RESEARCH ACTIVITIES

Theoretical and Computational Molecular Science

It is our goal to develop new theoretical and computational methods based on quantum mechanics, statistical mechanics, and molecular simulation in order to predict and understand the structures, reactions, and functions of molecules in gas, solution, and condensed phases as well as in nano- and bio-systems prior to or in cooperation with experiment.

Theoretical Study and Design of Functional Molecules: New Bonding, Structures, and Reactions

Department of Theoretical and Computational Molecular Science
Division of Theoretical Molecular Science I

NAGASE, Shigeru	Professor
OHTSUKA, Yuki	Assistant Professor*
TANAKA, Masato	IMS Fellow†
LUO, Gangfu	IMS Fellow
KATOUDA, Michio	Post-Doctoral Fellow
GUO, Jing-Doing	Post-Doctoral Fellow
GHOSH, Manik Kumer	Post-Doctoral Fellow
KARTHIKEYAN, Subramanlan	Post-Doctoral Fellow
SAKAKI, Shigeyoshi	Visiting Scientist
YAMADA, Mariko	Secretary
KONDO, Naoko	Secretarvy

In theoretical and computational chemistry, it is an important goal to develop functional molecules prior to or in cooperation with experiment. Thus, new bonds and structures provided by heavier atoms are investigated together with the reactivities. In addition, chemical modification and properties of nanocarbons are investigated to develop functional nanomolecular systems. Efficient computational methods are also developed to perform reliable quantum chemistry calculations for small and large molecular systems.

1. Two-Level Hierarchical Parallelization of Second-Order Møller-Plesset Perturbation Theory in Divide-and-Conquer Method

Electron correlation plays an important role in the accurate description of the energies, structures, and properties of molecules. Density functional theory (DFT) is widely used to calculate large molecules because of its low computational cost. However, frequently used DFT methods have several shortcomings. For example, they fail to describe non-covalent interaction energies and reaction barriers. Second-order Møller–Plesset perturbation (MP2) theory is the simplest method to account for electron correlation at an *ab initio* level. However, the computational cost is considerably high and the applications are limited to molecules of moderate size. We have developed an efficient parallel algorithm to reduce the computational cost as well as the requited sizes of memory and disk by employing the resolution-of-identity (RI) approximation.[1,2)] Despite the high performance, the computational cost is still too high for MP2 calculations to be applicable to very large molecules.

To make MP2 applicable to nanosystems and biological systems, we have developed a two-level hierarchical parallelization scheme in the divide-and-conquer (DC) method.[3)] In the DC-MP2 method, the total system is divided into small non-overlapping subsystems and its energy is obtained as a sum of the energies of subsystems. The two-level hierarchical parallelization scheme is a combination of coarse-grain parallelization assigning each subsystem to a group of processors, with fine-grain parallelization, where the computational tasks for evaluating MP2 correlation energy of the assigned subsystem are distributed among processors in the group.

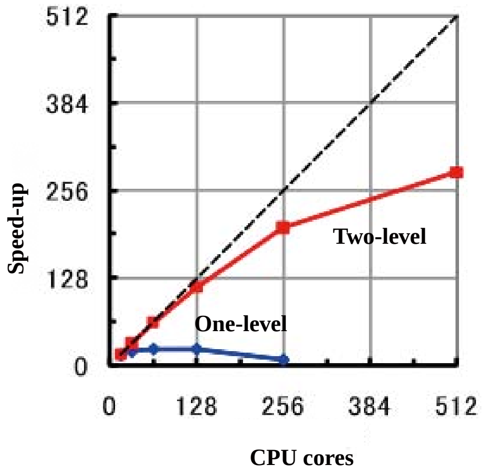

Figure 1. One-level and two-level parallelization of DC-MP2/6-31G* calculations of (β-alanine)$_{20}$.

Several test calculations on PC clusters show the high efficiency of the two-level hierarchical parallelization. Large scale parallel calculations of (β-alanine)$_{20}$ with the 6-31G* basis set are also performed using the T2K-Tsukuba massively parallel supercomputer. The results obtained using up to 512 CPU cores are summarized in Figure 1, which demonstrate that two-level parallelization becomes more effective for the larger number of CPU cores than single-level parallel calculations. It is noticeable that the two-level parallel calculation is 22 times faster even for 256 CPU cores than the single-level calculation. The parallel efficiency makes DC-MP2 calculations feasible for very large molecules in massively parallel computers.

2. A New Sampling Method for Projector Monte Carlo Calculations Based on Slater Determinants

In the next-generation computational chemistry, exact solutions of the Schrödinger equation are highly desired. For this purpose, we have developed a projector Monte Carlo method based on Slater determinants (PMC-SD) for the ground and excited sates.[4,5] Unlike the conventional method, no additional information such as nodes of trial wave functions is required. The accuracy of the PMC-SD method is improved systematically by increasing the number of walkers and the full-CI energies are obtainable as a limit for a given basis set. To make PMC-SD effective, we have proposed a new sampling method by using the symmetry of α and β electron configurations.[6] The advantages of the new sampling methods have been confirmed by several test calculations.

3. Examples of Computational Approaches to Interesting Molecular Systems

Endohedral metallofullerenes have attracted interest as building blocks of future nanoscale electronic devices because they have low oxidation and reduction potentials. Although endohedral metallofullerenes do not crystallize in general, chemical derivatization allows for the efficient crystallization. Thus, a single crystal is formed, in which the adamantylidene (Ad) derivative of La@C_{82} is aligned in an orderly fashion, as shown in Figure 2.[7]

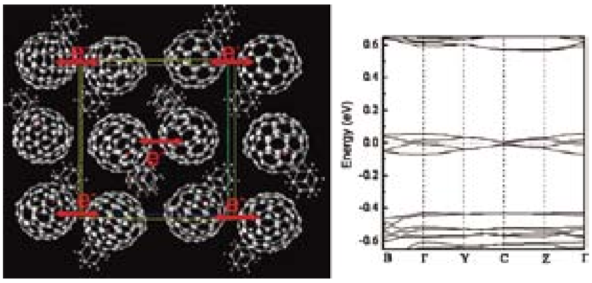

Figure 2. Single crystal of the La@C_{82} derivative and its band structure.

Density functional calculations confirm that the single crystal of La@C_{82}Ad is semi-metallic with a small band gap of 0.005 eV: the effective mass of electron of the conduction-band bottom and hole of the valence-band top is 0.97 and 0.97m_0 (m_0 is the mass of free electron), suggestive of nearly free-electron behavior. Accordingly, a high electron mobility of $\mu \geq 10$ cm^2 V^{-1} s^{-1} is observed by flash-photolysis time-resolved microwave conductivity measurements. The observed mobility is the highest of reported organic conductors. It is expected that the derivatization of endohedrtal metallofullerenes will open up a new field related to tunable organic conductors for molecular electronics.

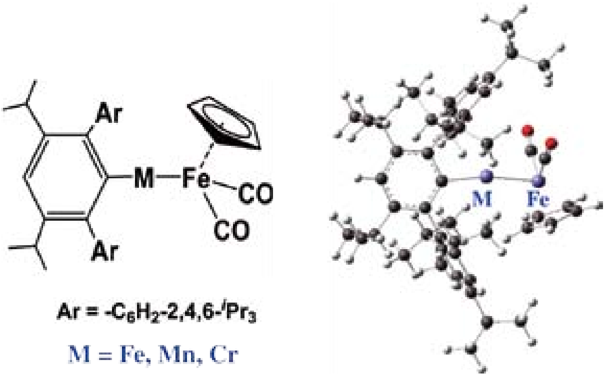

Figure 3. Two-coordinate transition metal complexes.

In collaboration with experiment, we have also performed calculations for (a) two-coordinate transition metal complexes with unusually short metal-metal bonds (Figure 3),[8] (b) planar four-membered aromatic systems protected by pentaary[60] fullerene,[9] (c) ferromagnetic spin coupling between La@C_{82} and cyclodimeric copper porphyrin upon inclusion,[10] and (d) covalently linked porphyrin-La@C_{82} hybrids.[11]

References

1) M. Katouda and S. Nagase, *Int. J. Quantum Chem.* **109**, 2121–2130 (2009).
2) M. Katouda and S. Nagase, *J. Chem. Phys.* **133**, 184103 (9 pages) (2010).
3) M. Katouda, M. Kobayashi, H. Nakai and S. Nagase, *J. Comput. Chem.* **32**, 2756–2764 (2011).
4) Y. Ohtsuka and S. Nagase, *Chem. Phys. Lett.* **463**, 431–434 (2008).
5) Y. Ohtsuka and S. Nagase, *Chem. Phys. Lett.* **485**, 367–370 (2010).
6) Y. Ohtsuka and S. Nagase, *Theor. Chem. Acc.* **130**, 501–505 (2011).
7) S. Sato, S. Seki, Y. Honsho, L. Wang, H. Nikawa, G. Luo, J. Lu, M. Haranaka, T. Tsuchiya, S. Nagase and T. Akasaka, *J. Am. Chem. Soc.* **133**, 2766–2771 (2011).
8) H. Lei, J. -D. Guo, J. C. Fettinger, S. Nagase and P. P. Power, *J. Am. Chem. Soc.* **132**, 17399–17401 (2010).
9) M. Maruyama, J. -D. Guo, S. Nagase, E. Nakamura and Y. Matsuo, *J. Am. Chem. Soc.* **133**, 6890–6893 (2011).
10) F. Hajjaj, K. Tashiro, H. Nikawa, N. Mizorogi, T. Akasaka, S. Nagase, K. Furukawa, T. Kato and T. Aida, *J. Am. Chem. Soc.* **133**, 9290–9292 (2011).
11) L. Feng, Z. Slanina, S. Sato, K. Yoza, T. Tsuchiya, N. Mizorogi, T. Akasaka, S. Nagase, N. Martin and D. M. Guldi, *Angew. Chem., Int. Ed.* **50**, 5909–5912 (2011).

---

* Present Address; Graduate School of System Informatics, Kobe University, Kobe 657-8501

† Present Address; Department of Chemistry, Hiroshima University, Higashi-Hiroshima 739-8526

Electron and Electromagnetic Field Dynamics in Nanostructures

Department of Theoretical and Computational Molecular Science
Division of Theoretical Molecular Science I

NOBUSADA, Katsuyuki	Associate Professor
YASUIKE, Tomokazu	Assistant Professor
NODA, Masashi	Post-Doctoral Fellow
YAMADA, Mariko	Secretary

We have developed theoretical methods to calculate photo-induced electron dynamics in nanostructured materials such as nanoparticles, quantum-dot arrays, and adsorbate-surface systems. Specifically, we have developed generalized theory of a light-matter interaction beyond a dipole approximation on the basis of the multipolar Hamiltonian with the aim of understanding the near-field excitation of molecules at the 1 nm scale. We have also studied exciton–polariton transmission in quantum dot waveguides. Furthermore, collectivity of plasmonic excitations in small sodium clusters was investigated in depth. Ultrafast relaxation dynamics of a gold cluster and adsorbate dynamics have been elucidated in collaboration with experimental groups.

1. Near-Field-Induced Optical Force on a Molecule[1)]

We have calculated the near-field-induced optical forces acting on a silver particle mimicked by a jellium model and on C_{60}. The real-time and real-space TDDFT approach combined with the nonuniform light-matter interaction formalism, recently developed by the authors, was employed to accurately calculate the inhomogeneous charge polarization induced by the full multipole interaction with the near field. The induced force is reasonably explained in terms of the polarization and screening charges. The local optical force on the silver particle takes both positive and negative values depending on the spatial distribution of these charges, and the net force becomes attractive as a result of a balance between the polarization and screening charges. The optical force on C_{60} is an order of magnitude smaller than that on the silver particle because of the lesser mobility of the electrons. The energy dependence of the optical force of these particles showed several maxima and minima, indicating that the resonance excitation does not necessarily induce the optical force most efficiently. Such a nonmonotonic energy dependence of the optical force will be utilized when manipulating nanoparticles at the nanometer scale by controlling the near-field frequency. To calculate the optical forces induced by a highly nonuniform electric field in real molecules, a sensible balance of the polarization and screening charges must be determined. The present first-principles TDDFT approach, taking account of full light-matter interactions, can be a powerful tool for optical manipulation in nanostructures.

2. Exciton–Polariton Transmission in Quantum Dot Waveguides[2)]

We have investigated the exciton–polariton energy transfer in bent or branched waveguides consisting of quantum dot arrays and designed the waveguide to facilitate the wave transmission. The efficient wave transformation between the longitudinal and transverse modes occurs in a waveguide bent by the angle smaller than 90° because of the interactions between the more than nearest-neighbor sites. The transmission efficiency lowers by the dispersion in velocity of the wave packet and also by the difference in the group velocity between the longitudinal and transverse waves. The difference in the group velocity is due to the fact that the longitudinal interaction is twice as large as the transverse one. However, the transmission efficiency was found to be sufficiently improved by controlling the interdot distance so as to equalize the longitudinal and transverse interactions. In the branched waveguide, the wave transmission generally decreased because the additional branch path induces the division of the transmission wave. We also found that the wave transmission rather efficiently occurred even in the branched waveguide by optimizing the branch angle so that the two branches bifurcate symmetrically. If there is energy difference (E) of the local exciton states between the adjacent sites, in the absence of thermal relaxation the transmission of the exciton–polariton wave through the sites was suppressed, depending on E. However, it has been clearly demonstrated that the existence of thermal relaxation enables to open a new channel of the transmission along which the exciton–polariton wave cannot transmit through the Coulomb interaction owing to the energy difference. We expect to control transmission paths in more complicated integrated waveguide circuits by changing temperature.

3. Collectivity of Plasmonic Excitations in Small Sodium Clusters with Ring and Linear Structures[3]

We have quantified the plasmonic excitations in small sodium clusters in terms of collectivity index, which allows us to study the nature of collective motions of electrons in ring and linear-chain geometries. We found that sodium nanostructures generally have plasmonic excitations irrespective of their geometries. The transition density distribution clearly shows that the strong peaks are assigned to the dipolar collective motions. The dipolar motions have three directions, and the energies of the corresponding plasmonic excitations are degenerate for a spherical particle. In the present clusters, the plasmonic excitations split into higher- and lower-energy modes owing to their lower symmetries. The lower-energy mode is attributed to the electronic motion along the direction where the electrons can move through a longer distance. In this case, the clusters have large transition moments although the corresponding collectivity indices are small. Therefore, we regard the lower-energy mode as a long-range charge transfer excitation. In contrast, the higher-energy plasmonic excitation is highly collective as a result of equal-strength interactions among energetically degenerate individual electronic states. In the vicinity of the higher-energy plasmonic excitation, we found that nondipolar collective modes exist. They are expected to play an important role in the interaction between nanoparticles in the context of nano-optics.

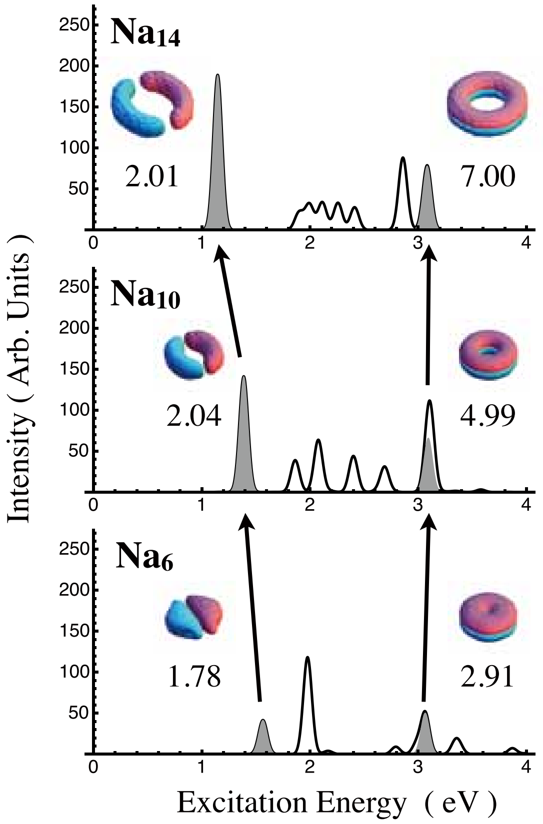

Figure 1. Photoabsorption spectra for ring Na$_n$ clusters (n = 6, 10, and 14). The color insets illustrate the transition density distributions for plasmonic excitations.

4. Ultrafast Relaxation Dynamics of Rod-Shaped 25-Atom Gold Nanoclusters[4]

We report a femtosecond spectroscopic investigation on the electronic structure and relaxation dynamics of a rod-shaped, 25-atom (Au_{25}) nanocluster capped by organic ligands. Broadband femtosecond transient absorption spectra of the cluster show overlapped excited state absorption and ground state bleach signals. Two lifetimes (*i.e.*, 0.8 ps fast component and a 2.4 µs long component) are identified, with the 0.8 ps component attributed to the fast internal conversion process from LUMO+*n* to LUMO and the long component to electron relaxation to the ground state. The rod shape of the cluster induces a strong anisotropic response in the transient absorption spectra, from which we deduce that the transition moment is oriented with the long axis of the prolate-shaped cluster. In addition, coherent phonon emission at 26 cm^{-1} was observed and results in the modulation of the excited state absorption transition energy.

5. Adsorbate-Localized versus Substrate-Mediated Excitation Mechanisms for Generation of Coherent Cs–Cu Stretching Vibration at Cu(111)[5]

Coherent Cs–Cu stretching vibration at a Cu(111) surface covered with a full monolayer of Cs is observed by using time-resolved second harmonic generation spectroscopy, and its generation mechanisms and dynamics are simulated theoretically. While the irradiations with ultrafast pulses at both 400 and 800 nm generate the coherent Cs–Cu stretching vibration at a frequency of 1.8 THz (60 cm^{-1}), they lead to two distinctively different features: The initial phase and the pump fluence dependence of the initial amplitude of coherent oscillation. At 400 nm excitation, the coherent oscillation is nearly cosine-like with respect to the pump pulse and the initial amplitude increases linearly with pump fluence. In contrast, at 800 nm excitation, the coherent oscillation is sine-like and the amplitude is saturated at high fluence. These features are successfully simulated by assuming that the coherent vibration is generated by two different electronic transitions: Substrate d-band excitation at 400 nm and the quasi-resonant excitation between adsorbate-localized bands at 800 nm, *i.e.*, possibly from an alkali-induced quantum well state to an unoccupied state originating in Cs 5d bands or the third image potential state.

References

1) T. Iwasa and K. Nobusada, *Phys. Rev. A* **82**, 043411 (2010).
2) Y. Kubota and K. Nobusada, *J. Chem. Phys.* **134**, 044108 (2011).
3) T. Yasuike, K. Nobusada and M. Hayashi, *Phys. Rev. A* **83**, 013201 (2011).
4) M. Y. Sfeir, H. Qian, K. Nobusada and R. Jin, *J. Phys. Chem. C* **115**, 6200 (2011).
5) K. Watanabe, Y. Matsumoto, T. Yasuike and K. Nobusada, *J. Phys. Chem. A* **115**, 9528 (2011).

Advanced Electronic Structure Theory in Quantum Chemistry

Department of Theoretical and Computational Molecular Science
Division of Theoretical Molecular Science I

YANAI, Takeshi	Associate Professor
KURASHIGE, Yuki	Assistant Professor
MIZUKAMI, Wataru	Graduate Student
YAMADA, Mariko	Secretary

Aiming at predictive computational modelings of molecular electronic structures with *ab initio* quantum chemistry calculations, our scientific exploration is to establish a cutting-edge theoretical methodology that allows one to compute accurately and efficiently the complex electronic structures, in which strongly-interacting electrons play a crucial role to characterize the nature of molecules. The complicated electronic structures can be handled accurately with the multireference theory, which deals with multiple important electronic configurations on equal footing. However, with the standard multireference methods such as the complete active space self-consistent field (CASSCF), the tractable size of the reference space is limited to small active space because the complexity of the calculations grows exponentially with the reference size. The existing multireference methods are nevertheless usefully applied to chemical theory problems such as exploring chemical reactions of bonding, dissociation and isomerization along the reaction coordinates, electronically excited states, unstable electronic structures of radical systems, and multiple covalent bindings in molecular metal complexes, *etc*. Our resultant works to be reported here are (1) to develop a type of the multireference correlation model named Canonical Transformation (CT) theory, which can efficiently describe short-range dynamic correlation on top of the multi-configurational staring wave function, (2) to construct the extensive complete active space self-consistent field (CASSCF) method combined with *ab initio* density matrix renormalization group (DMRG) method for making unprecedentedly larger active spaces available for the CASSCF calculations, and (3) to develop an efficient second-order perturbation theory that can use large active space with the DMRG-SCF reference wavefunction.

1. Second-Order Perturbation Theory with a DMRG Self-Consistent Field Reference Function: Theory and Application to the Study of Chromium Dimer[1)]

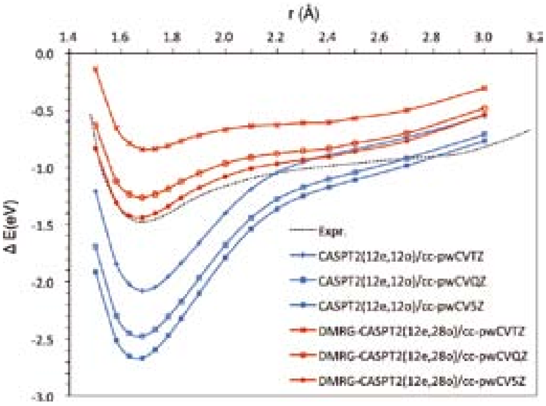

Figure 1. CASPT2(12e,12o)/$\mathbf{g}_1$ and DMRG-CASPT2(12e,28o)/$\mathbf{g}_1$/M = 512 potential energy curves of Cr_2 with a suite of cc-pwCXZ basis sets (X = T,Q,5). The energies ΔE are given relative to the isolated atoms. Experimental curve is included.

We have presented a second-order perturbation theory based on a density matrix renormalization group self-consistent field (DMRG-SCF) reference function. The method reproduces the solution of the complete active space with second-order perturbation theory (CASPT2) when the DMRG reference function is represented by a sufficiently large number of renormalized many-body basis, thereby being named DMRG-CASPT2 method. The DMRG-SCF is able to describe non-dynamical correlation with large active space that is insurmountable to the conventional CASSCF method,[2–3)] while the second-order perturbation theory provides an efficient description of dynamical correlation effects. The capability of our implementation is demonstrated for an application to the potential energy curve of the chromium dimer, which is one of the most demanding multireference systems that require best electronic structure treatment for non-dynamical and dynamical correlation as well as large basis sets. The DMRG-CASPT2/cc-pwCV5Z calculations were performed with a large (3*d* double-shell) active space consisting of 28 orbitals. Our approach using large-size DMRG reference addressed the problems of why the dissociation energy is largely overestimated by CASPT2 with the small active space consisting of 12 orbitals (3*d*4*s*), and also is oversensitive to the choice of the zeroth-order Hamiltonian. (**Figure 1**)

2. A Dual-Level Approach to Four-Component Relativistic Density-Functional Theory4)

This study presents an improvement that enhances the efficiency of the four-component density-functional theory (DFT) calculations by incorporating the dual-level approach proposed by Nakajima and Hirao into the Dirac-Kohn-Sham (DKS) method. At the heart of the dual-level approach is that high-cost hybrid DFT calculation using high-quality basis can be reproduced from a simple perturbation to much lower-cost DFT calculation that uses small basis and low-level pure exchange-correlation functional. The accuracy of this approach hinges on the insight that the description of total density is insensitive to the level of calculation. Significant computational saving arises in avoiding self-consistent field (SCF) procedure of iterating the time-consuming evaluation of Fock matrix in large basis representation as well as its large-dimensional diagonalization.

In the dual-level approach, a pair of the basis sets and exchange-correlation functionals is defined for specifying each level of the low- and high-cost calculations. We apply this scheme to four-component DFT calculations. Although this can be approached in a rather straightforward way, we attempt to mix an extra ingredient associated with the relativistic extension. In the present study, the duality of relativistic treatment is further invoked to achieve a further cost saving in the low-level calculations, for which the two-component relativistic approximation is employed.

There has been considerable progress in the development of a computationally less demanding two-component Hamiltonian which effectively neglects negative states. As the most suitable two-component method that allows for transparently bridging a gap between low- and high-level (*i.e.* four-component) descriptions, we employ a quasi-relativistic scheme proposed by Iliaš and Saue for implementing the Infinite-Order Two-Component (IOTC) relativistic Hamiltonian derived by Barysz and Sadlej. It is generated from a one-step decoupling transformation starting from the Dirac operator in the finite basis representation. The key reason for employing the IOTC Hamiltonian is that the decoupling matrix for the transformation is obtained as unitary. This unitarity is exploited, allowing for accurately retaining the description of the density matrix when it is similarity-transformed as frozen for the secondary high-level calculation. (**Figure 2**)

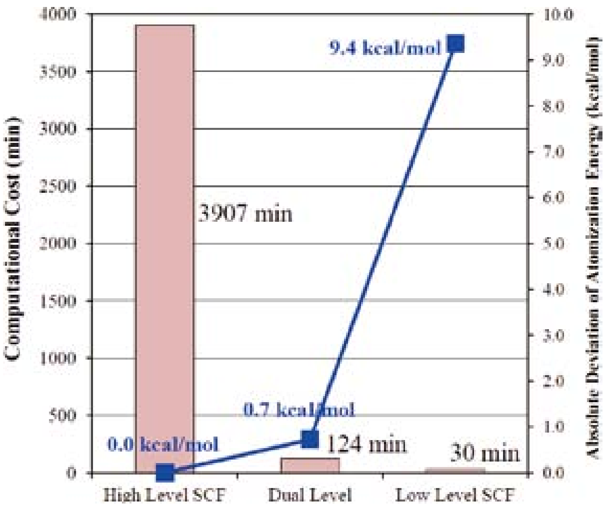

Figure 2. Computational times (bar) of the high- and low-level SCF calculations as well as the dual-level one for AuH at the equilibrium geometry, and the absolute deviations (square) of the atomization energies from the high-level result. The B3LYP functional is chosen as both high- and low-level functionals.

3. Canonical Transformation Theory for Multireference Dynamic Correlation Calculations

We have proposed a new class of explicit correlated theory on the basis of the effective Hamiltonian approach using the so-called canonical transformation (CT). The CT theory has been developed by Yanai, Chan, Neuscamman, and coworkers, in which dynamic electron correlation is described by a similarity transformation of the Hamiltonian H using a unitary exponential operator exp(A) with the excitation amplitude operator A = –A*. The central idea is to use the operator and cumulant decompositions to define a two-body effective Hamiltonian through an approximate Baker-Campbell-Hausdorff expansion,

$$\exp(-A)\, H \exp(A) = H + [H,A]_{1,2} + 1/2[[H,A],A]_{1,2} + \ldots$$

which can be evaluated recursively. Here $[\ldots]_{1,2}$ denotes that a commutator is approximated by an operator that contains only one- and two-body operators in the sense of generalized normal ordering of Mukherjee and Kutzelnigg.

We generalize this approach to F12 theory by introducing an A operator that depends on the interelectronic distances. In the present work, we use a Slater-type geminal function $[f(r_{12}) = -k^{-1}\exp(-k\, r_{12})]$ and project it onto the two-body operator bases. The associated amplitudes are determined by the first-order cusp condition as Ten-no proposed in F12 theory (SP or “fixed” Ansatz), so that the A is determined *a priori*.

References

1) Y. Kurashige and T. Yanai, *J. Chem. Phys.* **135**, 094104 (9 pages) (2011).
2) W. Mizukami, Y. Kurashige and T. Yanai, *J. Chem. Phys.* **133**, 091101 (4 pages) (2010).
3) Y. Kurashige and T. Yanai, *J. Chem. Phys.* **130**, 234114 (21 pages) (2009).
4) W. Mizukami, T. Nakajima, K. Hirao and T. Yanai, *Chem. Phys. Lett.* **508**, 177–181 (2011).

Developing the Statistical Mechanics Theory of Liquids in Chemistry and Biophysics

Department of Theoretical and Computational Molecular Science
Division of Theoretical Molecular Science II

HIRATA, Fumio	Professor
YOSHIDA, Norio	Assistant Professor
MARUYAMA, Yutaka	Post-Doctoral Fellow
PHONGPHANPHANEE, Saree	Post-Doctoral Fellow
SINDHIKARA, Daniel J.	Post-Doctoral Fellow
KIYOTA, Yasuomi	Post-Doctoral Fellow
SUETAKE, Yasumi	Secretary
KONDO, Naoko	Secretary
YAMADA, Mariko	Secretary

"Molecular recognition" is an essential elementary process for protein to function. The process is a thermodynamic process which is characterized with the free energy difference between two states of a host-guest system, namely, associated and dissociated states. It is readily understood that the structural fluctuation of protein gives a big effect on the free energy barrier. In that respect, the "molecular recognition" is a thermodynamic process which is conjugated with the structural fluctuation of protein.

We have been developing a new theory concerning the molecular recognition, based on the 3D-RISM/RISM theory which is a statistical mechanics of liquids. The theory has successfully "probed" small ligands such as water molecules and ions bound in a small cavity of protein.[1–3)]

1. Solvent and Salt Effects on Structural Stability of Human Telomere[4)]

Human telomere DNA is of intense interest because of its role in the biology of both cancer and aging. The single-stranded telomere terminus can adopt the structure of a G-quadruplex, which is of particular importance for anticancer drug discovery, and various G-quadruplex structures have been reported. The solution structure of human telomeric DNA in the presence of Na^+ has been determined by NMR to be anti-parallel basket-type, while the structure in KCl solution is still an open question. So, we have studied telomere structure in the two electrolyte solutions based on the 3D-RISM theory.

In pure water, the chair-type conformation was found to be the most stable one, which is followed by basket-, hybrid-, and propeller-type structures in the order. It is clarified that the order of the stability is determined essentially by the solvation free energy, not by the conformational energy.

The order of the stability changes in 0.1 M NaCl solutions from that in pure water. The basket-type structure becomes the most stable one in the electrolyte solution. The theoretical finding is consistent with the experimental observation due to NMR. The reversed order of the conformational stability was attributed to the salt effect, especially, to that from the Na^+ ions bound at inter-strand spaces of DNA.

Concerning the conformational stability in KCl solutions, our results predict that the order is not changed from that in pure water, that is, the chair-type is the most stable one. The finding suggests that the effect of the potassium ion upon the structure is not so strong as the sodium ion to change the order of the stability determined in pure water.

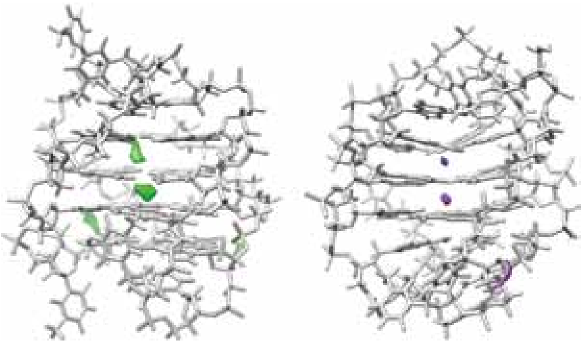

Figure 1. Na^+ and K^+ ions bound, respectively, by the basket- and chair-type structures of human telomere.

2. The Electronic-Structure Theory of a Large Molecular-System in Solution: Application to the Intercalation of Proflavin with Solvated DNA[5)]

A new approach (QM/MM/RISM) to treat the electronic structure of a macromolecule in solutions, which combines the quantum mechanics (QM), molecular mechanics (MM) and the RISM/3D-RISM theory, was presented. In the approach, solute is treated with the QM/MM method, while the solvent effect is handled by the RISM/3D-RISM theory. (Figure 2)

The QM/MM/RISM method was applied to investigate the intercalation of proflavine (PR) to decameric DNA double strands as an illustrative example. The free energy and solvation structure of $[deca(dA\text{-}dT)]_2$ and $[deca(dG\text{-}dC)]_2$ and their complex with PR were evaluated. The free energy change associated with the intercalation as well as the affinity of PR to two different DNA sequences was considered. The dG-dC base sequence shows greater affinity to proflavine than the dA-dT sequence. The results are consistent with the earlier experimental and computational studies.

We evaluated the three-dimensional distribution function (3D-DF) of solvent around solutes, DNA, PR, and DNA-PR complexes. We also calculated the radial distribution functions (RDFs) of solvent atoms around a designated atom of solutes. The intercalation induces a drastic change in the solvation structure of PR represented by the distribution functions. The exclusion of water molecules upon the intercalation contributes to increasing in $\Delta\mu$ of DNA-PR complexes. The solvent distribution also indicates that the polar solvent is distributed around negatively charged phosphates, and the amine of proflavine mitigates the electronic interaction between those atoms. Our results clearly support the hypothesis proposed by Ruiz *et al*.

It was demonstrated in this article that the method is applicable to a variety of nano- and biochemical problems involving the electronic structure of a large molecules in solvent. Such studies with the QM/MM/RISM method are in progress.

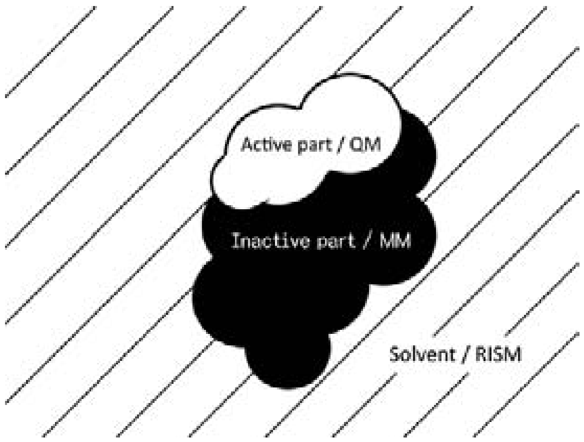

Figure 2. Schematic descripttion of partitioning of the system in QM/MM/RISM method.

3. A New Approach for Investigating the Molecular Recognition of Protein: Toward Structure-Based Drug-Design Based on the 3D-RISM Theory$^{6)}$

Recently, we started our effort on drug design based on the 3D-RISM theory. Our strategy to realize "drug binding" or molecular recognition (MR) has been to consider a drug molecule as a component of solvent or solution, and to find the distribution of drug molecules around the binding site of protein by solving the 3D-RISM equation. The method was so successful as far as the size of drug molecules is reasonably small, such as water and ethanol. However, we have realized that the method becomes increasingly difficult as molecular size of drug gets bigger and bigger. It is because numerical solutions of the 1D-RISM equation for solvent, which should be done prior to the 3D-RISM calculation, becomes unstable due to inherent non-linearity of the equation.

However, many ligands of biological interests, including ordinary drug molecules, are not so small. Therefore, we proposed a new approach to tackle the MR of large ligand molecules by protein based on the 3D-RISM and RISM theories. The strategy of the method is to regard both a ligand molecule and a receptor protein as solutes, which are immersed in solvent in the infinite dilution. The distribution of ligand molecules around a receptor protein is described by the sol**u**te–sol**u**te 3D-RISM (or uu-3D-RISM) instead of conventional sol**u**te–sol**v**ent 3D-RISM (or uv-3D-RISM).

The new method is applied to Phospholipase A2 (PLA2) which is known as a receptor of acetylsalicylic acid (aspirin). Since the size of aspirin is much larger and more complex than those we have examined previously, to analyze the density distribution function (DDF) from uu-3D-RISM is not a trivial problem. So, we developed a new method to analyze DDF, defining a new function which locates the center of the most probable distribution of ligand. The orientation of aspirin inside the binding-site of PLA2 was determined by defining a score function which ranks the fitting level of trial orientations with DDF. The binding mode of the ligand inside the pocket was in fair agreement with that determined from the X-ray crystallography. (Figure 3)

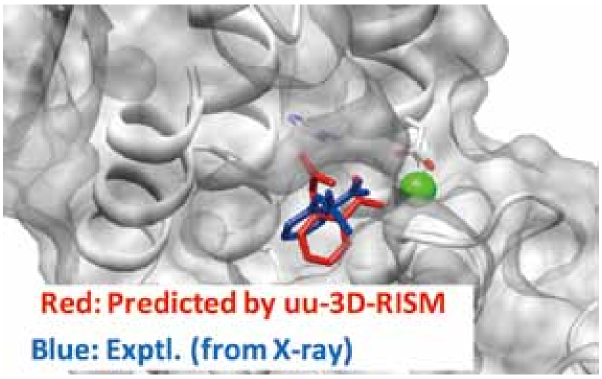

Figure 3. Predicted binding-mode of aspirin, which is obtained from uu-3D-RISM. The binding-mode determined by X-ray structure is depicted with blue sticks.

References

1) F. Hirata, *Molecular Theory of Solvation*, Kluwer; Dordrecht, Netherlands (2003).
2) A. Kovalenko and F. Hirata, *J. Chem. Phys.* **110**, 10095–10112 (1999).
3) T. Imai, R. Hiraoka, A. Kovalenko and F. Hirata, *J. Am. Chem. Soc. (Communication)* **127**, 15334–15335 (2005).
4) Y. Maruyama, T. Matsushita, R. Ueoka and F. Hirata, *J. Phys. Chem.* **115**, 2408 (2011).
5) N. Yoshida, Y. Kiyota and F. Hirata, *J. Mol. Liq.* **159**, 83 (2011).
6) Y. Kiyota, N. Yoshida and F. Hirata, *J. Chem. Theory Comput.* **7**, 3803–3815 (2011).

Theory of Nonequilibrium Quantum Transport

Department of Theoretical and Computational Molecular Science
Division of Theoretical Molecular Science II

YONEMITSU, Kenji	Associate Professor
TANAKA, Yasuhiro	Assistant Professor
NISHIOKA, Keita	IMS Fellow
MIYAZAKI, Mitake	Visiting Scientist*
KONDO, Naoko	Secretary

Nonlinear conduction in correlated electron systems such as one-dimensional Mott insulators and two-dimensional charge-ordered materials has been of great interest in the past few decades. They offer intriguing subjects of nonequilibrium physics in condensed matter and the possibility for novel functions of electronic devices. Here, we study the relationship between the nonlinear conduction in nano-sized materials and the dielectric breakdown of bulk insulators from a general viewpoint. Then, we study the relationship between the non-linear conduction and the coexisting charge orders in two-dimensional organic materials.

1. Crossover from Bias-Induced to Field-Induced Breakdown of Insulators$^{1)}$

We focus on quasi-two-dimensional quarter-filled-band charNonequilibrium states induced by an applied bias voltage (V) and the corresponding current–voltage characteristics of one-dimensional models describing band and Mott insulators (Figure 1) are investigated theoretically by using non-equilibrium Green's functions.$^{2)}$ We attach the models to metallic electrodes, whose effects are incorporated into the self-energy. Modulation of the electron density and the scalar potential coming from the additional long-range interaction are calculated self-consistently within the Hartree approximation. For both models of band and Mott insulators with length L_C, the bias voltage induces a breakdown of the insulating state, whose threshold shows a crossover as a function of L_C (Figure 2). It is determined basically by the bias $V_{th} \sim \Delta$ for L_C smaller than the correlation length $\xi = W/\Delta$, where W denotes the bandwidth and Δ denotes the energy gap. For systems with L_C much larger than ξ, the threshold is governed by the electric field V_{th}/L_C, which is consistent with a Landau-Zener–type breakdown, where V_{th}/L_C is proportional to Δ^2/W. The spatial dependence of the scalar potential turns out to be crucially important for this crossover: without the scalar potential, the breakdown would occur unnaturally at $V_{th} \sim \Delta$ regardless of the length of the central part L_C.

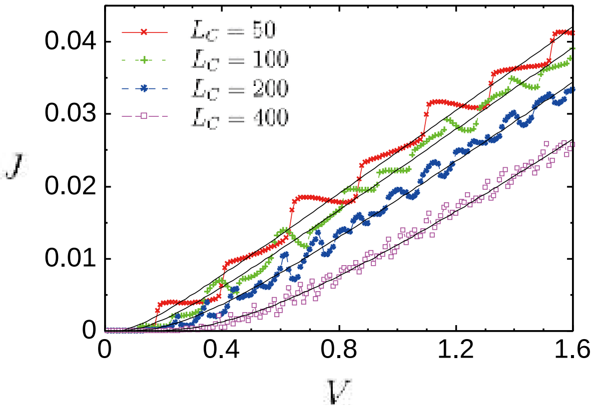

Figure 1. Current (J)–Voltage (V) characteristics of one-dimensional band insulators for several sizes of the central part L_C, with alternation of transfer integrals $\delta t = 0.025$, Coulomb parameter $V_p = 0.1$, and coupling to left and right electrodes $\gamma_L = \gamma_R = 0.1$. The solid lines show the function $J = aV \exp(-V_{th}/V)$, which fits to the results.

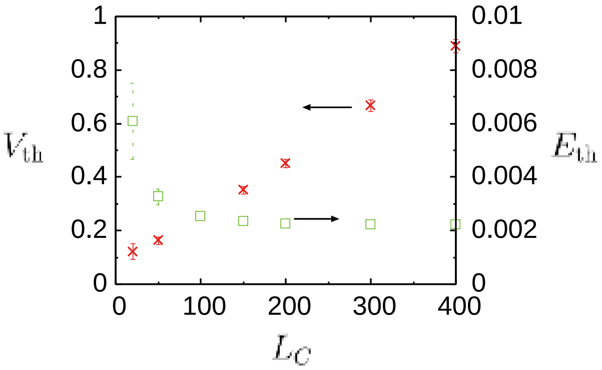

Figure 2. Dependence of the threshold bias voltage V_{th} and the threshold electric field E_{th} on the size of the central part L_C. The other parameters are the same as in Figure 1.

2. Nonlinear Conduction and Melting of Charge Order on a Triangular Lattice3)

As described above, a photoinduced insulator-to-metal tranThe observations of the giant nonlinear conduction and spontaneous current oscillation in the organic compounds θ-(BEDT-TTF)$_2$CsM(SCN)$_4$ (M = Co and Zn) have renewed interest since the electric-field-induced behaviors differ in many respects from the sliding of density waves in quasi-one-dimensional materials, where a nesting of the Fermi surface is responsible for their ground states. In quasi-two-dimensional organic conductors θ-(BEDT-TTF)$_2$X, the long-range Coulomb repulsion is mainly responsible for the ground state accompanied with charge orders.

We focus on the mechanism of the peculiar nonlinear conduction in θ-(BEDT-TTF)$_2$X through the melting of stripe-type charge order. An extended Peierls-Hubbard model attached to metallic electrodes (Figure 3) is investigated by a nonequilibrium Green's function technique.2) A novel current–voltage characteristics (Figure 4) appears in a coexistent state of stripe-type and non-stripe 3-fold charge orders, where the applied bias melts mainly the stripe-type charge order through the reduction of lattice distortion, whereas the 3-fold charge order survives (Figure 5). These contrastive responses of the two different charge orders are consistent with the experimental observations.

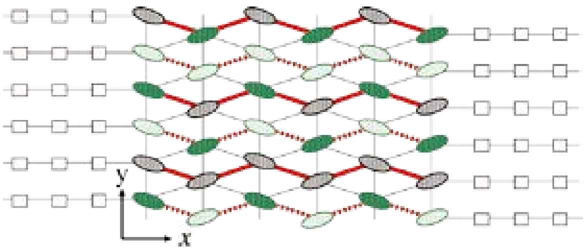

Figure 3. Schematic picture of the model. The left and right electrodes are attached to the central part where the horizontal and 3-fold charge orders coexist.

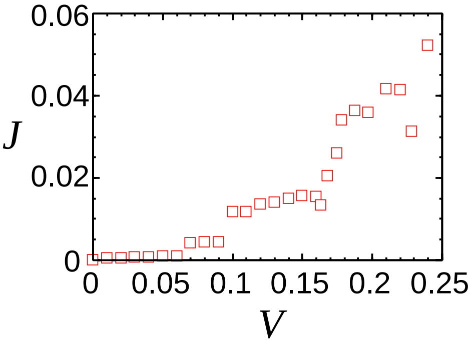

Figure 4. Electric current J, as a function of V.

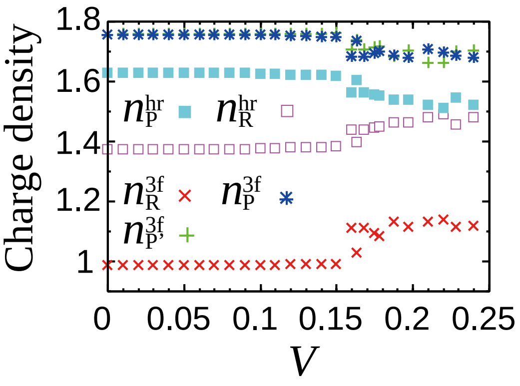

Figure 5. Horizontal (n^{hr}_R and n^{hr}_P) and 3-fold (n^{3f}_R, n^{3f}_P, and $n^{3f}_{P'}$) components of the charge distribution, as a function of V.

When both stripe-type and 3-fold charge orders exist, the density of states at the chemical potential of the central part μ_C, is suppressed compared to the purely 3-fold charge-ordered state (Figure 6). A small current flows because the coexistent state has no energy gap in the thermodynamic limit. Above a threshold bias voltage, the density of states at μ_C is large since the horizontal charge modulation is significantly decreased. This change in the conduction behavior is triggered by the reduction of lattice distortion.

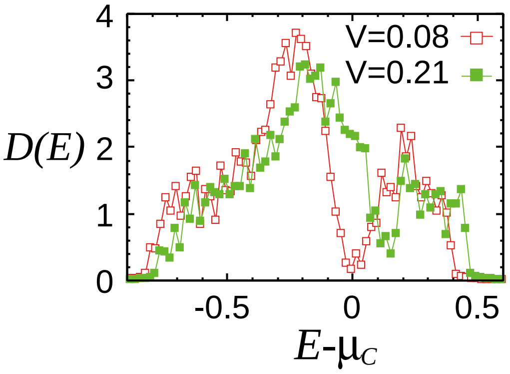

Figure 6. Density of states for V = 0.08 and 0.21.

References

1) Y. Tanaka and K. Yonemitsu, *Phys. Rev. B* **83**, 085113 (11 pages) (2011).
2) K. Yonemitsu, *J. Phys. Soc. Jpn.* **78**, 054705 (8 pages) (2009).
3) Y. Tanaka and K. Yonemitsu, *Phys. B (Amsterdam, Neth.)* **405**, S211–S213 (2010).

* from Hakodate National College of Technology

Theoretical Studies on Condensed Phase Dynamics

Department of Theoretical and Computational Molecular Science
Division of Computational Molecular Science

SAITO, Shinji	Professor
KIM, Kang	Assistant Professor
HIGASHI, Masahiro	JSPS Post-Doctoral Felloww
YAGASAKI, Takuma	Post-Doctoral Fellow
IMOTO, Sho	Graduate Student
KAWAGUCHI, Ritsuko	Secretary

Liquids and biological systems show complicated dynamics because of their structural flexibility and dynamical hierarchy. Understanding these complicated dynamics is indispensable to elucidate chemical reactions and relaxation in solutions and functions of proteins. We have been investigating complex dynamics in supercooled liquids,1–3) chemical reactions in biological systems using molecular dynamics simulation4) and the stability of ions at water/vapor interface.5) In addition, we have been theoretically investigating liquid dynamics by using linear and higher-order nonlinear IR spectroscopy.6,7)

1. Role of the Lifetime of Dynamical Heterogeneity in the Frequency-Dependent Stokes–Einstein Relation of Supercooled Liquids1)

We previously investigated the lifetime of dynamical heterogeneity in supercooled liquids in terms of a four-point, three-time density correlation function *via* molecular dynamics simulations [*Phys. Rev. E* **79**, 060501(R) (2009); *J. Chem. Phys*. **133**, 044511 (2010)]. In this letter, we examine the physical role of the lifetime of dynamicsl heterogeneity in the violation of the Stokes–Einstein (SE) relation by calculating the frequency-dependent viscosity and self-diffusion constant. Our results demonstrate that the SE relation holds up to the time scale at which the non-Gaussian parameter is maximum. Large violations of the SE relation are characterized by time scales longer than the lifetime of the dynamical heterogeneity in highly supercooled liquids.

2. Hidden Slow Time Scale of Correlated Motions in Supercooled Liquids: Multi-Time Correlation Function Approach2)

A three-time correlation function of particle displacements is introduced and numerically calculated by performing molecular dynamics simulations of binary soft-sphere supercooled systems. It is found that the two-dimensional representations of the three-time correlation function reveal couplings of particle motions that exist over a wide range of time scales. Furthermore, it is demonstrated that the systematic change in the second time interval in the three-time correlation function enables us to analyze how the correlations in mobility decay with time. From this analysis, the characteristic time scale of dynamical heterogeneity is quantified. We find that the dynamical heterogeneity time scale becomes much slower than the α-relaxation time as the temperature decreased.

3. Relation between Conformational Heterogeneity and Reaction Cycle of Ras: Molecular Simulation of Ras4)

Ras functions as a molecular switch by cycling between the active GTP-bound state and the inactive GDP-bound state.

It is known experimentally that there is another GTP-bound state called state 1. We investigate the conformational changes and fluctuations arising from the difference in the coordinations between the switch regions and ligands in the GTP and GDP-bound states using a total of 830 ns of molecular-dynamics simulations. Our results suggest that the large fluctuations among multiple conformations of switch I in state 1 owing to the absence of coordination between Thr-35 and Mg^{2+} inhibit the binding of Ras to effectors. Furthermore, we elucidate the conformational heterogeneity in Ras by using principal component analysis, and propose a two-step reaction path from the GDP-bound state to the active GTP-bound state *via* state 1. This studysuggests that state 1 plays an important role in signal transduction as an intermediate state of the nucleotide exchange process, although state 1 itself is an inactive state for signal transduction.

4. Effects of Nonadditive Interactions on Ion Solvation at the Water/Vapor Interface: A Molecular Dynamics Study$^{5)}$

The solvation of halide ions at the water/vapor interface is investigated by using molecular dynamics simulations with nonpolarizable molecular mechanical (MM), polarizable MM, and quantum mechanical (QM)/MM methods. The free energy profile of the ion solvation is decomposed into the energy and the entropic contributions along the ion displacement from inside to the surface of water. It is found that the surface affinity of the ion, relative to the bulk value, is determined by a subtle balance between the energetic destabilization and the entropic stabilization with the ion displacement. The amount of energetic destabilization is found to be reduced when nonadditive interactions are included, as in the polarizable MM and QM/MM models. The structure of water around the ion at the interface is also largely modified when the higher order effects are considered. For example, the induced dipole effect enhances the solvation structure around the ion at the interface significantly and thus reduces the amount of entropic stabilization at the interface, relative to in the bulk. It is found that this induced dipole effect causes the slowing in the ion–water hydrogen bond dynamics at the interface. On the other hand, the higher order induced multipole effects in the QM/MM method suppress both the excessive enhancement of the solvation structure and the slowing of the ion–water hydrogen bond dynamics at the interface. The present study demonstrates that not only the induced dipole moment but also the higher order induced multipole moments, which are neglected in standard empirical models, are essential for the correct description of the ion solvation at the water/vapor interface.

5. A Novel Method for Analyzing Energy Relaxation in Condensed Phases Using Nonequilibrium Molecular Dynamics Simulations: Application to the Energy Relaxation of Intermolecular Motions in Liquid Water$^{6)}$

We present a novel method to investigate energy relaxation processes in condensed phases using nonequilibrium molecular dynamics simulations. This method can reveal details of the time evolution of energy relaxation like two-color third-order IR spectroscopy. Nonetheless, the computational cost of this method is significantly lower than that of third-order response functions. We apply this method to the energy relaxation of intermolecular motions in liquid water. We show that the intermolecular energy relaxation in water is characterized by four energy transfer processes. The structural changes of the liquid associated with the energy relaxation are also analyzed by the nonequilibrium molecular dynamics technique.

References

1) K. Kim and S. Saito, *J. Phys Soc. Jpn.* **79**, 093601 (4 pages) (2010).
2) K. Kim and S. Saito, *J. Non-Crys. Solids* **357**, 371–375 (2010).
3) K. Kim, K. Miyazaki and S. Saito, *Eur. Phys. J. Special Topics* **189**, 135–139 (2010).
4) C. Kobayashi and S. Saito, *Biophys. J.* **99**, 3726–3734 (2010).
5) T. Yagasaki, S. Saito and I. Ohmine, *J. Phys. Chem. A* **114**, 12573–12584 (2010). (invited)
6) T. Yagasaki and S. Saito, *J. Chem. Phys.* **134**, 184503 (9 pages) (2011).
7) S. Yamaguchi, S. Saito and K. Tominaga, *Phys. Chem. Chem. Phys.* **13**, 14742–14749 (2011).

Theoretical Study on Molecular Excited States and Chemical Reactions

Department of Theoretical and Computational Molecular Science
Division of Computational Molecular Science

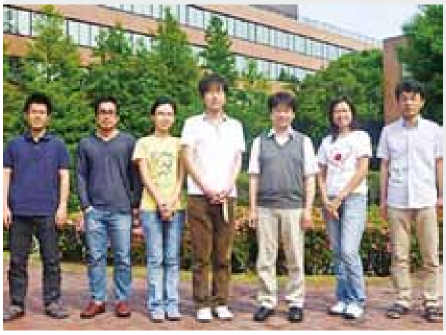

EHARA, Masahiro	Professor
FUKUDA, Ryoichi	Assistant Professor
TASHIRO, Motomichi	IMS Research Assistant Professor
BOBUATONG, Karan	Post-Doctral Fellow
NUNTHABOOT, Nadtanet	Visiting Scientist
NAMUANGRUK, Supawadee	Visiting Scientist
HORIKAWA, Takenori	Graduate Student
KAWAGUCHI, Ritsuko	Secretary

Molecules in the excited states show characteristic photophysical properties and reactivity. We investigate the molecular excited states and chemical reactions which are relevant in chemistry, physics, and chemical biology with developing the highly accurate electronic structure theory. We are also interested in the excited-state dynamics and energy relaxation so that we also develop the methodology of large-scale quantum dynamics. In this report, we report our recent studies on the development of the PCM-SAC-CI method,1) Excited-state geometry and vibrational frequency,2) and Double core-hole states and Auger processes.3)

1. Development of PCM-SAC-CI Method for Vertical Electronic Transitions1)

Transitions between electronic states of molecules in solution are important subjects in theoretical and computational chemistry. That is associated with the recent priority issues of molecular science, such as improving the efficiency of light-energy convergence or developing of molecular-scale devices. For this purpose, we have developed a theory foe electronic excitations in solution by generalizing the polarizable continuum model (PCM) to molecular solutes described at the level of the symmetry-adapted cluster (SAC) and symmetry-adapted cluster–configuration interaction (SAC-CI) methods.

We presented the theory and implementation of the nonequilibrium solvation model of PCM SAC/SAC-CI method for describing vertical photoemission and photoabsorption processes of molecules in solution. The concept of nonequilibrium solvation has been introduced to describe the solvent polarization processes involving sudden variation of solute charge distribution. In the PCM, the polarization vector of the dielectric medium is partitioned into two components: Namely, the fast or dynamical component and the slow or inertial component. The fast component is associated with all the degree of freedom of the solvent molecules having characteristic times faster than the time scale of the sudden process of solute, while the slow component collects all the other contributions from the degree of freedom having slower characteristic times.

Using the nonequilibrium solvation scheme, a vertical electron transition from an initial state to a final state may be described as follows: The initial state is described by equilibrium solvation, while in the final state, the inertial component remains in the solvation for the initial states. We have formulated such nonequilibrium solvation scheme within the PCM SAC/SAC-CI frameworks and computational program have been implemented. The effect of nonequilibrium solvation was significant for methylene–cyclopropene in aqueous solution; the directions of solvent effects were opposite between equilibrium and nonequilibrium models (Figure 1).

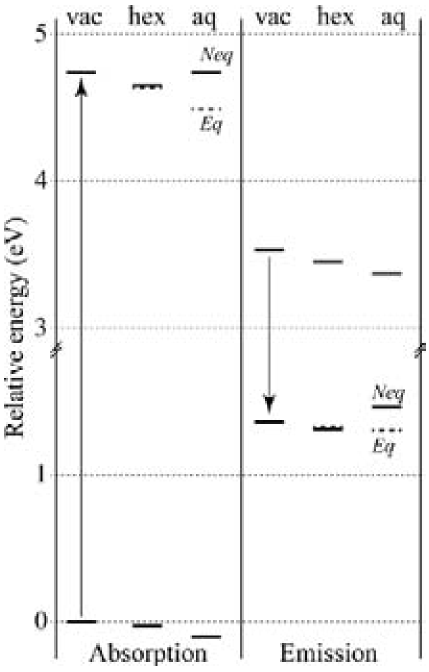

Figure 1. Relative energies of methylenecyclopropene in the ground and first excited states, where the ground state geometry was used for absorption and the excited state geometry with a planar constraint was used for emission. Solid horizontal lines denote nonequilibrium solvation results and broken lines denote equilibrium solvation results.

2. Excited-State Geometries and Vibrational Frequencies Studied by the Analytical Energy Gradients of the SAC-CI Method[2)]

Electronic properties, geometric structures, and spectroscopic constants in molecular excited states are of interest because they are characteristics compared with those in the ground states. Geometry relaxation and dissociation dynamics in the excited states can be elucidated by analyzing the fine structure arising from the vibrational spectra. Theoretical information is valuable for interpreting these high-resolution spectra and the physics behind them.

In this series of studies, we systematically apply the analytical energy gradients of the direct symmetry-adapted cluster–configuration interaction singles and doubles nonvariational method to calculate the equilibrium geometries and vibrational frequencies of excited and ionized states of molecules. The harmonic vibrational frequencies were calculated using the second derivatives numerically computed from the analytical first derivatives and the anharmonicity was evaluated from the three-dimensional potential energy surfaces around the local minima. In this paper, the method is applied to the low-lying valence singlet and triplet excited states of HAB-type molecules, HCF, HCCl, HSiF, HSiCl, HNO, HPO, and their deuterium isotopomers. The vibrational level emission spectra of HSiF and DSiF and absorption spectra of HSiCl and DSiCl were also simulated within the Franck–Condon approximation and agree well with the experimental spectra (Figure 2). The results show that the present method is useful and reliable for calculating these quantities and spectra. The change in geometry in the excited states was qualitatively interpreted in the light of the electrostatic force theory. The effect of perturbation selection with the localized molecular orbitals on the geometrical parameters and harmonic vibrational frequencies is also discussed.

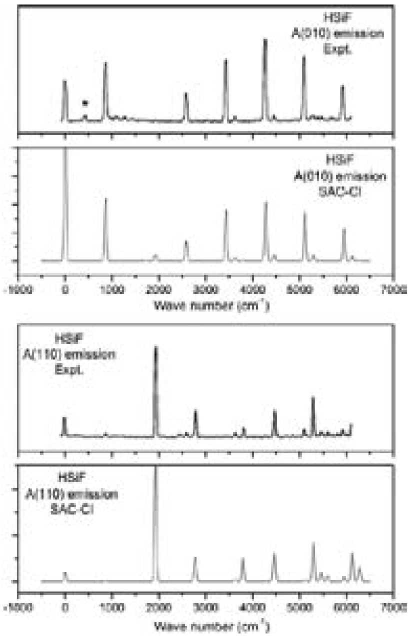

Figure 2. The SAC–CI *A*(010) and *A*(110) emission spectra of HSiF compared with the observed SVL emission spectra.

3. Double Core-Hole States and Auger Processes[3)]

Double core-hole states of atoms and molecules have long been objects of interest and are recently focused because of the development of various kinds of spectroscopy.

In this work, we have collaborated with the experimental group and investigated the DCH states of CH_4 and NH_3 and subsequent Auger decay processes. Energies of the hollow molecules CH_4^{2+} and NH_3^{2+} with double vacancies in the 1*s* shells have been measured using an efficient coincidence technique combined with synchrotron radiation. The energies of these states have been determined accurately by the CASSCF calculations and can be well understood on the basis of a simple theoretical model. Their major decay pathway, successive Auger emissions, leads first to a new form of triply charged ion with a core hole and two valence vacancies (Figure 3); experimental evidence for such a state is presented with its theoretical interpretation. Preedge 2-hole–1-particle (2*h*–1*p*) states at energies below the double core-hole states are located in the same experiments and their decay pathways are also identified.

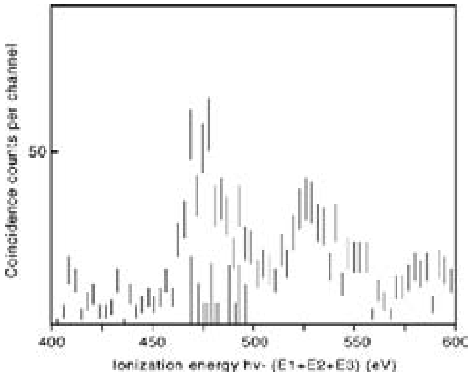

Figure 3. Triple coincidence spectrum selected within the range of the peak for DCH formation in NH_3 at $h\nu = 950$ eV. The main feature around 475 eV ionization energy represents the CVV triply ionized state reached by the first step of Auger decay from the hollow ammonia molecule.

References

1) R. Fukuda, M. Ehara, H. Nakatsuji and R. Cammi, *J. Chem. Phys.* **134**, 104109 (11 pages) (2011).

2) M. Ehara, F. Oyagi, Y. Abe, R. Fukuda and H. Nakatsuji, *J. Chem. Phys.* **135**, 044316 (14 pages) (2010).

3) J. H. D. Eland, M. Tashiro, P. Linusson, M. Ehara, K. Ueda and R. Feifel, *Phys. Rev. Lett.* **105**, 213005 (4 pages) (2010).

Development of New Algorithms for Molecular Dynamics Simulation and Its Application to Biomolecular Systems

Department of Theoretical and Computational Molecular Science
Division of Computational Molecular Science

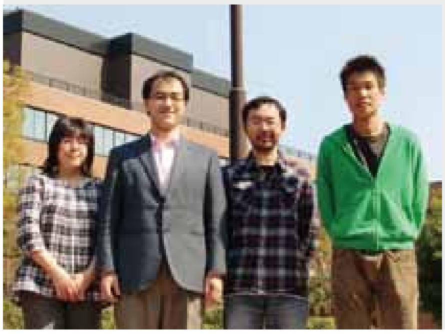

OKUMURA, Hisashi	Associate Professor
ITOH, G. Satoru	Assistant Professor
SAKAGUCHI, Takeshi	Graduate Student*
KAWAGUCHI, Ritsuko	Secretary

To predict the native structures of proteins, efficient samplings in the conformational space by molecular dynamics simulations are necessary. In the conventional canonical-ensemble simulations, however, it is difficult to realize efficient samplings in proteins because the simulations tend to get trapped in a few of many local-minimum states. To overcome these difficulties, we have proposed new generalized-ensemble algorithms, such as multibaric- multithermal algorithm, partial multicanonical algorithm, and van der Waals replica exchange method. We apply these methods to proteins and peptides.

1. Temperature and Pressure Denaturation of Chignolin: Folding and Unfolding Simulation by Multibaric-Multithermal Molecular Dynamics Method

A multibaric-multithermal molecular dynamics (MD) simulation[1)] of a 10-residue protein, chignolin was performed to study its folding and unfolding thermodynamics and the denaturation mechanisms. All-atom model for the protein with Amber parm99SB force field were employed in explicit TIP3P water. This MD simulation covered wide ranges of temperature between T = 260 ~ 560 K and pressure between P = 0.1 ~ 600 MPa and sampled many conformations without getting trapped in local-minimum free-energy states. Folding events to the native β-hairpin structure occurred five times and unfolding events were observed four times. As temperature and/or pressure increases, fraction of the folded chignolin decreases. The partial molar enthalpy change ΔH and partial molar volume change ΔV upon unfolding were calculated as $\Delta H = 20.3 \pm 4.5$ kJ/mol and $\Delta V = -6.7 \pm 2.5$ cm^3/mol, respectively. These values agree well with recent experimental results.

Illustrating typical local-minimum free-energy conformations, folding and unfolding process of the chignolin was revealed, as shown in Figure 1. When it unfolds from the β-hairpin structure, only the C terminus or both C and N termini open first. It may undergo an α-helix or 3_{10}-helix structure and finally unfolds to the extended structure. Calculating radial distribution functions between chignolin backbone atoms and water oxygen atoms, hydrated water was found to decrease as temperature increases, but increase as pressure increases.

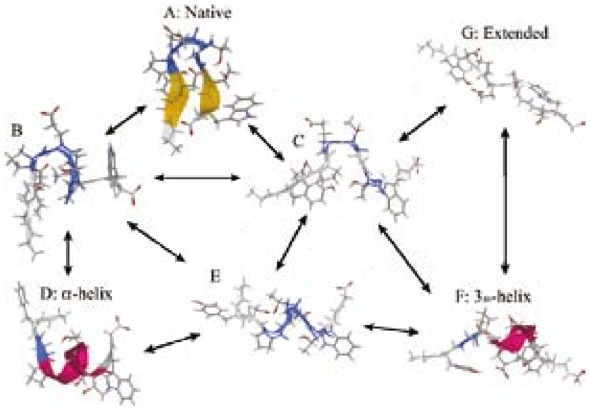

Figure 1. Typical conformations at local-minimum free-energy states and transition states obtained by the multibaric-multithermal MD simulation. The N terminus and the C terminus are on the left-hand side and on the right-hand side, respectively.

2. Length Dependence of Polyglycine Conformations in Vacuum[2)]

We performed replica-exchange molecular dynamics simulations of polyglycines in vacuum to investigate their conformational difference due to different numbers of residues. We employed the polyglycines of which the numbers of residues are 1 (PG1), 5 (PG5), 10 (PG10), and 15 (PG15). We discussed the conformations of the polyglycine molecules, which have the lowest potential energies in local minimum states. The polyglycines PG5 and PG10 often have helical structures. The helical structures of the polyglycine PG10 are β-helix structures. The PG15 have complicated tertiary structures. The tertiary structures have two β-hairpins in the N-terminal and C-terminal regions. A parallel β-sheet structure is also formed between the N-terminal side of the N-terminal β-hairpin and the C-terminal side of the C-terminal β-hairpin.

3. All-Atom Molecular Dynamics Simulations of Polyglutamine Dimers

Polyglutamine peptides form protofibrils composed by β-sheets. The aggregation of these protofibrils causes amyloidosis. It was not yet clear how polyglutamine aggregate and form β-sheets. For probing polyglutamine conformation in the β-sheets, we performed all-atom molecular dynamics simulations on pairs of the polyglutamine fragments in explicit water which consist of 10 repeated glutamine residues from parallel, anti-parallel and perpendicular initial conditions. This is the first work to simulate polyglutamine dimers in all-atom force field in explicit water. All of our simulation formed anti-parallel β-sheets and the number of β-bridges increased gradually, as shown in Figure 2. It indicates that polyglutamine dimer prefer anti-parallel β-sheet conformation than parallel conformation. This agrees well with previous researches by experiments and a coarse-grained molecular dynamics simulation. A free-energy barrier was also found at the structures with no β-bridge, which makes the transformation difficult between parallel and anti-parallel β-sheets.

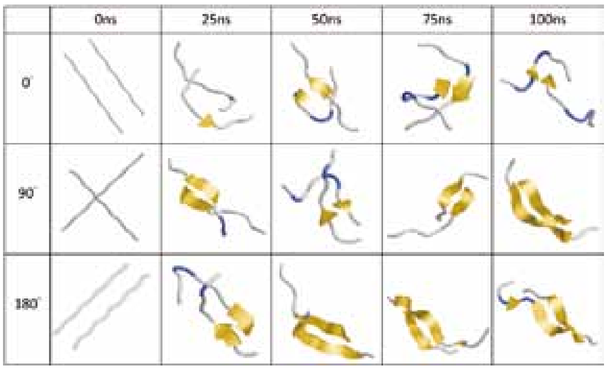

Figure 2. The snapshots at 0, 25, 50, 75, and 100 ns during the simulations. Angle 0°, 90°, and 180° stand for systems started from the parallel, perpendicular, and anti-parallel initial conditions, respectively.

References

1) H. Okumura and Y. Okamoto, *J. Phys. Chem. B* **112**, 12038–12049 (2008).
2) S. G. Itoh and H. Okumura, *J. Phys. Soc. Jpn.* **80**, 094801 (8 pages) (2011).

---

* carrying out graduate research on Cooperative Education Program of IMS with Nagoya University

Theory and Computation of Reactions and Properties in Solutions and Liquids

Department of Theoretical and Computational Molecular Science
Division of Computational Molecular Science

ISHIDA, Tateki Assistant Professor

Our researches are focused on the projects both on ultrafast photoinduced electron energy transfer in the excited state in solution and on ionic liquids (ILs). The project on photoinduced electron energy transfer processes in the excited state in solution concentrates the development of a theoretical method to describe solvent motion and dynamics accompanying electron energy transfer with the theoretical treatment to solvation processes and excited-state intramolecular electron transfer processes in solution we have developed. On the other hand, the purpose of ILs projects is to study specific interionic dynamics in ILs and to extract a new perspective on the physically and chemically unique characteristics of ILs.

1. Photoinduced Electron Energy Transfer Processes in the Excited State in Solution

We have proposed and developed a procedure for describing the time-dependent evolution of the electronic structure of a solute molecule in solution, coupling an electronic structure theory with a solution of the equation which governs the development of the fluctuation of solvent number density around a solute molecule in the formalism of an interaction site model. We extend this prescription for studying electron energy transfer processes in the excited state in solution. It is shown that the coupling between fast solvation dynamics and a fast intramolecular electron energy transfer is likely to play an important role in the emergence of photoinduced various and unique functionalities in biochemical and metal complex systems.

2. Molecular Dynamics Study of the Unique Dynamical Behavior in Ionic Liquids through Interionic Interactions[1)]

We have focused on the interionic dynamics of an IL, 1-Butyl-3-Methylimidazolium cation with the anion, $[PF_6]^-$, $[BMIm][PF_6]$, and have investigated the interionic interaction in the IL and the polarization effects on the system. From the results by Molecular dynamics simulations, it has been concluded that the cage effect in ILs could be reduced by many-body polarization effects.

3. Investigations of New Perspectives on the Characteristics of Ionic Liquids[2)]

We investigated the ultrafast dynamics in 1-butyl-3-methylimidazolium-based ionic liquids with two series of anions: (1) cyano-group substituted anions ($[SCN]^-$, $[N(CN)_2]^-$, and $[C(CN)_3]^-$) and (2) trifluoromethylsulfonyl group substituted anions ($[OTf]^-$, $[NTf_2]^-$, and $[CTf_3]^-$) by femtosecond Raman-induced Kerr effect spectroscopy. From the Fourier-transform Kerr spectra of the ionic liquids, the low-frequency spectrum of 1-butyl-3-methylimidazolium tricyanomethide indicates a low-frequency shift compared to the ILs with the other cyano-group substituted anions, due to the planar structures of the cation and the anion. The relative amplitude of the low-frequency band at approximately 20 cm^{-1} to the entire broad spectrum for the ionic liquids with trifluoromethylsulfonyl-group substituted anions is larger with the order $[OTf]^- < [NTf_2]^- \sim [CTf_3]^-$. These results can be attributed to the librational motion of anions and/or the coupling of the translational and reorientational motions.

Also, we have carried out the study of dicationic ILs with typical counter anions. (DOI 10.1021/jp206266e) The molecular dynamics simulations for dicationic ILs systems have been proceeded. The interionic interactions dependent on the unique spatial distribution of ionic species have been investigated including the analysis of velocity autocorrelation and polarizability time correlation functions and various dynamical properties based on the detailed analyses of collective motion of ionic molecules.

References

1) T. Ishida, *J. Non-Cryst. Solids* **357**, 454–462 (2011).
2) H. Fukazawa, T. Ishida and H. Shirota, *J. Phys. Chem. B* **115**(16), 4621–4631 (2011).

Visiting Professors

Visiting Professor
YOSHIZAWA, Kazunari *(from Kyushu University)*

Quantum Chemical Studies on Nanostructures and Enzymatic Reactions

In my group nanostructures and enzymatic reactions are studied by using quantum chemical calculations. The first topic is concerned about functions of metal ions in the active sites of enzymes and catalysts. The direct conversion of methane to methanol under physiological conditions, the bare MO^+ complex in the gas phase, Fe-ZSM-5 zeolite, and B_{12}-dependent diol dehydratase, for example, are studied. The second topic is chemical understanding of electron transport properties in molecular junctions, in which two electrodes have contact with a molecule, in terms of the orbital concept. We found that the phase and amplitude of the HOMO and LUMO of molecules determine essential properties of the electron transport in them. The derived rule to predict single molecules' essential transport properties was recently confirmed by collaboration with experimental groups.

Visiting Professor
SUGITA, Yuji *(from RIKEN)*

Molecular Dynamics Simulations of Large Conformational Changes in Membrane Proteins

Due to the recent advances in molecular biology and structural biology, we have more than 300 atomic coordinates of membrane proteins in protein data bank (PDB). In our research teams, we have developed simulation techniques to simulate membrane proteins with explicit solvent and lipid bilayers and carried out large-scale molecular dynamics simulations of the sarcoplasmic reticulum Ca^{2+}-ATPase (calcium ion pump), sec translocons, and so on. In the simulations of calcium ion pump, we have successfully shown the differences of the calcium-binding affinity between wild-type and two mutant ATPases, namely, Glu771Gln, and Glu908Gln. Furthermore, we have shown that the calcium affinity at the transmembrane binding sites has close relationship with the shielding of bulk water from the luminal side. This provides new insight into the mechanisms of gating of ion pathways in cation pumps.

RESEARCH ACTIVITIES

Photo-Molecular Science

We study the interaction between molecules and optical fields with its possible applications to active control of molecular functionality and reactivity. We also develop novel light sources to promote those studies. Two research facilities, the Laser Research Center for Molecular Science and the UVSOR, closely collaborate with the Department.

The core topics of the Department include ultrahigh-precision coherent control of gas- and condensed-phase molecules, high-resolution optical microscopy applied to nanomaterials, synchrotron-based spectroscopy of core-excited molecules and solid-state materials, vacuum-UV photochemistry, and the development of novel laser- and synchrotron-radiation sources.

Development of Advanced Near-Field Spectroscopy and Application to Nanometric Systems

Department of Photo-Molecular Science
Division of Photo-Molecular Science I

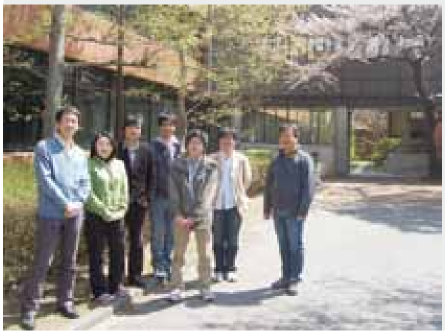

OKAMOTO, Hiromi	Professor
JEONG, Dae Hong	Visiting Associate Professor
NARUSHIMA, Tetsuya	Assistant Professor
NISHIYAMA, Yoshio	IMS Research Assistant Professor
HARADA, Yosuke	Post-Doctoral Fellow
LIM, Jong Kuk	Post-Doctoral Fellow
WU, Huijun	Graduate Student
OCHIAI, Takao	Graduate Student*
ISHIKAWA, Akiko	Technical Fellow
NOMURA, Emiko	Secretary

There is much demand for the study of local optical properties of molecular assemblies and materials, to understand mesoscopic phenomena and/or to construct optoelectronic devices in the nanometric scale. Scanning near-field optical microscopy (SNOM) is an imaging method that enables spatial resolution beyond the diffraction limit of light. Combination of this technique with various advanced spectroscopic methods may offer a direct probe of dynamical processes in nanomaterials. It may provide essential and basic knowledge for analyzing origins of characteristic features and functionalities of the nanometric systems. We have constructed apparatuses of near-field spectroscopy for excited-state studies of nanomaterials, with the feasibilities of nonlinear and time-resolved measurements. They enable near-field measurements of two-photon induced emission and femtosecond transient transmission, in addition to conventional transmission, emission, and Raman-scattering. Based on these methods, we are investigating the characteristic spatiotemporal behaviors of various metal-nanoparticle systems and molecular assemblies.

1. Visualization of Localized Optical Fields and Plasmon Wavefunctions in Metal Nanostructures

We recently reported that wavefunctions of localized plasmon resonances of chemically synthesized metal (Au and Ag) nanoparticles are visualized by near-field transmission or two-photon excitation measurements.1) The same methods were also applied to Au nanoparticle assemblies to visualize confined optical fields.1) It was revealed for the dimers that highly localized optical field is generated at the interstitial sites between the particles. In many-particle assemblies, the localized fields were especially intensified at the rim parts of the assemblies, and such a characteristic field distribution has been attributed to interaction between plasmon excitations induced on the particles.2)

We have extended the studies to metal nanostructures manufactured by the electron-beam lithography technique, in collaboration with researchers of other institution, or other top-down fabrication techniques, with which structures that are difficult to obtain with the chemical methods can be available. As an example, near-field properties of nano-void structures, opened on thin gold metallic films on glass substrates, were characterized, and the field distributions in the vicinities of the voids were visualized.3) In circular void chain structures, we found that confined optical fields were generated in the interstitial sites between voids under some circumstances (Figure 1). The field distributions were analyzed based on the electromagnetic theories and calculations. The observed and calculated field distribution was discussed in relation to Babinet's principle in optics, which gives general relation between electromagnetic field distributions for complementary nanostructures made of thin conductors, such as a nanoparticle assembly and a nano-void assembly.

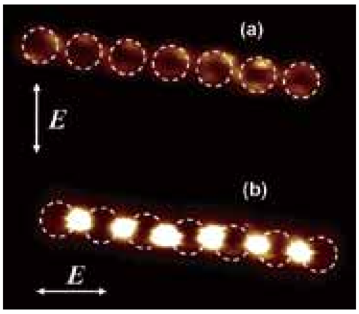

Figure 1. Near-field two-photon excitation images of a nanovoid chain opened on a Au film (thickness ~20 nm).3) The diameter of the void was ~400 nm. The incident polarization was nearly perpendicular (a) and parallel (b) to the chain. Excitation: 785 nm.

Such a study is essential as a basis for designing unique optical properties and functions of metal nanostructures, and their applications to highly sensitive spectroscopic methods and exotic photochemical fields, as well as to nanoscale optical waveguids.

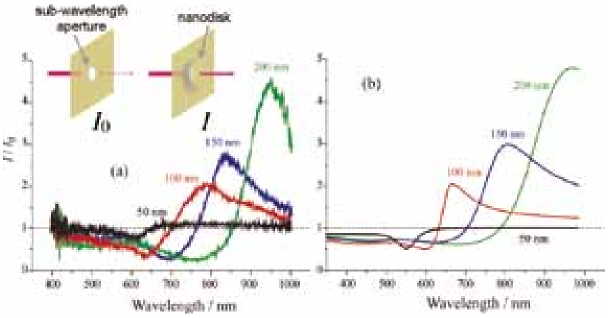

Figure 2. Transmittance spectra of capped nanoapertures, (a) experimental and (b) model calculation. The inset shows the schematic models of an uncapped and a capped nanoapertures.

2. Anomalous Light Transmission through Capped Nanoapertures

In the course of near-field studies on metal nanodisks fabricated on glass substrates by electron-beam lithography, we examined light intensity transmitted through a nanometer-scale aperture opened on an opaque metallic screen. When the aperture is obscured by an opaque metallic disk (cap) with a larger diameter than the aperture, the transmitted light was found to be, paradoxically, even stronger than that without the disk.4)

We investigated spectroscopic characteristics of light transmission through a nanoaperture on a gold film with a diameter of ~100 nm (Figure 2, inset, left; apertured near-field probe, in practice) and that capped with gold nanodisks (diameter 50–200 nm) at a distance of ~30 nm from the aperture (Figure 2, inset, right). The transmittance through the capped aperture is defined as the ratio between intensities for the capped aperture (I) and for the aperture without the disk (I_0) and is plotted in Figure 2(a). In the long wavelength region, the transmittance through the capped aperture exceeds 1, and surprisingly, the maximum transmittance becomes even higher for larger disks. We analyzed the spectra based upon a theoretical model, and it turned out that the phenomenon arise from the property of localized plasmon resonances: The anomalous transmission is due to highly efficient performance of the nanodisks for conversion between near-field and far-field radiations.

3. Nonlinear Effects in Optical Trapping

The optical trapping technique has been widely used in various areas to manipulate particles, cells, and so forth. The principle of trapping is based on the interaction between optical electric fields and induced linear polarizations. In the course of the studies on behavior of gold nanoparticles under pulsed laser fields, we have found a novel phenomenon of optical trapping of spherical gold nanoparticles arising from nonlinear polarization when we trap the nanoparticles by ultrashort near-infrared laser pulses.5) That is, the stable trap site (usually appears in the center of the focused beam) is split into two equivalent positions, and the split trap positions are aligned along the direction of the incident laser polarization. The split distance depends on the trapping-laser power and wavelength. We have found that the results were successfully interpreted in terms of the nonlinear polarization caused by the femtosecond pulses. This is the first report that treats the nonlinear effects in optical trapping.

Figure 3. Two gold nanoparticles trapped by ultrashort pulses. Two particles are trapped separately and aligned along the incident laser polarization (arrows).

4. Construction of Apparatuses for Nonlinear and Ultrafast Near-Field Spectroscopy

In previous studies we achieved ultrafast near-field imaging with a time resolution of ~100 fs.1) To further extend the dynamical studies of plasmons, we are now developing an apparatus that achieves near-field time-resolved measurements with < 20 fs time resolution. We have also constructed an apparatus for near-field/far-field microscopic nonlinear optical measurements based on the technique of atomic-force microscope.

5. Near-Field Imaging of Organic Molecular Assemblies and Hybrid Systems

We are studying nanometric structures and optical properties of organic molecular assemblies such as LB films of functional conjugated molecules, and hybrid systems consist of metal nanoparticles and organic functional materials, mainly as collaborations with other research groups.

References

1) H. Okamoto and K. Imura, *Prog. Surf. Sci.* **84**, 199–229 (2009).

2) H. Okamoto, K. Imura, T. Shimada and M. Kitajima, *J. Photochem. Photobiol., A* **221**, 154–159 (2011).

3) S. I. Kim, K. Imura, S. Kim and H. Okamoto, *J. Phys. Chem. C* **115**, 1548–1555 (2011).

4) K. Imura, K. Ueno, H. Misawa and H. Okamoto, *Nano Lett.* **11**, 960–965 (2011).

5) Y. Jiang, T. Narushima and H. Okamoto, *Nat. Phys.* **6**, 1005–1009 (2010).

---

* carrying out graduate research on Cooperative Education Program of IMS with University of Tsukuba.

Design and Reconstruction of Molecular Quantum States of Motion

Department of Photo-Molecular Science
Division of Photo-Molecular Science I

OHSHIMA, Yasuhiro	Professor
MIZUSE, Kenta	Assistant Professor
HAYASHI, Masato	Post-Doctoral Fellow
MIYAKE, Shinichiro	Graduate Student
INAGAKI, Itsuko	Secretary

Molecules are vital existence. In a gas-phase ensemble at room temperature, they are, in an average, flying away by a few hundred meters, making turns almost reaching to 10^{11} times, and shaking themselves more than 10^{13} times within the duration of only one second. The ultimate goal this research group has been aiming to is to capture the lively figures of molecules moving in such a dynamic manner and to have a perfect command over the molecular motions. Here lasers with ultimate resolution in time and energy domains are employed complementally and cooperatively for this purpose.

1. Unveiling the Nonadiabatic Rotational Excitation Process in a Symmetric-Top Molecule Induced by Two Intense Laser Pulses[1)]

When gaseous molecules are irradiated by an intense nonresonant ultrafast laser pulse, rotation of molecules is coherently excited via the interaction with the molecular anisotropic polarizability, to create a rotational quantum wave packet (WP). We has developed a method for exploring such a nonadiabatic rotational excitation (NAREX) process in a quantum-state resolved manner, and reported rotational-state distributions after the impulsive excitation with a fundamental output of a femtosecond (fs) Ti:Sapphire laser.[2,3)]

We made an extended study for unveiling the NAREX process in symmetric-top molecules. Benzene molecules have been taken as a sample. The initial state distribution was restricted mostly to the five lowest rotational levels in different nuclear-spin manifolds by an extensive adiabatic cooling with the rotational temperature well below 1 K, and distributions after the interaction with a fs double-pulse pair (3–5 TW/cm^2 each with 160 fs duration) with time delays were probed by employing resonant enhanced two-photon ionization (R2PI) *via* the $S_1 \leftarrow S_0$ 6_0^1 vibronic transition with nanosecond (ns) dye laser pulses. Populations of 10 rotational levels with J ranging from 0 to 4 and K from 0 to 3 were examined to show an oscillatory dependence on the time delay between the two pulses. Fourier analysis of the beat signals provides the coupling strengths between the constituent levels of the rotational WPs created by NAREX. These data agrees well with the results from quantum mechanical calculations, evidencing stepwise excitation pathways in the wave packet creation with $\Delta J = 2$ for $K = 0$ stack while $\Delta J = 1$ and 2 in $K > 0$ stacks.

2. Controlling the Sense of Molecular Rotation: Classical vs Quantum Analysis[4)]

The anisotropy of molecular system is represented as a non-uniform distribution of projections, M, of angular momentum, J, onto a space-fixed (Z) axis. The system is designated as being *oriented* when the populations for $+M$ and $-M$ are different. In the classical vector model, the + or – orientation corresponds to clockwise or counter-clockwise rotation, respectively. We have shown that a pair of linearly-polarized intense ultrafast pulses creates molecular ensembles with oriented rotational angular momentum, when the delay and the mutual polarization between the laser fields are appropriately arranged.[5)]

We have further undertaken a comparative study of the classical and quantum aspects of the underlying mechanism of the effect. Good quantitative agreement is found between the classical description of the process and the rigorous quantum mechanical analysis at the relevant experimental conditions. Both approaches predict the same optimal values for the delay between pulses and the angle between them, and deliver the same magnitude of the induced oriented angular momentum of the molecular ensemble. As expected, quantum and classical analysis substantially deviate when the delay between pulses is comparable with the period of quantum rotational revivals. However, time-averaged characteristics of the excited molecular ensemble are equally good described by these two approaches. This is illustrated by calculating the anisotropic time-averaged angular distribution, which reflects persistent confinement of the molecular axes to the rotation plane defined by two polarization vectors of the pulses.

3. Reconstruction of the Rotational Wave Packet Created by NAREX and Ultrafast State-Distribution Control

The fs-pump and ns-probe approach has been also adopted for a detailed study on characterization and control of the rotational WP in NO. For double fs-pulse excitation, the population of each rotational state showed oscillatory change against the time delay between the two pulses. As has been shown previously,6) the delay dependence pertinent to the initially populated state allowed us to determine the amplitude and phase of each eigenstate that constitutes the rotational WP. The experimental results, in particular, the systematic phase shifts against J, represented a clear signature of bifurcated excitation pathways in the WP creation, which is characteristic to linear molecules in a doubly degenerate vibronic state. We have also shown that the final distribution can be concentrated into a narrow range of states if the time delay between the two pulses is properly arranged. For instance, almost 80% can be repopulated in the initial $J = 1/2$ state. Highly focused population has been achieved also for $J = 3/2$ and 5/2. The experimental finding has demonstrated the capability of state-distribution control in an ultrafast time scale (within several tens of picoseconds).

4. Coherent Intermolecular-Mode Excitation of NO–Ar by Nonresonant Intense Femtosecond Laser Fields

Nonadiabatic interactions with a nonresonant ultrafast laser field can coherently excite also molecular vibration. Here, vibrational distribution after nonadiabatic vibrational excitation (NAVEX) is probed in a quantum-state resolved manner. The method has been applied to NO–Ar. R2PI spectrum of NO–Ar associated to the monomer A–X (0,0) transition exhibited a number of hot bands when the fs pump pulse was applied. These hot band transitions are assigned to those from vibrationally excited states pertinent to intermolecular modes, of which excitation energies range in 4–30 cm^{-1}. Thus we have successfully probed the intermolecular vibrational energy levels up to 1/3 of the total binding energy of NO–Ar, which is estimated to be *ca.* 90 cm^{-1}. When the cluster was excited with a pair of fs pulses, the intensities of monitored vibronic bands changed oscillatory against the delay between the two pulses. These results indicate the creation of a quantum WP pertinent to intermolecular vibrations in the electronic ground state. Real-time WP propagation was calculated by numerically solving the time-dependent Schrödinger equation on the intermolecular potential energy surface.

5. High-Resolution Laser Spectroscopy of Benzene Clusters with He Atoms and H_2 Molecules

Molecular clusters containing benzene are prototypical systems for elucidating the intermolecular interaction pertinent to aromatic rings. We are now focusing on clusters of benzene attached by small numbers of atoms and molecules. Specifically, high-resolution electronic spectra of benzene–$(\mathrm{He})_n$ and –$(\mathrm{H_2})_n$ (n = 1, 2) have been examined via two-color R2PI in the vicinity of the monomer S_1–S_0 6_0^1 band. We employed a tripled output from a ns pulsed dye amplifier, which was injection-seeded by the CW output from a Ti:Sapphire laser, as an excitation source. Owing to the narrow band width (~250 MHz) of the laser system and the efficient rotational cooling down to 0.3 K by implementing a high-pressure pulsed valve, rotational structures have been fully resolved. The observed spectra shows unambiguously that He and H_2 are located above the center of the benzene molecular plane (for the both sides in the case of n = 2), and the H_2 molecular axes are perpendicular to the plane. The rotational constants thus determined set the distances of He and H_2 above the plane to be: 3.602 (+0.063) Å and 3.477 (+0.131) Å, respectively, where values in parentheses represent the change by the excitation from S_0 to S_1. Several vibronic bands associated to excitation of intermolecular vibrations have also been observed for all the clusters examined. The vibrational frequencies of benzene(S_1)–He are derived as: 17 and 13 cm^{-1} for the intermolecular stretch and bend modes, respectively. The values in the complex with H_2 are: 48 cm^{-1} for the stretch, while 34 and 39 cm^{-1} for the two bend modes. The vibronic bands of benzene–He exhibit tunneling splitting due to a large-amplitude migration of He above and below the benzene molecular plane. This finding is matched with the prediction based on a high-level *ab initio* calculation.

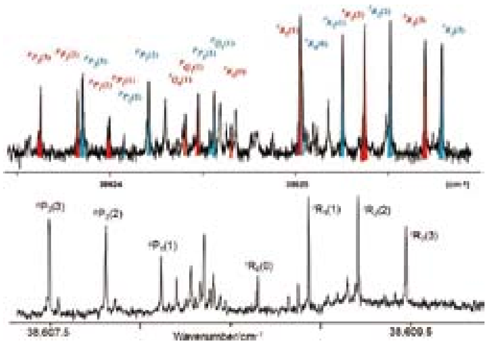

Figure 1. High-resolution excitation spectra of C_6H_6–He: (bottom) the $S_1 \leftarrow S_0$ 6_0^1 band, (top) the intermolecular-stretch excited band. Each rotational line is split into two (indicated in red and blue) due to quantum tunneling.

References

1) D. Baek, H. Hasegawa and Y. Ohshima, *J. Chem. Phys.* **134**, 224302 (10 pages) (2011).

2) H. Hasegawa and Y. Ohshima, *Phys. Rev. A* **74**, 061401 (4 pages) (2006).

3) H. Hasegawa and Y. Ohshima, *Chem. Phys. Lett.* **454**, 148–152 (2008).

4) Y. Khodorkovsky, K. Kitano, H. Hasegawa, Y. Ohshima and I. Sh. Averbukh, *Phys. Rev. A* **83**, 023423 (10 pages) (2011).

5) K. Kitano, H. Hasegawa and Y. Ohshima, *Phys. Rev. Lett.* **103**, 223002 (4 pages) (2009).

6) H. Hasegawa and Y. Ohshima, *Phys. Rev. Lett.* **101**, 053002 (4 pages) (2008).

Development of High-Precision Coherent Control and Its Applications

Department of Photo-Molecular Science
Division of Photo-Molecular Science II

OHMORI, Kenji	Professor
KATSUKI, Hiroyuki	Assistant Professor
TAKEI, Nobuyuki	Assistant Professor
GOTO, Haruka	Post-Doctoral Fellow
NAKAGAWA, Yoshihiro	Graduate Student
KOYASU, Kuniaki	Graduate Student
INAGAKI, Itsuko	Secretary
YAMAGAMI, Yukiko	Secretary

Coherent control is based on manipulation of quantum phases of wave functions. It is a basic scheme of controlling a variety of quantum systems from simple atoms to nanostructures with possible applications to novel quantum technologies such as bond-selective chemistry and quantum computation. Coherent control is thus currently one of the principal subjects of various fields of science and technology such as atomic and molecular physics, solid-state physics, quantum electronics, and information science and technology. One promising strategy to carry out coherent control is to use coherent light to modulate a matter wave with its optical phase. We have so far developed a high-precision wave-packet interferometry by stabilizing the relative quantum phase of the two molecular wave packets generated by a pair of femtosecond laser pulses on the attosecond time scale. We will apply our high-precision quantum interferometry to gas, liquid, solid, and surface systems to explore and control various quantum phenomena.

1. Strong-Laser-Induced Quantum Interference1)

Molecules are expected to be promising information devices. Theoretical proposals have been made for logic gates with a molecular wave packet modulated by a strong femtosecond laser pulse. However, it has not yet been observed how this changes the population of each eigenstate within the wave packet. Here we demonstrate direct observation of the population beating clearly as a function of the delay of the strong laser pulse. The period is close to the recurrence period of the wave packet, even though a single eigenstate should have no information on the wave-packet motion. This unusual beat arises from quantum interference among multiple eigenstates combined on a single eigenstate. This new concept, which we refer to as 'strong-laser-induced interference,' is not specific to molecular eigenstates, but universal to the superposition of any eigenstates in a variety of quantum systems, being a new tool for quantum logic gates, and providing a new method to manipulate wave packets with femtosecond laser pulses in general applications of coherent control.

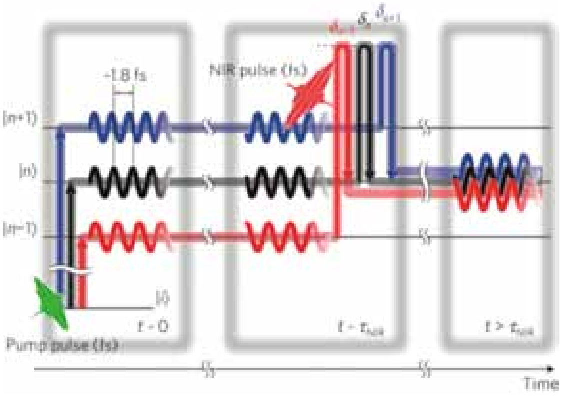

Figure 1. Starting from a common initial state *i*, there are multiple pathways given by the pump and strong near-infrared (NIR) laser pulses to the common final state *n*. Those multiple pathways interfere with each other. The amounts of phase shifts during the NIR pulse are indicated as δ_{n-1}, δ_n, and δ_{n+1}.

2. Optical Manipulation of Coherent Phonons in Superconducting $YBa_2Cu_3O_{7-\delta}$ Thin Films2)

The coherent phonons of $YBa_2Cu_3O_{7-\delta}$ are believed to be strongly coupled to its superconductivity. Controlling the phonons below its transition temperature, therefore, may serve as a promising scheme of the control of superconductivity. Here we demonstrate optical manipulation of the Ba–O and Cu–O vibrations in a thin-film $YBa_2Cu_3O_{7-\delta}$ below its transition temperature using a pair of femtosecond laser pulses. The interpulse delay is tuned to integral and half-integral multiples of the oscillation period of a specific phonon mode (Ba–O or Cu–O vibration) to enhance and suppress its amplitude, respectively.

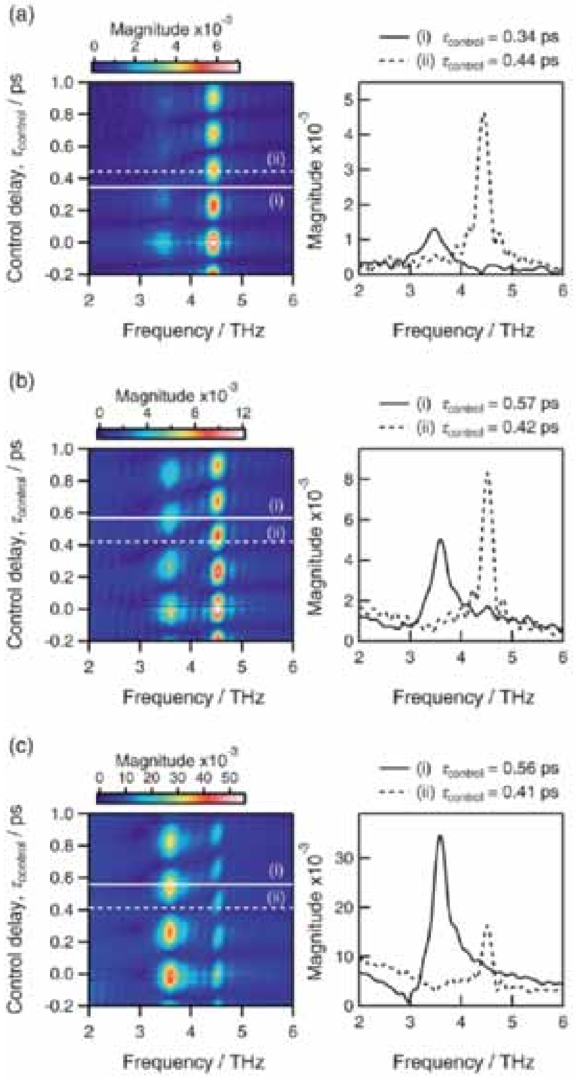

Figure 2. Fast-Fourier-transform of the temporal evolutions of the coherent phonons induced by a pair of femtosecond laser pulses in $YBa_2Cu_3O_{7-\delta}$ thin films with temperatures (a) 296 K, (b) 78 K, and (c) 8 K. They are plotted as functions of the interpulse delay $\tau_{control}$ in the left column. The right column shows cross sections along the solid (i) and broken (ii) lines in the left column at each temperature.

References

1) H. Goto, H. Katsuki, H. Ibrahim, H. Chiba and K. Ohmori, *Nat. Phys.* **7**, 383–385 (2011).
   Highlighted by Nat. Phys. **7**, 373–374 (2011).
   Highlighted by Nat. Photonics **5**, 382–383 (2011).
2) Y. Okano, H. Katsuki, Y. Nakagawa, H. Takahashi, K. G. Nakamura and K. Ohmori, *Faraday Discuss.* **153**, 375–382 (2011). (invited paper).

Awards

KATSUKI, Hiroyuki; The Young Scientist’s Prize of The Commendation for Science and Technology by the Minister of Education, Culture, Sports, Science and Technology, Japan.

KATSUKI, Hiroyuki; MORINO Foundation research award.

Molecular Inner-Shell Spectroscopy: Local Electronic Structure and Intermolecular Interaction

Department of Photo-Molecular Science
Division of Photo-Molecular Science III

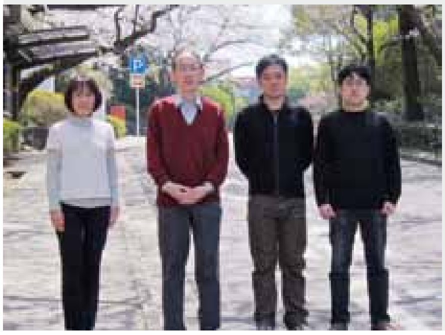

KOSUGI, Nobuhiro	Professor
YAMANE, Hiroyuki	Assistant Professor
NAGASAKA, Masanari	Assistant Professor
NAKANE, Junko	Secretary

In order to reveal local electronic structures and weak intermolecular interactions in molecular solids, liquids, and clusters, we are developing and improving several kinds of soft X-ray spectroscopic techniques such as X-ray photoelectron spectroscopy (X-ray PES, XPS), X-ray absorption spectroscopy (XAS), resonant Auger electron spectroscopy (RAS), X-ray emission spectroscopy (XES), resonant XES (RXES), and resonant inelastic X-ray scattering (RIXS), at UVSOR in-vacuum undulator beamlines BL-3U and BL-6U with some international collaboration programs, and also an original *ab initio* quantum chemical program package GSCF, which is optimized to calculation of molecular inner-shell processes.

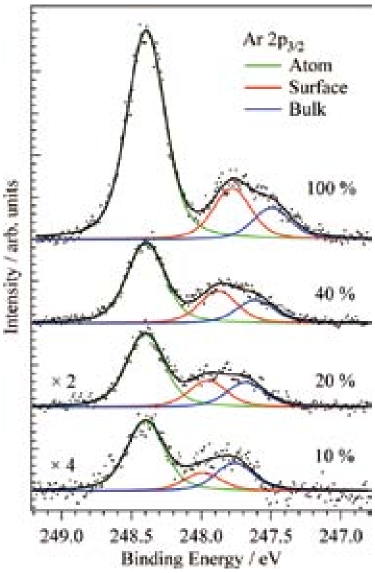

Figure 1. Ar $2p_{3/2}$ XPS spectra for mixed Ar-N_2 clusters prepared from different mixing ratio of Ar. The surface and bulk sites of the mixed clusters are separately obtained by a fitting procedures.

1. Structures of Small Mixed Ar-N_2 Clusters Studied by Soft X-Ray Photoelectron Spectroscopy[1]

Figure 1 shows Ar $2p_{3/2}$ XPS spectra for Ar and mixed Ar-N_2 clusters of different compositions. The surface and bulk sites of the clusters are distinguished by a fitting procedure. The cluster size of 200 corresponds to icosahedral multilayer structures with 4 or 5 layers. The intensity ratio of the surface and bulk sites observed for the Ar $2p_{3/2}$ XPS spectra of the pure (100%) Ar_{200} cluster is consistent with such icosahedral multilayer structures. On the other hand, in 10% Ar, the intensity of the surface sites is smaller than that of the bulk sites. This intensity ratio suggests a core-shell structure, where the Ar aggregates are located in the bulk and are covered by a N_2 shell. We have roughly estimated the composition of N_2 bound in clusters from the partial pressure of N_2, and confirmed that the surface-to-bulk ratio of Ar is consistent with a core-shell structure, where Ar is covered by N_2. These core-shell structures are also observed in expansions containing 20 and 40% Ar.

2. Electronic Structure of Liquid Methanol Studied by Carbon K-Edge Soft X-Ray Absorption Spectroscopy[2]

Figure 2 shows C K-edge XAS spectra of molecular (gas) and liquid methanol at 25 °C. Two peaks around 288 and 289.5 eV and several Rydberg states are observed in the molecular spectra. The 288 eV and 289.5 eV peaks contain O–H and C–H components, respectively, and the 292.5 eV peak contains a σ* C–O component. Our C K-edge XAS spectrum of liquid methanol shows a simple structure with three contributions around 288.5, 290, and 293 eV as shown in

Figure 2(b).

The peak around 288.5 eV in liquid methanol is shifted to higher photon energy compared to that of methanol gas. The energy shift (0.53 eV) would be caused by the formation of the hydrogen bonding networks between methanol molecules. The peak around 290 eV in liquid methanol is also shifted to higher photon energy, but the energy shift (0.20 eV) is smaller than in the first band. This may be explained by a dominant contribution from the hydrophilic OH component in the first band. The peak around 293 eV does not show a noticeable difference between gas and liquid because the σ* (C–O) orbital is not influenced by the hydrogen bonding network.

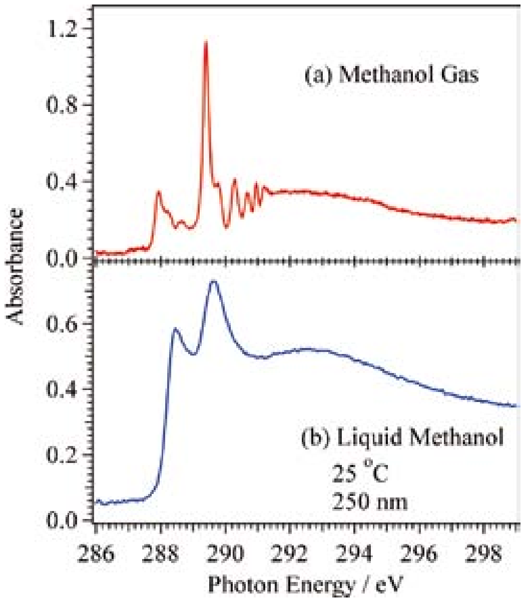

Figure 2. Carbon K-edge XAS spectra for (a) methanol gas and (b) liquid methanol at 25 °C. The thickness of liquid methanol layer is estimated to be 250 nm.

3. Very Narrow Intermolecular Electronic Band Dispersion in a Crystalline Film of Zn-Phthalocyanine[3)]

The electronic band dispersion, energy *versus* wave vector: $E(\boldsymbol{k})$, is a fundamental parameter to understand electric properties of solids such as hole mobility (μ_h). In the field of organic semiconductors, study of the intermolecular $E(\boldsymbol{k})$ shows a rapid progress due to the needs of the interpretation of the charge transport mechanism in molecular electronic devices. However, due to very weak intermolecular interaction and difficulty in preparing crystallized films appropriate for the $E(\boldsymbol{k})$ measurement, the observation of the intermolecular $E(\boldsymbol{k})$ has been limited in the case of high-μ_h materials. In order to elucidate and control the functionality of organic semiconductors, a systematic and quantitative experiment on the intermolecular interaction is essential. In this work, we have succeeded to observe a very narrow intermolecular $E(\boldsymbol{k})$ in crystalline films of Zn-phthalocyanine (ZnPc), which is one of the promising materials in the field of organic electronics.

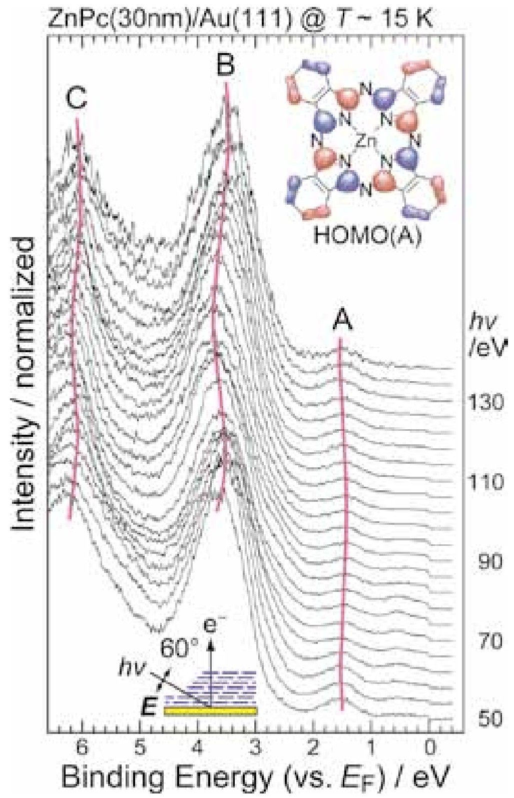

Figure 3. The $h\nu$ dependent angle-resolved PES spectra (4 eV step) at the normal emission for the crystalline ZnPc films on Au(111) at 15K.

Figure 3 shows $h\nu$ dependent angle-resolved PES (ARPES) spectra at the normal emission for the ZnPc crystalline film on Au(111) at 15 K. Since the ZnPc crystalline film on Au(111) shows a Stranski-Krastanov growth mode, there are the remanent substrate signal such as a Fermi edge, which we can use for the fine $h\nu$ calibration. For the ZnPc-derived peaks A, B, and C, we have observed a clear dispersive behavior with $h\nu$, wherein (i) the periodicities of A–C are the same in the $\boldsymbol{k}$ space and (ii) the bandwidth of peak A, originating from the highest occupied molecular orbital (HOMO), is 120 meV.

The present observation clearly indicates that the band-like transport is realized in the phthalocyanine films by the control of the geometric film structure. Moreover, the present result can be a benchmark for the systematic study on the intermolecular interaction, *e.g.*, intermolecular $E(\boldsymbol{k})$ as a function of the central metal atom in the phthalocyanine molecule, which enables to discuss experimentally the intermolecular interaction in terms of the intermolecular distance and the molecular orbital symmetry.

References

1) M. Nagasaka, E. Serdaroglu, R. Flesch, E. Rühl and N. Kosugi, to be published.
2) M. Nagasaka and N. Kosugi, to be published.
3) H. Yamane and N. Kosugi, to be published.

Photoabsorption and Photoionization Studies of Fullerenes and Development of High-Efficiency Organic Solar Cells

Department of Photo-Molecular Science
Division of Photo-Molecular Science III

MITSUKE, Koichiro	Associate Professor
KATAYANAGI, Hideki	Assistant Professor
LE, Hong Quang	Post-Doctoral Fellow
PRAJONGTAT, Pongthep	Research Fellow
MORENOS, Lei Angeli S.	Visiting Scientist
BASHYAL, Deepak	Graduate Student
ASARI, Chie	Technical Fellow
SHIMIZU, Atsuko	Secretary

We have observed the formation of multiply-charged photoions from gaseous fullerenes or aromatic hydrocarbons irradiated with synchrotron radiation at $h\nu$ = 25 to 200 eV. We thus studied the mechanisms and kinetics of consecutive C_2-release reactions on the basis of (i) the yield curves for the fragments $C_{60(70)-2n}{}^{z+}$ ($n \geq 1$, z = 1–3) as a function of the primary internal energy and (ii) the three dimensional velocity distributions of the fragments. Last year the velocity distributions of $C_{60-2n}{}^{z+}$ and $C_{70-2n}{}^{z+}$ were measured for the first time. Concepts of the microcanonical temperature and Arrhenius-type rate constants for individual C_2 ejection steps allowed us to compare the experimental total average kinetic energy with theoretical kinetic energy release predicted from the “model free approach” developed by Klots.

In the second topic we have fabricated dye-sensitized solar cells (DSSCs) containing ruthenium dye and iodide electrolyte and measured their short-circuit current and the intensity of the transmitted light to estimate the wavelength dependence of the incidence photon-to-current conversion efficiency (IPCE) and photoabsorbance (ABS) in the range of 300 to 1000 nm. In addition, we evaluated the quantum yield (APCE) of DSSCs for the electron injection from the excited orbital of Ru dye to the conduction band of TiO_2 nanoparticles. Our final goal is to develop DSSCs with high performance and long lifetime by improving ABS and APCE mainly in the near infrared region.

1. Mass-Analyzed Velocity Map Imaging of Photofragments from C_{70} [1)]

The velocity distributions of the fragments produced by dissociative photoionization of C_{70} have been measured at several photon energies in the extreme UV region, by using a flight-time resolved velocity map imaging (VMI) technique combined with a high-temperature molecular beam and synchrotron radiation. Average kinetic energy release was estimated for the six reaction steps of consecutive C_2 emission, starting from $C_{70}{}^{2+} \rightarrow C_{68}{}^{2+} + C_2$ to $C_{60}{}^{2+} \rightarrow C_{58}{}^{2+} + C_2$. The total kinetic energy generated in each step shows a general tendency to increase with increasing $h\nu$, except for the first and fifth steps. This propensity reflects statistical redistributions of the excess energy in the transition states for the above fragmentation mechanism. Analysis based on the finite-heat-bath theory predicts the detectable minimum cluster sizes at the end of the C_2–emission decay chain. They accord well with the minimum sizes of the observed ions, if the excess energy in the primary $C_{70}{}^{2+}$ is assumed to be smaller by ~15 eV than the maximum available energy. The present VMI experiments reveal remarkably small kinetic energy release in the fifth step, in contradiction to theoretical predictions, which suggests involvement of other fragmentation mechanisms in the formation of $C_{60}{}^{2+}$.

2. Velocity Map Imaging for Photoionization of Polycyclic Aromatic Hydrocarbons

We have demonstrated the versatility of our apparatus in photoionization study of various nonvolatile substances, by taking an example of complicated dissociation of sumanene $C_{21}H_{12}$ and coronene $C_{24}H_{12}$ in the extreme UV. Though their chemical reactions are sometimes discussed by analogy with those of C_{60}, a great difference in the velocity distribution has been observed between the fragment ions from C_{60} and those from sumanene. The appearance $h\nu$ values for $C_{60-2n}{}^{z+}$ are higher by 30–33 eV than their thermochemical thresholds for dissociative ionization of C_{60}. Usually, the relative abundance of $C_{60-2n}{}^{z+}$ is two orders of magnitude lower than that of the parent $C_{60}{}^{z+}$. In contrast, the y–t map of sumanene in Figure 1 suggests prompt coulomb explosion of $C_{21}H_{12}{}^{z+}$ (z = 2 and 3) into singly-charged fragments followed by stepwise C_2 ejection. This argument appears to hold true in the case of photodissociation of coronene $C_{24}H_{12}$.

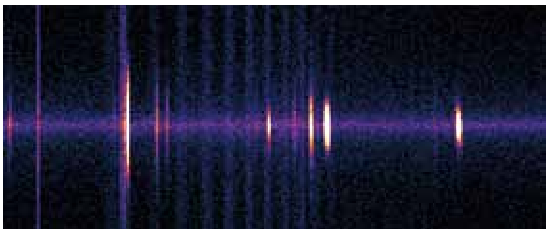

Figure 1. Map of y–t of the photoions from $C_{21}H_{12}$. The y and t coordinates are proportional to the y component of the ion velocity and the square root of mass-to-charge ratio m/z, respectively.

3. Photoexcitation and Electron Injection Processes in Azo Dyes Adsorbed on Nanocrystalline TiO_2 Films[3)]

Dye-sensitized solar cells were fabricated using eight azo dyes which have different positions and/or numbers of carboxyl and hydroxyl groups. The short-circuit current density, photoabsorbance, absorptance and quantum yield for dyes-to-TiO_2 electron injection were measured by photons ranging from 380 to 800 nm. X-ray and ultraviolet photoelectron spectroscopy of the photovoltaic electrodes were also conducted. The photon-to-current conversion efficiency of the cells was found to depend mostly on the relative position of the lowest unoccupied molecular orbital of the adsorbed dyes and partly by their concentration on the TiO_2 nanoparticles.

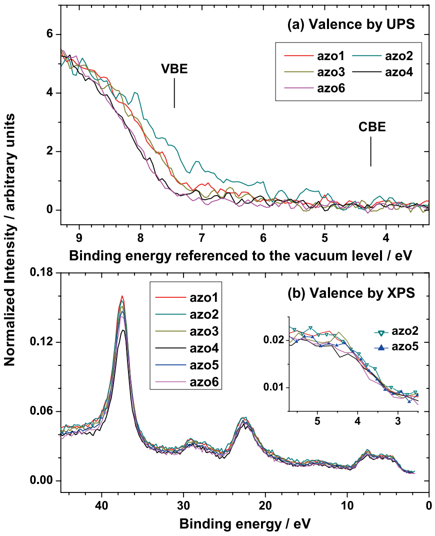

Figure 2. Ionization of valence and Ti 3p electrons of the TiO_2 film covered with six azo dyes on the working electrodes observed by photoelectron spectroscopy.

4. Efficient Dye-Sensitized Solar Cells Made from TiO_2 Nanoparticles Powder, VP P90[4)]

Dye sensitized solar cells (DSSCs) were fabricated by means of a wet process using the paste of titanium dioxide (TiO_2) prepared from commercial powders of TiO_2 nanopartilces, VP TiO_2 P90 and AEROXIDE® TiO_2 P25. The other ingredients of the TiO_2 pastes were ethanol, aqueous solution of acetic acid, α-terpineol, and ethyl cellulose. The optimum composition has been determined by comparing the energy conversion efficiencies of assembled DSSCs. The sensitizer dye is the Ruthenium 535-bisTBA in acetonitrile solution. The conversion efficiency of 9% or higher has been obtained by using a double-layer film of P90-type TiO_2 with an immersion of FTO glass into a $TiCl_4$ solution and an additional coating of a light scattering layer.

5. Fabrication, Analysis and Evaluation of Dye-Sensitized Solar Cells Made from Zinc Oxide Nanorods

Production of zinc oxide nanostructures in solution phase have attracted wide attentions and triggered various research works aiming at low cost and large scale electrode materials for DSSCs. We have studied the growth of ZnO nanorod array on fluorine-doped tin oxide substrates using a low-temperature solution method. By optimizing the growth parameters, such as reagent concentrations and temperatures (typ. 90 °C), we can control the hydrothermal growth and obtain a maximum length of 18 μm with an aspect ratio of 136. The ZnO nanorods were then applied to the electrode materials of the solar cells. The DSSCs with ZnO nanorods have produced the best energy conversion efficiency η of 1.63%. The effects of the difference in aspect ratio and device process on η have been discussed.

6. Theoretical Investigations on the Adsorption Geometries and Electronic Structures of Azo Dyes Adsorbed on TiO_2

We have employed periodic density functional theory calculations to study the adsorption geometries and electronic structures of azo dyes anchored on TiO_2 surfaces. The theoretical adsorption energies indicate that the bidentate bridging configuration is more preferable than the bidentate chelating and monodentate ester-type geometries. The band gap energies are smaller for the adsorbed complexes than for the clean surfaces, since additional electronic states arise from mixing of the molecular orbitals of the dyes with the TiO_2 valence and conduction bands. The strong electronic coupling between the excited states of azo dyes and conduction bands is observed in the high-efficiency dyes, but not in the low-efficiency dyes. Moreover, the Fermi levels of TiO_2 covered with the former dyes are shifted to higher direction than those with the latter. Thus, the open circuit voltage was increased in DSSCs based on the former dyes.

References

1) H. Katayanagi and K. Mitsuke, *J. Chem. Phys.* **135**, 144307 (8 pages) (2011).
2) H. Katayanagi and K. Mitsuke, *J. Chem. Phys. (Communication)* **133**, 081101 (4 pages) (2010).
3) K. Nakajima, K. Ohta, H. Katayanagi and K. Mitsuke, *Chem. Phys. Lett.* **510**, 228–233 (2011).
4) K. Mitsuke, D. Bashyal and K. Nakajima, *Proc. PACCON* **2011**, 457–460 (2011).

Light Source Developments by Using Relativistic Electron Beams

UVSOR Facility
Division of Advanced Accelerator Research

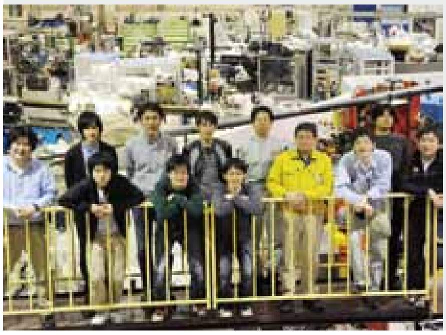

KATOH, Masahiro	Professor
ADACHI, Masahiro	Assistant Professor
ZEN, Heishun	Assistant Professor
TANIKAWA, Takanori	Graduate Student
TAIRA, Yoshitaka	Graduate Student*
KIKUCHI, Yoshitaka	Graduate Student*
GOTO, Yoshiaki	Graduate Student*
WASA, Naoki	Graduate Student*

This project involves researches and developments on synchrotron light source, free electron laser, beam physics and their related technologies. Most of these works are performed at the UVSOR Facility.

1. Developments on UVSOR Accelerators

In these years, we have been preparing for a new injection method called top-up injection at the UVSOR-II electron storage ring.1) In this operation scheme, electron beam is re-filled with a short interval, typically one minute, to keep the beam current approximately constant. It was expected that synchrotron radiation experiments under more stable condition would be possible. In July 2010, we have started operating UVSOR-II with the top-up injection fully in the users beam time, which is usually 12 hours a day. The stability of the injection efficiency is essentially important for the stable top-up operation. However, some drifts of the pulse power supplies for the injector and the beam transport system in various time scales, minutes to hours, made the injection efficiency unstable. We have developed a feedback system based on digital oscilloscopes and PC's, and have succeeded to stabilize them.2)

In spring 2010, we have installed a new undulator at a straight section created last year by moving the injection point to another short straight section, as shown in Figure 1. The undulator is APPLE-II type and will be used as a modulator in the coherent synchrotron radiation experiments as described later. Another undulator, which will work as a radiator producing coherent harmonic radiation, will be installed in this autumn.

Figure 1. New APPLE-II type undulator just after the installation in spring, 2011. Another undulator will be installed in autumn 2011. Both of them will be used to produce coherent synchrotron radiation.

We have designed a new magnetic lattice for the storage ring, in which the emittance could be reduced by factor of about 2. An upgrade program has been funded based on this design. Eight bending magnets, which have been used for more than 25 years, would be replaced with combined-function ones. The design and construction of new magnets are in progress. A pulse sextupole magnet system was designed and is under construction, which will be used to realize more sophisticated beam injection scheme, in which the electron beam movement during the injection would be reduced significantly not to disturb users experiments. A new 1m long in-vacuum undulator has been designed and is under construction, which will be installed at the last straight section reserved for insertion devices. This upgrade would make UVSOR-II the world brightest low energy synchrotron light source. The reconstruction work would be completed in summer, 2012.

2. Light Source Developments

We have demonstrated that coherent synchrotron radiation of various properties could be generated in an electron storage ring by using an external laser source.3–5) This research is supported by the Quantum Beam Technology Program of JST/MEXT. Under this support, a new experimental station is being constructed.6) A new undulator was installed. The upgrade of the laser system was completed. Two new beamlines dedicated to the coherent lights in the VUV range and in the THz range is under construction.7) The experiments in the new site will be started this winter.

Coherent harmonic generation is a method to produce coherent harmonics of laser light by using relativistic electron beam. We have succeeded in producing the coherent harmonics of Ti:Sa laser in the VUV range, up to 9th harmonic.[8)] We observed saturation of the coherent radiation intensity as increasing the laser power. After the saturation, the intensity of the coherent harmonics oscillates with the laser intensity. We have explained this phenomenon as the result of the micro-bunch formation in the over-bunching regime.[9)]

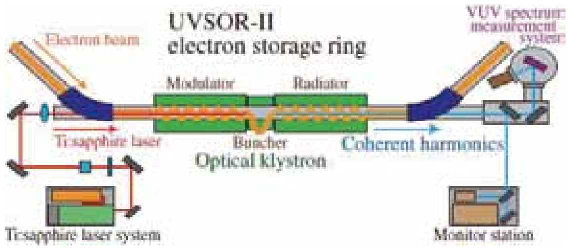

Figure 2. Experimental set-up of Coherent Harmonic Generation at UVSOR-II.

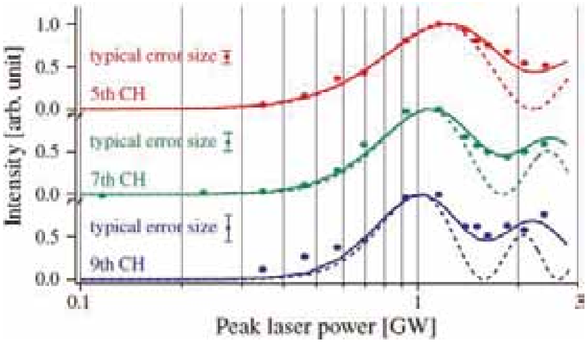

Figure 3. Coherent Harmonic Radiation Intensity vs. Injected Laser Power.

Laser Compton scattering is a technique to produce a quasi-monochromatic X-rays and gamma-rays by using a relativistic electron beam and laser. The laser photons are Compton back-scattered by the high energy electrons and are converted to gamma-rays. The electron beam circulating in the storage ring is very thin in the vertical direction. The typical diameter is in the order of 10 microns. By injecting laser light from the vertical direction to the beam, it is possible to produce ultra-short, quasi-monochromatic, energy tunable, polarization variable gamma-ray pulses. We have already confirmed the tunability of the energy and the polarization.[10)] Techniques to measure the pulse width is under development.

3. Developments of Accelerator Technologies

We have observed that operation of the undulators at UVSOR-II affects the beam lifetime and the injection efficiency and sometimes causes problems on the top-up operation. We consider that this is due to the non-linear magnetic field produced by the undulators. To reduce these effects, we are developing multi-wire correction coil system. The coil consists of tens of thin wires on the beam duct at the undulator and produces various correction fields depending on the electric current of each wire. Based on the preliminary experiment last year, we have fabricated a coil with 14 flat wires, in collaboration with Equipment Development Center. It was confirmed that the coil could correct the non-linear field produced by the undulators.[11)]

References

1) M. Katoh, M. Adachi, H. Zen, J. Yamazaki, K. Hayashi, A. Mochihashi, M. Shimada and M. Hosaka, *AIP Conf. Proc.* **1234**, 531 (2010).
2) H. Zen, M. Adachi, M. Katoh, K. Hayashi, J. Yamazaki, T. Tanikawa, Y. Taira, M. Hosaka and N. Yamamoto, *Proc. 1st Int. Particle Accel. Conf.* 2576–2578 (2010).
3) (in alphabetic order) S. Bielawski, C. Evain, T. Hara, M. Hosaka, M. Katoh, S. Kimura, A. Mochihashi, M. Shimada, C. Szwaj, T. Takahashi and Y. Takashima, *Nat. Phys.* **4**, 390–393 (2008).
4) M. Labat, M. Hosaka, M. Shimada, M. Katoh and M. E. Couprie, *Phys. Rev. Lett.* **101**, 164803 (2008).
5) M. Shimada, M. Katoh, M. Adachi, T. Tanikawa, S. Kimura, M. Hosaka, N. Yamamoto, Y. Takashima and T. Takahashi, *Phys. Rev. Lett.* **103**, 144802 (2009).
6) M. Adachi, M. Katoh, H. Zen, T. Tanikawa, M. Hosaka, Y. Takashima, N. Yamamoto and Y. Taira, *AIP Conf. Proc.* **1234**, 492 (2010).
7) S. Kimura, E. Nakamura, M. Hosaka, T. Takahashi and M. Katoh, *AIP Conf. Proc.* **1234**, 63 (2010).
8) T. Tanikawa, M. Adachi, M. Katoh, J. Yamazaki, H. Zen, M. Hosaka, Y. Taira and N. Yamamoto, *Proc.1st Int. Particle Acc. Conf.* 2206–2208 (2010).
9) T. Tanikawa, M. Adachi, H. Zen, M. Hosaka, N. Yamamoto, Y. Taira and M. Katoh, *Appl. Phys. Express* **3**, 122702 (3 pages) (2010).
10) Y. Taira, M. Adachi, H. Zen, T. Tanikawa, M. Hosaka, Y. Takashima, N. Yamamoto, K. Soda and M. Katoh, *Nucl. Instrum. Methods Phys. Res., Sect. A* **637**, 5116–5119 (2011).
11) Y. Kikuchi, M. Hosaka, N. Yamamoto, Y. Takashima, M. Adachi, H. Zen and M. Katoh, *UVSOR Activity Report* **2010**, 31 (2011).

---

* carrying out graduate research on Cooperative Education Program of IMS with Nagoya University

Synchrotron Radiation Spectroscopy on Strongly Correlated Electron Systems

UVSOR Facility
Division of Advanced Solid State Physics

KIMURA, Shin-ichi	Associate Professor
MATSUNAMI, Masaharu	Assistant Professor
MIYAZAKI, Hidetoshi	IMS Fellow*
MORI, Tatsuya	Post-Doctoral Fellow†
IMURA, Keiichiro	Post-Doctoral Fellow
OZKENDIR, Osman Murat	Research Fellow‡
NISHI, Tatsuhiko	Research Fellow§
IIZUKA, Takuya	Graduate Student
HAJIRI, Tetsuya	Graduate Student‖
NIWA, Ryosuke	Graduate Student‖

Solids with strong electron–electron interaction, namely strongly correlated electron systems (SCES), have various physical properties, such as non-BCS superconducting, colossal magneto-resistance, heavy fermion and so on, which cannot be predicted by first-principle band structure calculation. Due to the physical properties, the materials are the candidates of the next generation functional materials. We investigate the mechanism of the physical properties as well as the electronic structure of SCES, especially rare-earth compounds, organic superconductors and transition-metal compounds, by infrared/THz spectroscopy and angle-resolved photoemission spectroscopy based on synchrotron radiation. Since experimental techniques using synchrotron radiation are evolved rapidly, the development of the synchrotron radiation instruments is also one of our research subjects.

1. Electronic-Structure-Driven Magnetic Ordering in a Kondo Semiconductor $CeOs_2Al_{10}$[1,2)]

Cerium-based compounds CeM_2Al_{10} (M = Ru, Os) are new-type of Kondo semiconductors/insulators because they show antiferromagnetic transition at higher temperature than that expected by the Ruderman-Kittel-Kasuya-Yoshida (RKKY) interaction. We reported the anisotropic changes in the electronic structure of a Kondo semiconductor $CeOs_2Al_{10}$ across an anomalous antiferromagnetic ordering temperature (T_0) of 29 K, using optical conductivity spectra as shown in Figsures 1 (a)-(c). The spectra along the *a* and *c* axes indicate that an energy gap due to the hybridization between conduction bands and nearly local 4f states, namely the c–f hybridization gap, emerges from a higher temperature continuously across T_0. Along the *b* axis, on the other hand, another energy gap with a peak at 20 meV becomes visible at 39 K (> T_0) and fully opens at T_0 (Figure 1d) because of a charge instability. This result implies that the appearance of the energy gap, as well as the change in the electronic structure along the *b* axis, induces the antiferromagnetic ordering below T_0.

In the reference material $CeFe_2Al_{10}$, which does not have the anomalous antiferromagnetic ordering, the temperature

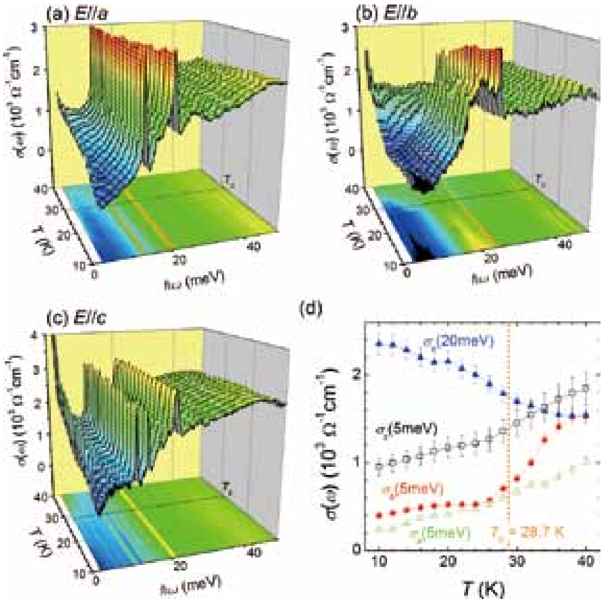

Figure 1. Temperature-dependent optical conductivity [σ(ω)] spectra in E // a (a), E // b (b), and E // c (c) at temperatures from 10 to 40 K. (d) Temperature dependence of representatives of spectral change. σ_x(5 meV) [x = a, b, c (x is axis name)] and σ_b(20 meV) are the intensities of the σ(ω) spectra at 5 and 20 meV, respectively.

dependence of the polarized optical conductivity [σ(ω)] spectra were also reported. The σ(ω) spectrum along the *b*-axis differs greatly from that in the *ac*-plane, indicating that this material has an anisotropic electronic structure. At low temperatures, in all axes, a shoulder structure due to the optical transition across the hybridization gap between the conduction band and the localized 4f states, namely c–f hybridization, appears at 55 meV. However, the gap opening temperature and the temperature of appearance of the quasiparticle Drude weight are strongly anisotropic indicating the anisotropic Kondo effect. The strong anisotropic nature in both electronic structure and Kondo effect is considered to be relevant to the anomalous magnetic phase transition in $CeRu_2Al_{10}$ and $CeOs_2Al_{10}$.

2. Nodeless Superconducting Gap in $A_xFe_2Se_2$ (A = K, Cs) Revealed by Angle-Resolved Photoemission Spectroscopy[3)]

Pairing symmetry is a fundamental property that characterizes a superconductor. For the iron-based high-temperature superconductors, an $s_\pm$-wave pairing symmetry has received increasing experimental and theoretical support. More specifically, the superconducting order parameter is an isotropic s-wave type around a particular Fermi surface, but it has opposite signs between the hole Fermi surfaces at the zone center and the electron Fermi surfaces at the zone corners. Here we report the low-energy electronic structure of the newly discovered superconductors, $A_xFe_2Se_2$ (A = K, Cs) with a superconducting transition temperature (T_c) of about 30 K. We found $A_xFe_2Se_2$ (A = K, Cs) is the most heavily electron-doped among all iron-based superconductors. Large electron Fermi surfaces are observed around the zone corners as shown in Figure 2, with an almost isotropic superconducting gap of ~10.3 meV, whereas there is no hole Fermi surface near the zone center, which demonstrates that interband scattering or Fermi surface nesting is not a necessary ingredient for the unconventional superconductivity in iron-based superconductors. Thus, the sign change in the $s_\pm$ pairing symmetry driven by the interband scattering as suggested in many weak coupling theories becomes conceptually irrelevant in describing the superconducting state here. A more conventional s-wave pairing is probably a better description.

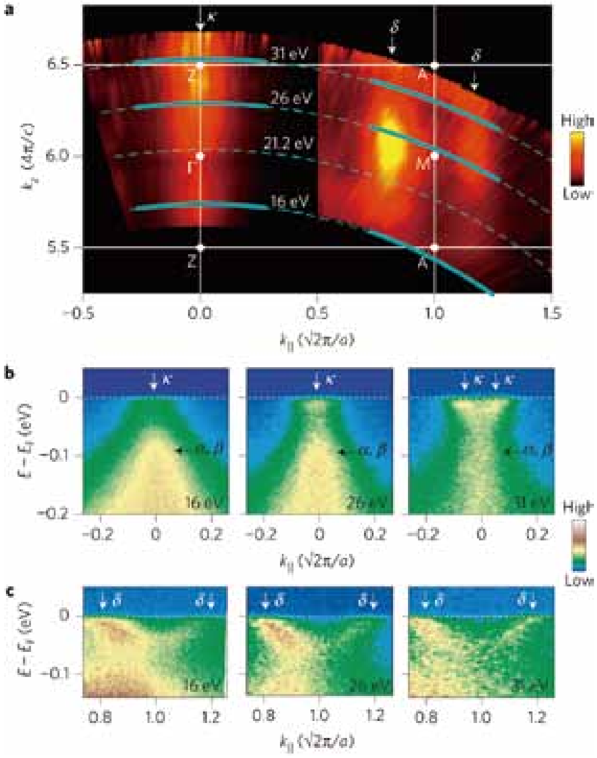

Figure 2. The photoemission intensity of $K_{0.8}Fe_2Se_2$ in the ΓZAM plane. The intensity was integrated over a window of (E_F–15 meV, E_F+15 meV). Different k_z's were accessed by varying the photon energy at Beamline 7U of UVSOR, as indicated by the dashed lines, where an inner potential of 11 eV is used to obtain k_z. **b**, **c**, Photoemission intensity along the three momentum cuts across Γ–Z, and the other three momentum cuts across M–A respectively as marked by thick solid lines in **a**. The data were taken with horizontally polarized 16, 26 and 31 eV photons.

References

1) S. Kimura, T. Iizuka, H. Miyazaki, A. Irizawa, Y. Muro and T. Takabatake, *Phys. Rev. Lett.* **106**, 056404 (2011).
2) S. Kimura, Y. Muro and T. Takabatake, *J. Phys. Soc. Jpn.* **80**, 033702 (2011).
3) Y. Zhang, L. X. Yang, M. Xu, Z. R. Ye, F. Chen, C. He, H. C. Xu, J. Jiang, B. P. Xie, J. J. Ying, X. F. Wang, X. H. Chen, Jiangping Hu, M. Matsunami, S. Kimura and D. L. Feng, *Nat. Mater.* **10**, 273 (2011).

---

* Present Address; Center for Fostering Young and Innovative Researchers, Nagoya Institute of Technology

† Present Address; Graduate School of Pure and Applied Sciences, University of Tsukuba

‡ from Mersin University, Turkey

§ from Chiba University

|| carrying out graduate research on Cooperative Education Program of IMS with Nagoya University

Electronic Structure and Decay Dynamics in Atoms and Molecules Following Core Hole Creation

UVSOR Facility
Division of Advanced Photochemistry

SHIGEMASA, Eiji	Associate Professor
IWAYAMA, Hiroshi	Assistant Professor
ISHIKAWA, Lisa	Post-Doctoral Fellow

The dynamics of the inner-shell photoexcitation, photoionization, and subsequent decay processes is much more complex, in comparison to outer-shell photo-processes. For instance, the inner-shell photoionization is concomitant with the excitation and ionization of valence electrons, which reveal themselves as shake-up and shake-off satellite structures in the corresponding photoelectron spectrum. The one-photon multi-electron processes, which are entirely due to the electron correlation in the system, are known to happen not only in the primary inner-shell hole creation processes, but also in their relaxation processes. Our research project is focused on elucidating the electronic structures and decay dynamics in core-excited atoms and molecules, by utilizing various spectroscopic techniques together with monochromatized synchrotron radiation in the soft x-ray region.

1. Doppler Effect in Fragment Autoionization Following Core-to-Valence Excitations

The Doppler effect is known to occur when the source and observer are in motion relative to each other, leading to an apparent change in the observed frequency of the propagating wave. This effect has a wide variety of applications in many fields, relating to the sensing of movement. In the research field of molecular science, the sensing of nuclear motion has long been an attractive issue. Gel'mukhanov and co-workers predicted in 1998[1)] that the nuclear motion in 'ultrafast dissociation' following molecular core-level photoexcitation can be probed by the Doppler effect in emitted Auger electron. Ultrafast dissociation is a process where the molecular dissociation at the core-excited state precedes the Auger decay and then an atomic fragment emits an Auger electron. This atomic Auger electron can possess the opposite Doppler shift depending on the direction approaching the detector (label (A) in Figure 1(a)) or moving away from it (label (B) in Figure 1(a)). This electron Doppler shift in kinetic energy can be expressed as $\mathbf{p}\cdot\mathbf{v}$, where $\mathbf{p}$ is the momentum of the electron and $\mathbf{v}$ is the velocity vector of the emitting fragment, and thus it becomes maximum when both vectors are parallel. Although molecules in the gas phase are randomly oriented, molecular photoabsorption is known to be highly anisotropic relative to the polarization vector of the incident radiation. Therefore, detection of the emitted Auger electron along the preferred direction of emission of the fragment makes the measurement of the Doppler shift possible experimentally.

In our recent works,[2)] it has been disclosed that the Doppler effect can be utilized as a unique tool to investigate the molecular dynamics at singly-charged ion states produced by resonant Auger decay. Special attention is paid to detecting slow electrons. In cascade Auger decay, two electrons are ejected sequentially with distinct kinetic energies depending on the energy levels of the initial, intermediate, and final electronic states involved. One of the two emitted electrons is often slow (typically less than 5 eV). Singly-charged molecular ion states populated by the first electron emission can undergo competition between second electron emission and molecular dissociation. If one of the dissociating fragments is excited it may subsequently autoionize; the autoionizing atomic fragment can act as an electron emitter which can exhibit a Doppler splitting if the kinetic energy of the atomic fragment is sufficiently large and the initial photoabsorption anisotropy is substantially maintained in the angular distribution of fragments.

As an example, the O* autoionizing electron spectrum following the O1s → σ^* excitation in O_2 is denoted in Figure 1(b). Clear Doppler profiles, depending on the fragment-ion directions as labeled in (A) or (B), are discernable in the atomic oxygen autoionization peaks. The corresponding Doppler profiles, as a counterpart of the fragmentation process, are also seen in the atomic Auger electron peak. It is clarified that femtosecond dissociation dynamics of singly-charged ion states produced by resonant Auger decay can be deduced from the information obtained by analyzing the Doppler profiles. In the cascade Auger decay following the O1s → σ* excitation in O_2, it is concluded that the slow Auger electrons are produced by autoionization of valence-excited atomic fragments created simultaneously to the core-excited atomic fragments during ultrafast dissociation of the oxygen molecule.

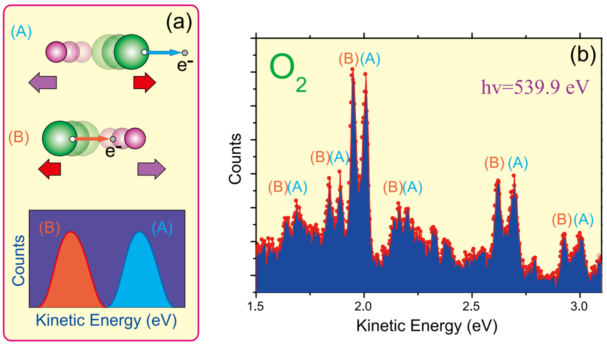

Figure 1. (a) Schematic representations for explaining a source of the electron Doppler splittings in kinetic energy, and (b) Doppler splittings observed in the autoionizing electron spectrum from an atomic oxygen following the O1s → σ* excitation in O_2.

2. Two-Dimensional Electron Spectroscopy on BL6U

A new project for constructing the undulator beamline BL6U has been initiated since 2007. A Monk-Gillieson mounting with a variable-included-angle mechanism has been chosen, in order to cover a wide photon energy region (30–500 eV) with one single grating. It has been confirmed through its performance tests that the monochromator designed can cover the photon energy ranging from 40 to 400 eV with the resolving power higher than 5000 and the photon flux more than 10^{11} photons/sec, when the storage ring is operated in the top-up mode.

A new electron spectrometer, MBS-A1, for gas phase spectroscopy has successfully been installed, in parallel with the construction program of BL6U. High-resolution electron spectroscopy is a powerful method to study electronic structures of atoms and molecules, especially when high-resolution electron spectra and their polarization dependences are measured as a function of photon energy. The ability of this two dimensional (2D) electron spectroscopy has been proved in our recent work at SPring-8.[2,4] In order to apply high-resolution 2D electron spectroscopy to the investigation of the L-shell excitations of the second row elements, a new experimental setup for BL6U has been designed and constructed.

For realizing 2D electron spectroscopy with high resolution, software development for controlling both the beamline monochromator and MBS-A1 analyzer has been performed. For the beamline monochromator, not only its output but the gap of the undulator should be controlled. After careful optimizations for the undulator gaps, 2D electron spectroscopy on BL6U has become feasible, thanks to the stable operation of the UVSOR-II storage ring.

Figure 2 demonstrates the 2D maps for the de-excitation spectra following the double excitations near the carbon 1s photoionization threshold in CO, measured in (a) horizontal, and (b) vertical directions, respectively, as an example of successful measurements. The exit slit opening of the monochromator was set at 30 μm, which corresponds to the photon energy resolution of about 60 meV. The pass energy and slit width of the MBS-A1 analyzer were set to 100 eV and 0.2 mm, which results in the electron energy resolution of about 60 meV. The straight lines with a slope of 1 in the high kinetic energy (KE) region in each 2D map are due to the valence photoelectrons with vibrational structures. The vertical lines around KE of 275 eV in Figure 2(b) are assigned to the atomic Auger line from oxygen atoms after the dissociation of CO molecules. Some island-like structures are seen in the KE range of 267–270 eV in Figure 2(a) and Figure 2(b), which seem to be specific to the decay processes of the double excitations. The complicated photon energy dependences of the structures may suggest that the de-excitation processes of the doubly excited states of CO are not so simple.

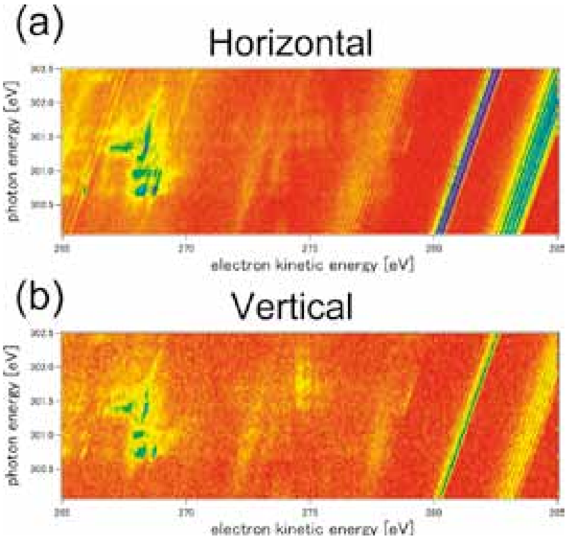

Figure 2. 2D map of de-excitation spectra following the double excitations around the carbon K-edge of CO, measured in (a) horizontal, and (b) vertical directions, respectively.

References

1) F. Gel'mukhanov, H. Ågren and P. Sałek, *Phys. Rev. A* **57**, 2511–2526 (1998).
2) E. Shigemasa *et al.*, *New J. Phys.* **12**, 063030 (9 pages) (2010).
3) R. Guillemin *et al.*, *Phys. Rev. A* **82**, 051401(R) (4 pages) (2010).
4) T. Kaneyasu *et al.*, *Phys. Rev. Lett.* **101**, 183003 (4 pages) (2008).

Micro Solid-State Photonics

Laser Research Center for Molecular Science
Division of Advanced Laser Development

TAIRA, Takunori	Associate Professor
LOISEAU, Pascal	Visiting Associate Professor
ISHIZUKI, Hideki	Assistant Professor
AKIYAMA, Jun	IMS Research Assistant Professor
TSUNEKANE, Masaki	Post-Doctoral Fellow
SATO, Yoichi	Post-Doctoral Fellow
JOLY, Simon	Post-Doctoral Fellow
BHANDARI, Rakesh	Post-Doctoral Fellow
KONG, Weipeng	Graduate Student
ITO, Yuta	Graduate Student*
ONO, Yoko	Secretary
INAGAKI, Yayoi	Secretary

The artistic optical devices should be compact, reliable, efficient and high power light sources. With the approaches of domain structures and boundaries engineering, it is possible to bring the new interaction in their coherent radiation. The high-brightness nature of Yb or Nd doped single crystal or ceramic microchip lasers can realize efficient nonlinear wavelength conversion. In addition, designed nonlinear polarization under coherent length level allows us new function, such as the quasi phase matching (QPM). The development of "***Micro Solid-State Photonics***," which is based on the micro domain structure and boundary controlled materials, opens new horizon in the laser science.

1. Composite, All-Ceramics, High-Peak Power Nd:YAG/Cr^{4+}:YAG Monolithic Micro-Laser with Three-Beam Output for Engine Ignition

A passively Q-switched Nd:YAG/Cr^{4+}:YAG micro-laser with three-beam output was realized for multi-point ignition of an automobile engine as shown in Figure 1. A single active laser source made of a composite, all-ceramics Nd:YAG/Cr^{4+}:YAG monolithic cavity with a length of 10 mm was pumped by three independent lines. At 5 Hz repetition rate, each line delivered laser pulses with energy of 2.4 mJ and 850-ps pulse duration (2.8-MW peak power). The M^2 factor of a laser beam was 3.7, and stable air breakdowns were realized. The increase of pump repetition rate up to 100 Hz improved the laser pulse energy by 3% and required an increase of the pump pulse energy by only 5%. We confirmed that pulse timing of the laser-array beams could by adjusted by less than 5% tuning of an individual line pump energy, and then simultaneous multi-point ignition is possible.

Figure 1. Microchip laser with three-beam output.

2. Development of Megawatt-Peak-Power UV Microchip Laser

Megawatt peak power, giant pulse microchip lasers are attractive for wavelength conversion, provided their output is linearly polarized. We use a [110] cut Cr^{4+}:YAG for passively Q-switched Nd:YAG microchip laser to obtain a stable, linearly polarized output. Then, we optimize the conditions for second harmonic generation (SHG) using Lithium Triborate (LBO) to achieve > 6 MW peak power, 1.7 mJ, 265 ps, 100 Hz pulses at 532 nm wavelength with a conversion efficiency of 84.71%. Further, using β-Barium Borate (BBO) for fourth harmonic generation (FHG), we obtain > 2 MW peak power, 562 μJ, 260 ps, 100 Hz pulses at 266nm with 51.2% conversion efficiency as shown in Figure 2. These are world records for SHG and FHG using microchip lasers.

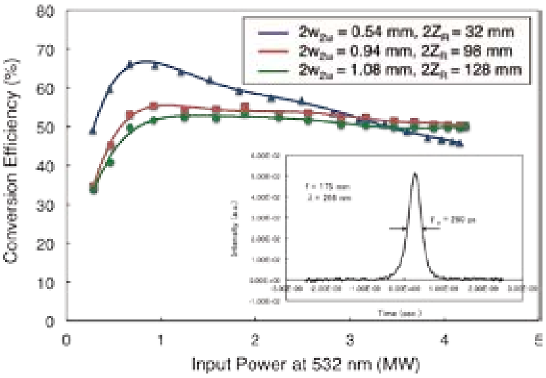

Figure 2. FHG conversion characteristics under different focusing conditions.

3. Variation of the Stimulated Emission Cross Section in Nd:YAG Caused by the Structural Changes of Russell-Saunders Manifolds

It was experimentally found that electronic structures of Russell-Saunders manifolds in Nd:YAG depended on the Nd^{3+}-doping concentration (C_{Nd}) and its fabrication process. Both of the bandwidth and the branching ratio in fluorescent transitions in Nd:YAG varied almost linearly depending on C_{Nd}, and a fabrication process has its own diluted limit of the bandwidth and the branching ratio. Also dependences of Stark splitting in Nd:YAG were also observed. As a result, Nd^{3+}-doping causes 1.9% and 4.5% reduction in the maximum value of the stimulated emission cross section (σ) of Nd:YAG per 1 at.% of C_{Nd} at 1.064 µm and 1.319 µm, respectively. Figure 3 shows the concentration dependence of σ in Nd:YAG at 1.064-µm (a) and 1.319-µm (b).

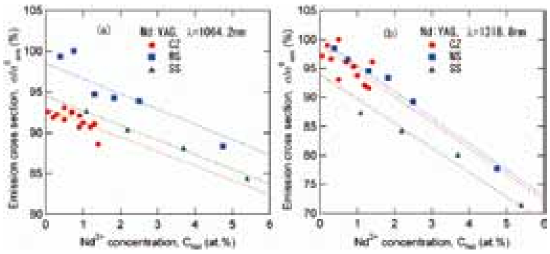

Figure 3. The ratio between σ to the Nd^{3+}-diluted limit ($\sigma_{em}{}^0$) of Nd:YAG at 1.064-µm (a) and 1.319-µm (b). Circle, triangle, and square indicate $\sigma/\sigma_{em}{}^0$ of CZ, SS, and WS, respectively.

4. Demonstration of Rare-Earth-Doped Anisotropic Ceramic Laser

We succeeded in developing a QCW-diode-pumped "anisotropic ceramic laser" by using micro-domain-controlled neodymium doped hexagonal fluorapatite [Nd_3:$Ca_{10}(PO_4)_6F_2$, Nd:FAP] polycrystalline ceramics as the gain medium, which were fabricated by the rare earth assisted magnetic grain-orientation control method, as a step toward achieving giant micro photonics. The laser delivers 1063.10 and 1063.22 nm output beams when pumped with a central wavelength of 807.5 nm and a 2 nm bandwidth diode laser operating in quasi-continuous-wave (QCW) mode. The resulting slope efficiency with respect to the absorbed power was 2.6% and the oscillation threshold was 12 W when uncoated 2 at.% Nd:FAP material was used as Figure 4.

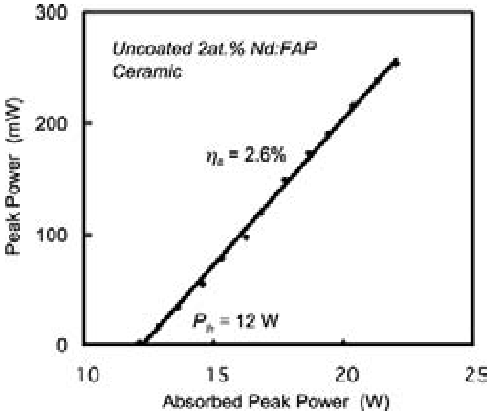

Figure 4. Nd:FAP QCW peak laser output power at 1.06 µm *versus* pump power at 807.5 nm. The pump pulse duration and repetition rate are 420 µs and 6 Hz.

5. PFabrication of Slant Quasi-Phase Matching Structure in Mg-Doped Congruent $LiNbO_3$

We fabricated slant quasi-phase-matching structure in 2-mm-thick Mg-doped $LiNbO_3$ crystal at 65° slant angle with 75-µm surface period as Figure 5. Slant QPM has a possibility of wafer-scale-aperture device, suitable for handling high power/energy lasers.

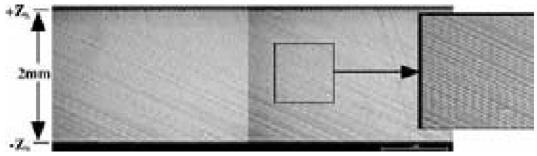

Figure 5. Y-face photograph of obtained slant QPM structure in 65° slant MgLN with thickness d_1 = 2 mm. Surface QPM period Λ_1 = 75 µm.

References

1) N. Pavel, M. Tsunekane and T. Taira, *Opt. Express* **19**, 9378–9384 (2011).
2) R. Bhandari and T. Taira, T*echnical Digest of Nonlinear Optics 2011 (NLO2011)*, NME2, Kauai, Hawaii, USA (July 17–22, 2011).
3) Y. Sato and T. Taira, *Opt. Mater. Express* **1**, 514 (2011).
4) J. Akiyama, Y. Sato and T. Taira, *Appl. Phys. Express* **4**, 022703 (2011).
5) H. Ishizuki and T. Taira, *Technical Digest of Nonlinear Optics (NLO2011)*, NMA4, Kauai, Hawaii, USA (July, 17–22, 2011).

---

* carrying out graduate research on Cooperative Education Program of IMS with Ibaraki University.

Ultrafast Laser Science

Laser Research Center for Molecular Science
Division of Advanced Laser Development

FUJI, Takao	Associate Professor
NOMURA, Yutaka	Assistant Professor
MASUDA, Michiko	Secretary
KAWAI, Shigeko	Secretary

Speed of ultrafast energy transfer from light to molecules (*i.e.* primary processes of photosynthesis, photoisomerization in visual pigments, *etc.*) is on the order of femtosecond (10^{-15} s). In our laboratory, we develop cutting edge lasers for such ultrafast molecular science, namely, femtosecond or attosecond (10^{-18} s) ultrashort pulse lasers.

For example, arbitrary waveform synthesis can be performed with simultaneous generation of femtosecond light pulses in various wavelength regions and superimposition of them with precisely controlled phases.

We would like to develop such advanced light control technology, which can push forward the research on ultrafast photochemical reactions.

1. Ultrabroadband Mid-Infared Source Based on Four-Wave Rectification[1)]

Optical rectification is one of the most commonly used frequency conversion processes for generation of ultrashort teraherz wave. The nonlinear process basically produces a wave whose shape is proportional to a derivative of temporal intensity profile of an input pulse.

Nowadays 7-fs Ti:Sapphire oscillators are commercially available, thus by using such a light source it is even possible to generate broadband mid-infrared light through the optical rectification assuming perfect phase matching condition. Comparing with a traditional mid-infrared ultrashort pulse generation with sequential down conversion processes, the most unique feature of the scheme is that carrier-envelope phase of the generated mid-infrared pulses is passively stabilized.

Several groups demonstrated such broadband and phase-stable light generation with solid nonlinear crystals. However, it is not realistic to have broadband spectrum which covers the entire mid-infrared (3–20 μm) region by using nonlinear solid crystals because of the limited transmission bandwidth.

On the other hand, optical rectification with gas media is an interesting alternative technique since transmission bandwidth of gases is much wider than that of solid media. In fact, rare gases are completely transparent from teraherz to visible region. Although the largest drawback of gas media is low nonlinear coefficient, it is possible to use much more intense pumping pulse than that for solid media, and filamentation effect of ultrashort pump pulses can enhance the efficiency of the frequency conversion.

Ultrabroadband mid-infrared pulse generation through the optical rectification (four-wave rectification) in gases was firstly demonstrated in 2007,[2)] and the technique was followed by several groups. Such mid-infrared pulses with more than one octave at full width at half maximum are very attractive to be applied for molecular spectroscopy, *e.g.* two-dimensional infrared spectroscopy.

Here, latest progress of the mid-infrared pulse generation by four-wave rectification through filamentation in gases and the detailed characterization of the generated mid-infrared pulses are to be shown. In addition, we performed three-dimensional (3D) numerical simulation and compared the

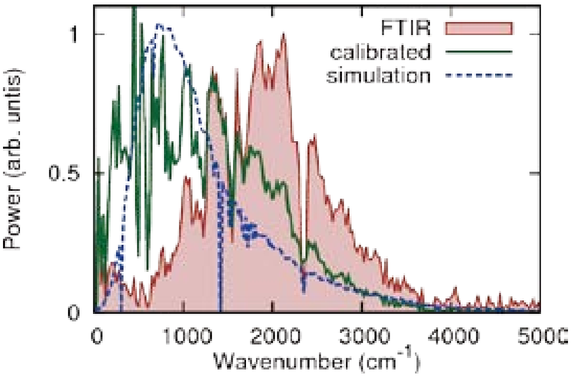

Figure 1. A typical spectrum of the mid-infrared pulse generated through the four-wave rectification process (filled curve, Brown). The spectrum was measured with a home-built Fourier transform infrared spectrometer. Sharp dips at 2400 cm^{-1} and at around 1800 cm^{-1} are due to absorption of carbon dioxide and water vapor in air, respectively. The solid line (Green) shows a spectrum after sensitivity calibration. The dotted line (Blue) shows a spectrum obtained from three-dimensional numerical simulation. The scale of the vertical axis is linear.

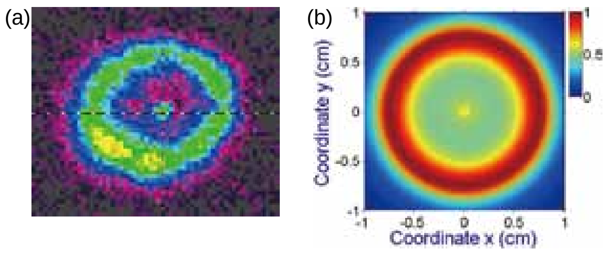

Figure 2. (a) Experimental and (b) simulated radical intensity distributions of the mid-infrared pulses.

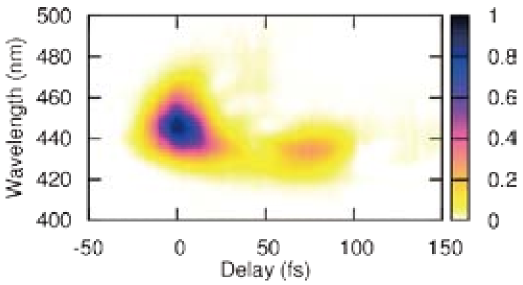

Figure 3. Measured XFROG trace.

experimental and theoretical results.

The light source was based on Ti:Sapphire multi-pass amplifier system (800 nm, 25 fs, 800 µJ@1 kHz). The second harmonic (ω_2, 90 µJ) and the fundamental (ω_1, 600 µJ) were spatially and temporally overlapped and focused into air by a concave mirror (r = –500 mm). A plasma column with a length of ~2 cm appeared around the focus. The mid-infrared pulse (ω_0) generated through four-wave rectification process ($\omega_1 + \omega_1 - \omega_2 \rightarrow \omega_0$) was filtered through Si and Ge plates and was introduced into a home-built fourier transform spectrometer. The Michelson-type interferometer consisted of a Ge coated KBr beam splitter, sliver mirrors, a feedback loop translation stage with 5 nm resolution, and a TGS (triglycine sulfate) pyroelectric detector.

The measured spectrum is shown as a filled curve (Brown) in the Figure 1. The broadband spectrum, which spread in whole mid-infrared region (500–4000 cm^{-1}), was generated due to broadband phase matching through the low dispersive gas medium. The power spectrum calibrated by using a SiC lamp (80007, Oriel) with known color temperature is also shown as a solid curve (Green) in Figure 1. Although the power in the frequency region lower than 500 cm^{-1} is not so reliable since the beam splitter in the Michelson-type interferometer was designed for > 500 cm^{-1}, it is very likely that the generated spectrum has significant intensity in the low frequency region. The pulse energy of the mid-infrared pulse was measured as ~250 nJ by using a pyroelectric detector (J-10MB-LE, Coherent). With this energy level, it is possible to apply the pulses for nonlinear spectroscopy for condensed matter. The pulse-to-pulse intensity fluctuation was about 2.5% rms. The transform-limited pulse calculated from the calibrated spectrum has less than 10 fs pulse duration, which is less than half the period of the center frequency (~1500 cm^{-1}). The passively stabilized carrier-envelope phase owing to the optical rectification scheme is highly valuable for the half-cycle pulses.

To explain the extremely broad spectrum, we performed a 3D modeling of nonlinear optical transformation of a high-intensity two-color field in air at atmospheric pressure. Our model is based on the slowly evolving wave approximation modified to include ionization of the gas by ultrashort laser pulses. The nonlinear polarization term includes not only the $\omega_1 + \omega_1 - \omega_2 \rightarrow \omega_0$ term, but all possible four-wave mixing terms, including those describing self- and cross-phase modulation and third-harmonic generation. Simulations were performed in parallel codes on the Lomonosov supercomputer facility at Moscow State University. The simulated spectrum is shown as a dashed curve (Blue) in Figure 1.

Characterization of the beam profile and the angular dispersion are important for further application of the light source. We have measured the beam profile of the infrared beam by using a pyroelectric camera (Pyrocam III, Spiricon). The measured beam profile is shown in Figure 2(a). The shape of the beam was ring, which seems to correspond to conical emission of the filament. Angle of the cone was estimated to be about 3 deg.

Figure 2(b) shows the simulated beam profile of the mid-infrared pulse obtained from the 3D simulation at the same time as the spectrum. The ring shape and the angle of the cone were well reproduced. Standard phase matching for the relevant four-wave mixing process does not explain the conical emission pattern. The pattern is accurately reproduced in our simulations only when the full ionization-assisted coupled dynamics of optical fields involved in the generation of mid-infrared ultrashort waveforms is included in the analysis. According to the simulation, the conical emission does not have significant angular dispersion, then it should be possible to compress the pulse down to single cycle.

To quantitatively evaluate the temporal shape of the generated infrared pulse, we measured cross-correlation frequency resolved optical gating (XFROG). A small portion of the fundamental (ω_1) 25 fs pulse was used as a reference pulse. The reference pulse and the infrared pulse (ω_0, test pulse) were focused into air with a off-axis parabolic mirror (f = 150 mm). Generated four-wave mixing spectra ($\omega_1 + \omega_1 - \omega_0 \rightarrow \omega_2$) were measured with a spectrometer (USB2000+, Ocean Optics) by scanning the delay time between the reference pulse and the infrared test pulse.

The measured XFROG trace is shown in Figure 3. The pulse width was estimated to be 15 fs, which is 1.1 cycles for 4.2 µm carrier wavelength, from a retrieved temporal profile of the test pulse (FROG error was ~0.4%). The result clearly indicates that the generated MIR spectrum is coherent.

References

1) T. Fuji and Y. Nomura, *20th International Laser Physics Workshop (LPHYS'11)*, 5.3.4 Sarajevo, July 11–15 (2011). (invited talk)

2) T. Fuji and T. Suzuki, *Opt. Lett.* **32**, 3330–3332 (2007).

Visiting Professors

Visiting Professor

KODAMA, Ryosuke *(from Osaka University)*

High Energy Density Sciences

Now it is relatively easy to realize high energy density states with high power lasers. The states would have a variety of attractive fields of sciences and technologies such as particle acceleration, laboratory astrophysics, and material science, nuclear science including medical applications and laser fusion, which is "High Energy Density Science: HEDS." One of the advantages of the HED states is its energy density, which is much higher than that of the solid state matter. He is now exploring high energy density sciences in methods of introducing a Plasma Photonics concept to control intense light and high energy charged particles with high energy density plasmas. Nonlinear interaction of intense light with vacuum or nonlinear optics in vacuum will be significantly enhanced with the focusing angle of the interaction laser light, which must be realized by applying the novel geometry with plasma photonic devices. As his other important topics, he is interested in creation of high pressure condensed matter such as metallic solid hydrogen with high power lasers. Freezing of a higher energy density state or metallic Si have been already realized, extending the new scheme to more number of materials to have novel materials in hand, which have never seen on the earth.

Visiting Professor

KONDOH, Hiroshi *(from Keio University)*

Surface Dynamic Processes Studied by Soft X-Ray Spectroscopy

We have been working on surface dynamic processes such as charge transfer from a molecule to a substrate and surface catalytic reactions using synchrotron-based soft x-ray spectroscopies. Recently we have studied the time scale of the charge transfer from organic molecules to metal substrates by means of the core-hole decay spectroscopy. For instance, the Coster-Kronig autoionization accompanying the S 2s–3p transition was used for estimation of the time constant for the charge transfer from a sulfur-containing molecule to a metal substrate at BL-6U in the UVSORII. The resultant time constant were found to be of the order of sub-femtosecond. Another research subject regarding the surface dynamic process is the understanding of surface catalytic process which proceeds under ambient pressure conditions. In particular, applying the soft x-ray absorption spectroscopy with the transmission mode to real-time observation of catalytic processes will allow us to understand the reaction mechanism under the practical working condition of the catalyst.

Visiting Associate Professor

UENO, Kosei *(from Hokkaido University)*

Near-Field Intensity Profile of Metallic Nanostructures Using Near-Field Optical Microscope

The global problems relevant to the environment and energy are attracting attention, so that it is considered that the construction of efficient light-energy conversion devices serves as an important subject of the scientific research. Thus far, the interaction between photons and molecules has not received much attention in photochemistry. However, the creation of a progressive methodology that allows an increase in the excitation probability is necessary. Namely, to create a low-carbon-emitting society by utilizing light energy, it is necessary to introduce the concept of "effective utilization of photons" to photochemistry. We develop photochemical reaction fields, in which make it possible to increase the interaction between photons and molecules. Metallic nanostructures showing localized surface plasmon resonance are a promising approach for the development of photochemical reaction fields. Therefore, we study the optical properties of the metallic nanostructures which are prepared with nanometric accuracy and elucidate its near-field intensity profile according to using a near-field optical microscope developed by Prof. Okamoto in IMS to investigate fundamental mechanisms of the concept of "effective utilization of photons" induced by metallic nanostructures.

Visiting Associate Professor

TAKAHASHI, Toshiharu *(from Kyoto University)*

Development of New Spectroscopic Methods Using THz Coherent Synchrotron Radiation

We are developing new spectroscopic techniques with coherent synchrotron radiation (CSR) in the THz-wave region. One is the technique of the scanning near-field transmission and reflection microscopy using broadband CSR, where the high spatial resolution below the diffraction limit is available. Second, the method of the monochromatic THz-wave pump–photoemission probe spectroscopy (PES) is also developing. Since the VUV radiation by the coherent harmonic generation (CHG) can be emitted using the laser pulse in UVSOR, the jitter-free pump-probe spectroscopy is possible with the THz-CSR. In order to perform these spectroscopic techniques, we are constructing a new CSR beamline (BL1B) in UVSOR.

RESEARCH ACTIVITIES

Materials Molecular Science

Extensive developments of new molecules, molecular systems and their higher-order assemblies are being conducted in three Divisions of Electronic Structures, Electronic Properties, and Molecular Functions, one division for visiting professors, and Research Center for Molecular Scale Nanoscience, in an attempt to discover new phenomena and useful functions. The physical properties of electronic, optical and magnetic properties on new functional materials are investigated, and moreover, the chemical properties like catalysis and photochemistry and technological applications like solar cells are also examined in this department.

Graphene-Walled Alveolate Carbon & Structures and Functions of Metal–Carbon Nano-Systems Made from Metal-Acetylides

Department of Materials Molecular Science
Division of Electronic Structure

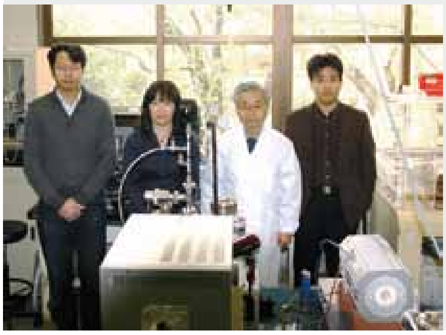

NISHI, Nobuyuki	Professor*
JUDAI, Ken	Assistant Professor†
NISHIJO, Junichi	Assistant Professor
USUI, Chika	Technical Fellow & Secretary

Metal acetylides or metal ethynyl molecules are made of the M^+–C^- ionic bonds. However, the ionic states of the acetylides are essentially metastable resulting in the segregation into metal-carbon or metal-organic polymer nanophases. Following to the invention of graphene-singlewalled Mesoporous Carbon Nano Dendrides (MCND) by evaporating silver from dendroid silver acetylide crystals, we have invented Graphene-multiwalled Alveolate Carbon (GAC), this time, and also 3D nanonets with GAC. These highly electron-conductive materials can be used for the electrodes of various next generation batteries.

1. Improvement of Graphene-Multiwalled Alveolate Carbon for Novel Battery Electrodes

As demonstrated by many researchers, graphene single sheets and multiple layers are successfully prepared on the ultraclean surface of metallic copper, nickel or iron. Chemical vapor deposition (CVD) of acetylene or methane produces C_2 radicals that forms condensed hexagonal rings (*i.e.* graphene) with π-orbitals sitting on the d- and s- orbitals of the metal surface. This happens on the gas-solid interface at relatively high temperatures. In order to make a graphene walled mesoporous carbon, copper methylacetylide wire crystals are used with coating iron compound layers that prevent the acetylide segregation reaction explosive. Copper nanoparticles are generated and methyl radicals are converted to methane and ethylene leaving C_2 radicals on the surface of copper particles. On the heating of the reactant, copper metals get away form the inner space to outside leaving the quasi-spherical (originally spherical) pores with walls made of two or three graphene layers as shown in figure 1b. As seen in the figure, all carbons in this alveolate

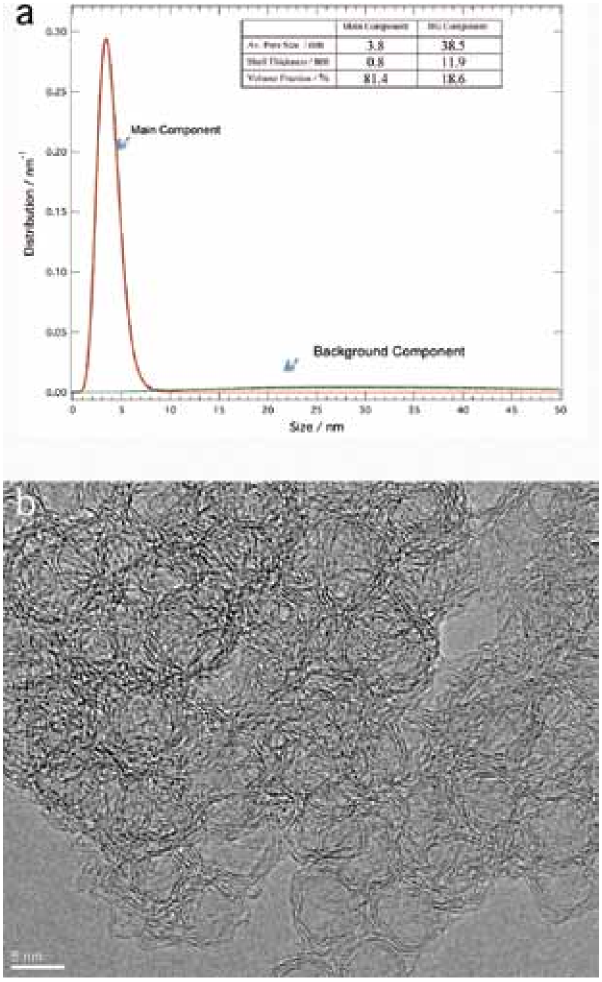

Figure 1. **a**: Core/shell analysis and the pore size distribution of the improved Graphene-multiwalled Alveolate Carbon. **b**: A TEM image of the improved Graphene-multiwalled Alveolate Carbon.

carbon are graphene sheets. Amorphous carbon is evacuated as CO_2 gas leaving micro- or meso-pores in the body and increasing the BET surface area of the alveolate carbon. Now, use of this carbon is under aggressive examination for various battery electrodes.

2. In Situ Preparation and Catalytic Activation Method for Copper Nano-Particles from Acetylide Molecules[1)]

Because metal nanoparticles have a high surface area to volume ratio, they can be highly reactive, cost-effective catalysts. However, metallic surfaces are usually too reactive to maintain their metallic character in the presence of oxygen and/or water vapor. Metal nanoparticle catalysts must be handled carefully to avoid oxidation and inactivation. Here, we suggest a facile in situ preparation method for metal nanoparticle catalysts. Copper acetylide and copper methyl-acetylide molecules are based on ionic bonding, and are relatively stable in air. They can be used as a precursor of copper nanoparticles. Due to their instability at increased temperatures, subsequent annealing promotes a segregation reaction into elemental copper and carbon. Transmission electron microscopy and powder X-ray diffraction revealed that the average diameters of the Cu nanoparticles thus formed were 13.3 and 4.4 nm for C_2Cu_2 and CuCC–CH_3 precursors, respectively. This suggests that the substitution of acetylide molecules can control the size of the resulting copper nanoparticles. The primary advantage of this preparation method is that the functional acetylide group can reduce copper cations. No additional reducing agent is required, so no further separation process is necessary. This presents in situ preparation process. The catalytic activity of the resulting Cu nanoparticles was confirmed for a hydrogen storage system.

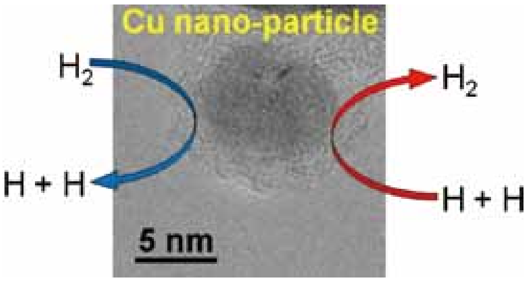

Figure 2. Scheme of hydrogen convertion by Cu nanoparticles covered with amorphous carbon mantles.

3. Weak Ferromagnetism and Strong Spin–Spin Interaction Mediated by the Mixed-Valence Ethynyltetrathiafulvalene-Type Ligand[2)]

A new chromium complex with ethynyl-tetrathiafulvalene (TTF) type ligands, [CrCyclam(C≡C-5-methyl-4’5’ -ethylenedithio-TTF)$_2$]OTf ([**1**]OTf), was synthesized. The cyclic voltammetry of the complex shows reversible two oxidation waves owing to the first and second oxidation of TTF unit. The electrochemical oxidation of [**1**]OTf in Bu_4NClO_4 or Bu_4NBF_4 solution of acetonitrile-chlorobenzene 1:1 mixture gave isostructural crystals of [**1**]$[ClO_4]_2(PhCl)_2$(MeCN) and [**1**]$[BF_4]_2(PhCl)_2$(MeCN), where two mixed-valence TTF units of adjacent complexes form dimer cation radical. The crystal structures are characterized by the alternate chain of $S = 3/2$ Cr^{3+}Cyclam units and $S = 1/2$ $(TTF)^{2+}$ dimers. These two paramagnetic components are connected directly by ethynyl group, resulting in the strong intra-chain spin-spin interaction of $2J/k_B = -30$ and –28 K for $[ClO_4]^-$ and $[BF_4]^-$ salts, respectively ($H = -2J\Sigma_i S_i \cdot S_{i+1}$). Both salts show weak-ferromagnetic transition at 23 K thanks to inter-chain anti-ferromagnetic interaction between TTF dimers. The remanent magnetizations and coercive forces of non-oriented samples at 1.8 K are 0.016 μB and 90 mT for the $[ClO_4]^-$ salt, and 0.010 μB and 50 mT Oe for the $[BF_4]^-$ salt, respectively. The weak-ferromagnetism is attributed to the Dzyaloshinsky-Moriya interaction between adjacent TTF dimers and / or the single ion anisotropy of $[\mathbf{1}]^{2+}$.

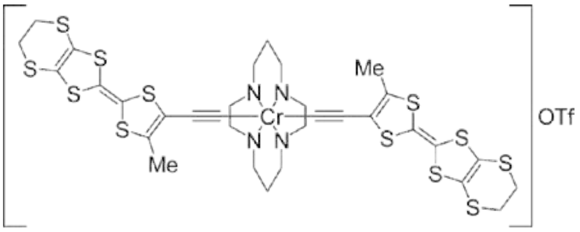

[**1**]OTf

References

1) K. Judai, S. Numao, J. Nishijo and N. Nishi, *J. Mol. Catal. A: Chem.* **347**, 28–33 (2011).

2) J. Nishijo, K. Judai and N. Nishi, *Inorg. Chem.* **50**, 3464–3570 (2011).

---

* Present Address; Nagoya Institute of Technology, Tokyo Institute of Technology

† Present Address; College of Humanities and Sciences, Nihon University

Characterization of Magnetic Ultrathin Films by Novel Spectroscopic Methods

Department of Materials Molecular Science
Division of Electronic Structure

YOKOYAMA, Toshihiko	Professor
NAKAGAWA, Takeshi	Assistant Professor
TAKAGI, Yasumasa	Assistant Professor
EGUCHI, Keitaro	Graduate Student
FUNAKI, Yumiko	Secretary
IWATA, Yumi	Secretary
KOSHIMIZU, Junko	Secretary

Novel properties of magnetic metal ultrathin films have been attractive both from fundamental interest and from technological requirements. We are especially interested in drastic modification of metal thin films by surface chemical treatment such as adsorption-induced spin transitions and morphological changes. The magnetic properties are characterized by means of several kinds of spectroscopic methods like MOKE (Magneto-Optical Kerr Effect) using UV-visible lasers and XMCD (X-ray Magnetic Circular Dichroism) using synchrotron radiation soft X-rays.

Moreover, we have been exploiting new techniques based on UV photoemission magnetic circular dichroism (MCD) such as ultrafast time resolved UV MCD photoelectron emission microscopy (PEEM) for spatiotemporal magnetic imaging.

1. Growth Process and Magnetic Properties of Fe Nanoparticles Deposited on Si_3N_4/Si(111)-(8×8)

The magnetic properties of ferromagnetic transition metals on Si substrates have been widely investigated for the exploitation of new magnetic devices. Since clean Si surfaces react with transition metals very easily to form usually non-magnetic transition-metal silicides, it is essential to insert some inert film between transition metals and Si substrate. No reports have been however published for epitaxially ordered substrates on Si(111). In the present study, we investigated growth processes and magnetic properties of Fe deposited on well-defined Si_3N_4/Si(111)-(8×8), by using STM and XMCD.

Figures 1(a) and 1(b) show the STM images of the Si_3N_4/Si(111)-(8×8) substrate surface and 7.5 ML (monolayer) Fe deposited on the substrate. The substrate surface exhibits clear (8×8) superstructure that was also verified by LEED (low energy electron diffraction). The 7.5 ML Fe film shows the formation of Fe nanoparticles with the average diameter of ~6.9 nm. Figure 1(c) shows the Fe *L*-edge XMCD spectra of Fe deposited on Si_3N_4/Si(111)-(8×8) and clean Si(111)-(7×7). It is clearly found that the XMCD signals of Fe/Si_3N_4 are much larger than those of Fe/Si(111), especially for small Fe coverages. Figure 2(d) shows the magnetization curves of 1.6

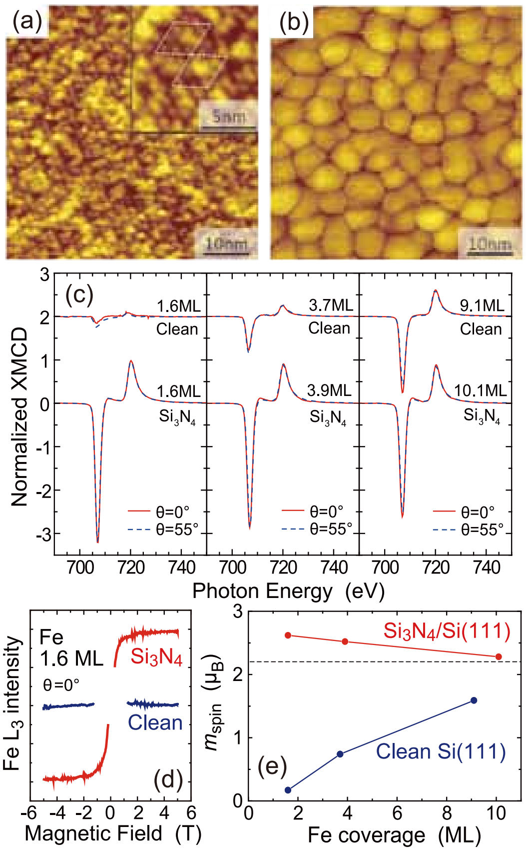

Figure 1. (a,b) 55×55nm^2 STM images of (a) Si_3N_4/Si(111)-(8×8) substrate and (b) the 7.5 ML Fe deposited film on the substrate. (c) Fe $L_{3,2}$-edge XMCD of Fe on clean Si(111) and Si_3N_4 at $\mu_0 H$ = ±5 T and T = 5 K. The X-ray incidence angles θ are 0° (normal incidence) and 55° (grazing). (d) Magnetization curves of 1.6 ML Fe on clean Si(111) (blue) and Si_3N_4 (red), taken at T = 5 K and θ = 0° by fixing the photon energy at the L_3 peak top. (e) Spin magnetic moments m_{spin} of Fe on clean Si(111) (blue) and Si_3N_4 (red) at T = 5 K as a function of Fe coverage.

ML Fe on the two substrates, again exemplifying a large and almost no magnetization of Fe on Si_3N_4 and clean Si(111), respectively. The XMCD spectra in Figure 1(c) allow us to obtain spin and orbital magnetic moments by using the so-called sum rules. The results are given in Figure 1(e). On clean Si(111)-(7×7), the spin magnetic moment is very small at low coverage and is enhanced with the increase in Fe coverage. On the contrary, Fe/Si_3N_4 has a much larger spin magnetic moment of 2.62 μ_B, which is even larger than that of bcc bulk Fe (2.2 μ_B). Such a drastic difference between the clean Si and Si_3N_4 substrates is caused by the fact that the Si_3N_4 substrate effectively suppresses the silicide formation. Because of the weak interaction with the Si_3N_4 substrate and the mismatch of the lattice constant, Fe/Si_3N_4 grows as nanoparticles that exhibit superparamagnetism. A larger spin magnetic moment at small Fe coverage is attributed to the size effect; the reduction of the particle size enhances the ratio of surface atoms that may exhibit larger magnetic moments.

2. Anharmonicity and Quantum Effects in Thermal Expansion of an Invar Alloy1)

Anomalously small thermal expansion over a wide temperature range in an iron-nickel alloy with a nickel concentration of around 35% was discovered by Guillaume in 1897, who was awarded the Nobel Prize in Physics in 1920. The effect is well known as the Invar effect and has been utilized in various kinds of industrial products. It has been recognized that the effect originates from magnetism. A basic concept of the Invar effect is that there exist at least two types of electronic states in Fe, typically high-spin (HS) and low-spin (LS) states. In this two-state model, the equilibrium potential energy is lower in the HS state than in the LS one, while the equilibrium atomic radius is larger in the former. This results in the compensation of thermal expansion due to increasing density of the LS state at higher temperature. Computational simulations at finite temperatures have also been carried out for the understanding of magnetization and thermal expansion. There have been, however, no reports concerning quantum-mechanical dynamics calculations, such as path-integral Monte Carlo (MC) simulations, although in general thermal expansion inherently results from anharmonic vibration, to which the quantum effect is essentially important at low temperature. In this work, we have investigated the anharmonicity and quantum effects in the Invar alloy $Fe_{64.6}Ni_{35.4}$. We have performed Fe and Ni *K*-edge extended x-ray-absorption fine-structure (EXAFS) spectroscopic measurements and the computational simulations based on the path-integral effective-classical-potential (PIECP) theory.

Figure 2(a) show the cohesive energies of hypothetical *fcc* Fe and the Invar alloy as a function of the lattice distance. In the present atomic potentials, fcc Fe shows that the LS state is more stable by 8.0 meV than the HS state, while the Invar case exhibits a more stable HS state by 25.0 meV. The bond distances of the HS and LS states are around R_{HS} = 2.530 Å and R_{LS} = 2.490 Å, respectively. Figures 2(b) and 2(c) show the first nearest-neighbor (NN) shells around Fe and Ni, respectively. Those around Fe show almost no thermal expansion, while those around Ni exhibit meaningful but smaller expansion than that of fcc Ni. At low temperature (< 100 K), the quantum effect is found to play an essentially important role. This is confirmed by comparing the quantum-mechanical simulations to the classical ones, the latter of which exhibit large (normal) thermal expansion at low temperature.

It is also revealed that thermal expansion for the Ni–Ni and Ni–Fe pairs is noticeably suppressed, even though the Ni electronic state may not vary depending on the temperature. On the other hand, the anharmonicity (asymmetric distribution) clearly exists for all the first NN shells as in the case of the normal thermal expansion system, where thermal expansion originates almost exclusively from the anharmonic interatomic potential. This implies the breakdown of the direct correspondence between thermal expansion and anharmonicity in a simple two-body model.

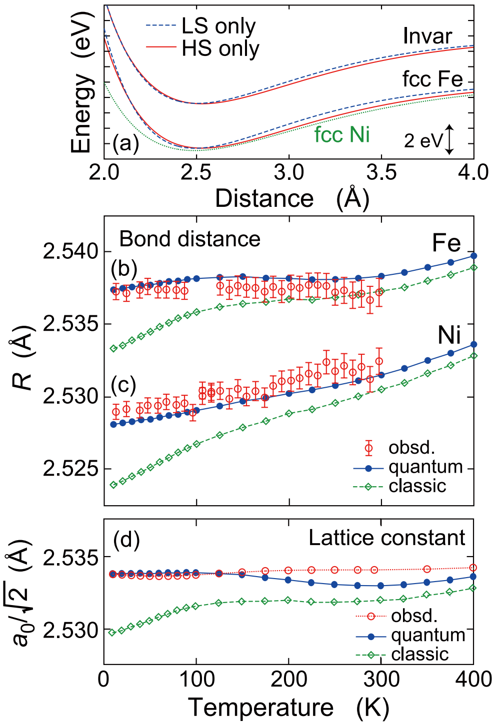

Figure 2. (a) Cohesive energies of Invar $Fe_{64.6}Ni_{35.4}$ (top lines), *fcc* Fe (bottom lines), and *fcc* Ni (bottom, green dotted line) as a function of the 1st NN distance at a temperature of 0 K. For Fe, two types of the potentials for the HS (red solid line) and LS (blue dashed line) states are depicted. (b),(c) Simulated 1st NN bond distance around Fe (b) and Ni (c) given by the PIECP (blue circles and solid line, quantum) and the classical MC (green diamond and dashed line, classic) methods, together with the experimental EXAFS data (red open circle with an error bar). (d) Equilibrium 1st NN distance ($a_0/\sqrt{2}$) given by the PIECP and classical MC simulations, together with the experimental literature data (red circle and dotted line).

Reference

1) T. Yokoyama and K. Eguchi, *Phys. Rev. Lett.* **107**, 065901 (2011).

Design and In-Situ Characterization of Catalyst Surfaces

Department of Materials Molecular Science
Division of Electronic Structure

TADA, Mizuki	Associate Professor
MURATSUGU, Satoshi	Assistant Professor
WENG, Zhihuan	Post-Doctoral Fellow
MAITY, Niladri	Post-Doctoral Fellow
ZHANG, Shenghong	Post-Doctoral Fellow
WATTANAKIT, Chularat	Visiting Scientist
TABTHONG, Sittichoke	Visiting Scientist
THUMRONGPATANARAKS, Wipavee	Visiting Scientist
GAN, Raymond	Visiting Scientist
JIANG, Lu	Visiting Scientist
WANG, Fei	Graduate Student
SAIDA, Takahiro	Graduate Student*
ISHIGURO, Nozomu	Graduate Student†
KUSHIDA, Yuko	Graduate Student†
VU, Thang	Graduate Student‡
FUNAKI, Yukino	Technical Fellow
USUI, Chika	Technical Fellow
GONDO, Makiko	Technical Fellow
FUKUTOMI, Yukiyo	Secretary

1. Preparation of Molecularly Imprinted Ru-Complex Catalysts for Asymmetric Transfer Hydrogenation in Water

We have prepared molecularly imprinted metal-complex catalysts on oxide surfaces, whose ligand is utilized as a template. A molecularly imprinted cavity memorized the shape and coordination environment of a template ligand can be prepared on a catalytically active metal complex behind the template from the supported metal complex. We have prepared molecularly imprinted Ru-complex catalysts on a SiO_2 surface for asymmetric transfer hydrogenation in water by stacking of organic polymer-matrix overlayers on the SiO_2 surface for the molecular imprinting of the supported Ru complex.

Molecularly imprinted Ru-complex catalysts were prepared by step-by-step procedures illustrated in Figure 1: (1) the attachment of a Ru complex on SiO_2, (2) the coordination of a template ligand ((*R*)-1-(*o*-fluorophenyl)ethanol), which is the product of *o*-fluoroacetophenone hydrogenation, (3) stacking of surface matrix overlayers using organic or inorganic polymer matrices, and (4) the removal of the template ligand from the Ru complex. We utilized hydrophobic organic polymer matrices for the transfer hydrogenation in water media and conducted several methods to prepare surface matrix overlayers on SiO_2: (a) photopolymerization of ThreeBond 3026E containing acrylate oligomer and 2-hydroxyethyl methacrylate, (b) vapor deposition polymerization of styrene and divinylbenzene, (c) precipitation polymerization of methylmethacrylate and ethyleneglycol dimethacrylate, and (d) hydrolysis-polymerization of tetramethoxysilane. The structures of the supported and molecularly imprinted Ru catalysts were characterized by XPS, solid-state NMR, XRF, TGA, UV/vis, and Ru K-edge XAFS.

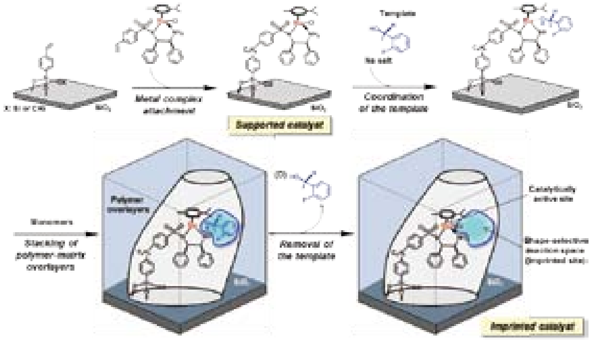

Figure 1. Preparation scheme of a molecularly imprinted Ru-complex catalyst on SiO_2 for the transfer hydrogenation of *o*-fluoroacetophenone in water.

XPS peak intensity analysis of Si 2p to C 1s of the polymer-stacked Ru catalysts showed that the stacking manner of these polymer matrices on the SiO_2 surface were significantly different. In the case of the photopolymerization of ThreeBond 3026E, we found large decrease in the peak intensity ratio, indicating that space around the supported Ru complex was covered by the polymer matrices. The stacking of the matrix overlayers changed catalytic behaviors for the *o*-fluoroacetophenone transfer hydrogenation in water and the improvement of enantioselectivity was observed.

2. Space-Resolved XAFS Analysis of A Single Catalyst Particle of A Supported Ni Catalyst Using X-Ray µ-Beam

Catalytic performances of solid catalysts depend on the structural and electronic aspects (oxidation state, coordination symmetry, local coordination structure, *etc.*) of catalysts, which are generally inhomogeneous powder assembly of solid particles with nm–µm sizes. X-ray beam for conventional XAFS (X-ray Absorption Fine Structure) is typically in mm size, which obtains macroscopically averaged structural information on the assembly of heterogeneous catalyst particles with various sizes, composition, and structures within mm-sized X-ray beam-spot. Structural bond information around a particular catalytic element in an individual catalyst particle has not been reported well because of the lack of characterization techniques with fine space resolution to directly observe such structural parameters of a single catalyst particle.

We have investigated the structural information of a single catalyst particle of a supported Ni catalyst ($NiO_x/Ce_2Zr_2O_y$ ($0 \le x \le 1$, $7 \le y \le 8$) for CH_4 steam reforming by 2-dimensional scanning µ-XRF and µ-XAFS analysis using an X-ray µ-beam (1000 nm (*h*) × 800 nm (*v*)). X-ray beam at Ni K-edge (8332 eV) was focused by Kirkpartick-Baez (KB) mirrors at the BL37XU beamline at SPring-8. The catalyst particles (average particle size = 750 ± 370 nm) were dispersed on a thin SiO_2 membrane substrate and the membrane was mounted on a piezoelectric translation stage for scanning µ-XRF and µ-XAFS. Fluorescent X-rays emitted from the sample were detected by a 19-element Ge detector.

2-Dimensional scanning µ-XRF mapping showed the position of each catalyst particle on the SiO_2 substrate (Figure 2 (A)). Significant contrast of the Ni Kα and Ce Lα + Lβ fluorescent X-rays was observed as shown in Figure 2 (A) and the size of the high X-ray intensity area was consistent to the size of the catalyst particles. Ni K-edge µ-XANES of both $Ni/Ce_2Zr_2O_7$, which was active for the CH_4 steam reforming, and $NiO/Ce_2Zr_2O_8$, which was inactive for the reaction, were measured at the positions of the catalyst particles, and the µ-XANES spectra of the both catalysts were significantly different each other as shown in Figure 2 (B) ((a) and (c)).

Figure 2 (C) shows a Ni K-edge µ-EXAFS Fourier transform of a single catalyst particle of the inactive $NiO/Ce_2Zr_2O_8$, recorded for 3 h. To our knowledge, the local coordination structure of the supported Ni species on a single catalyst particle was successfully analyzed for the first time by µ-EXAFS with the spatial resolution to the size of the catalyst particle. The Ni K-edge µ-EXAFS analysis of $NiO/Ce_2Zr_2O_8$ revealed the local coordination of the catalytically inactive Ni species (Ni–O and Ni–Ni), which was attributed to the NiO species. The µ-XAFS technique would be promising to explore new *in situ* space-resolved catalysis science, to understand catalysis of a single nanoparticle excluding noise information from the heterogeneous properties of the catalyst particle assembly.

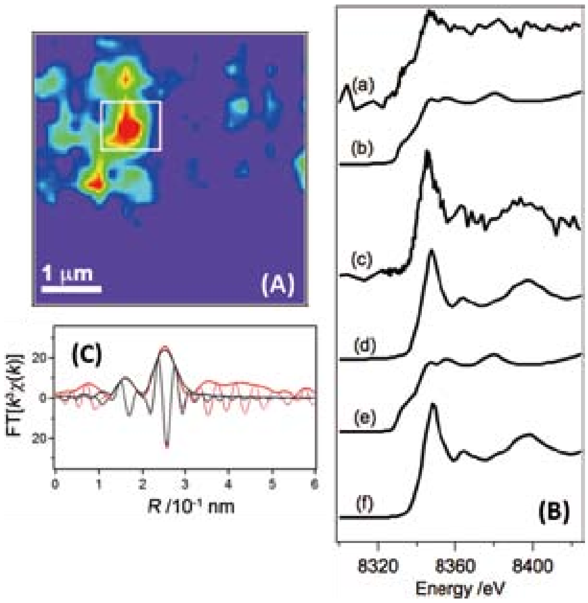

Figure 2. (A) A 2D-scanning Ni Kα XRF mapping image of $Ni/Ce_2Zr_2O_7$. 1 pixel = 200 nm. A white square in the image represents the beam area of (B)-(a). (B) Ni K-edge XANES spectra: (a) µ-XANES of a $Ni/Ce_2Zr_2O_7$ particle, (b) conventional XANES of $Ni/Ce_2Zr_2O_7$ powder assembly, (c) µ-XANES of a $NiO/Ce_2Zr_2O_8$ particle, (b) conventional XANES of $NiO/Ce_2Zr_2O_8$ powder assembly, (e) Ni foil, and (f) NiO. (C) Ni K-edge Fourier transform of a $NiO/Ce_2Zr_2O_8$ catalyst particle. Red and black lines represent on the observed and fitted spectra.

References

1) Z. Weng, S. Muratsugu, N. Ishiguro, S. Ohkoshi and M. Tada, *Dalton Trans.* **40**, 2338–2347 (2011).

2) M. Tada, N. Ishiguro, T. Uruga, H. Tanida, Y. Terada, S. Nagamatsu, Y. Iwasawa and S. Ohkoshi, *Phys. Chem. Chem. Phys.* **13**, 14910–14913 (2011).

* carrying out graduate research on Cooperative Education Program of IMS with Sinshu University

† carrying out graduate research on Cooperative Education Program of IMS with The University of Tokyo

‡ carrying out graduate research on Cooperative Education Program of IMS with JAIST

Studies of Charge-Order State in Organic Conductors

Department of Materials Molecular Science
Division of Electronic Properties

YAKUSHI, Kyuya	Professor*
YAMAMOTO, Kaoru	Assistant Professor
URUICHI, Mikio	Technical Associate
YUE, Yue	Post-Doctoral Fellow
ABE, Hitomi	Secretary

In organic conductors, kinetic energy is comparable with on-site and inter-site Coulomb energy. Due to this reason, many organic conductors are located in a boundary area between metallic and insulating states, and thus various organic charge-transfer compounds show metal–insulator phase transition. Recently, charge-ordered (CO) state originated from interelectron Coulomb interaction is widely found in organic conductors. The CO state attracts attention, first because charge-fluctuation-mediated superconductivity is theoretically predicted in superconducting compounds neighbored on CO phase, second because some compounds in CO phase show ferroelectricity. The macroscopic polarization in this ferroelectric transition is recognized not as the result of ionic displacements, but as the result of coherent integration of electronic polarizations induced by the CO transition. We have investigated the CO state and metallic state near CO employing infrared and Raman spectroscopy and SHG microscopy.

1. Hydrogen Isotope Effect on the Charge-Ordering Phase Transition in α'-(BEDT-TTF)$_2$IBr$_2$

α'-(BEDT-TTF)$_2$IBr$_2$ has a layered structure with two-dimensional interaction within the layer. In a variety of organic conductors, α'-(BEDT-TTF)$_2$IBr$_2$ is one of the most narrow-bandwidth copounds. Because of the narrow-bandwidth, the charge carriers of this compound is localized, and thus α'-(BEDT-TTF)$_2$IBr$_2$ is an insulator in a whole temperature range from 350 K to 4.2 K. This insulating compound shows succesive phase transitions at 207 K, ~160 K, and ~30 K. The resistivity jump at 207 K is regarded as an order-disorder phase transition of localized holes.$^{1)}$ Below ~160 K, macroscopic polarization evolves, suggesting a ferroelectric phase transition. Finally this compoonds undergoes a first order magnetic phase transition at ~30 K. Our goal is to understand the mechanism of this succesive phase transition. In this section, we focus on the hydrogen isotope effect on the order-disorder phase transition at 207 K.

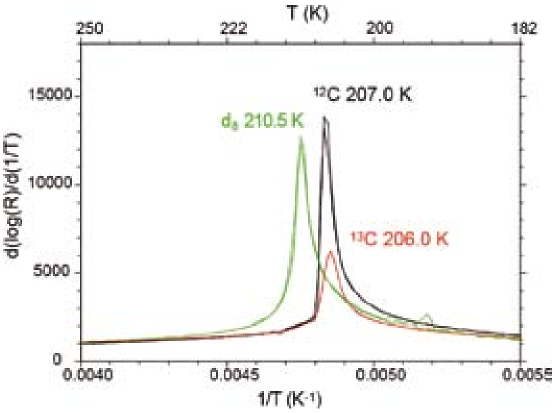

Figure 1. Comparison of the derivatives of electrical resistivity of α'-(BEDT-TTF)$_2$IBr$_2$, deuterium-substituted compound, α'-(d$_8$-BEDT-TTF)$_2$IBr$_2$, and ^{13}C-substituted compound, α'-(^{13}C-BEDT-TTF)$_2$IBr$_2$ where ^{13}C is substituted at the central C=C bond of BEDT-TTF. α'-(d$_8$-BEDT-TTF)$_2$IBr$_2$ shows a significant isotope effect on the order-disorder phase transition.

Figure 1 shows the derivative of the electrical resistance, (d(log$R$)/d(1/T)), where the peak temperature corresponds to the phase transition temperature, T_c. As shown in this figure, Tc of α'-(d$_8$-BEDT-TTF)$_2$IBr$_2$ shows a high-temperature shift of 3–4 K. The unit cell volume of α'-(d$_8$-BEDT-TTF)$_2$ IBr$_2$ shrinks by about 0.4% compared with that of α'-(BEDT-TTF)$_2$IBr$_2$. The volume change can be regarded as the result of chemical pressure. If we assume that the chemical pressure pushes up T_c, the isotope shift means $dT_c/dP > 0$. However, this assumption is opposite to the experimentally obtained pressure dependence of T_c, $dT_c/dP < 0$.$^{1)}$ Therefore, the isotope effect cannot be attributed to the effect of chemical pressure. We therefore propose a small polaron model, in which the effective transfer integral is reduced as $\tilde{t} = t\exp(-S)$, where $S = (E_b/\hbar\omega_0)\coth(\hbar\omega_0/2kT)$ is a vibrational overlap factor (Huang-Rhys factor). The deuterium substitution may soften the optical phonon mode ω_0, and increases S. This effect reduces the effective transfer integral, and thus the bandwidth. The decrease of bandwidth is regarded as the application of negative pressure. Combined with the relationship, $dT_c/dP < 0$, this small polaron model can qualitatively explain the isotope effect on the phase transition. We speculate that the librational modes around the short axis and the axis perpendicular to the molecular plane work most effectively as the optical phonon ω_0.

2. Inhomogeneous Ferroelectric Polarization in α'-(BEDT-TTF)$_2$IBr$_2$ Revealed by Second-Harmonic Generation Microscopy[2)]

As an effort to expand the material family of unconventional class of ferroelectrics, we focused in the present study on α'-(BEDT-TTF)$_2$IBr$_2$, which is another BEDT-TTF complex with trihalide anions similar to α-(BEDT-TTF)$_2$I$_3$. As expected from the similarity in the crystal structure, we have confirmed that the complex shows charge ordering at low temperatures[1)] in a separate study. The result of SHG measurements indeed verified that the complex also showed SHG in a charge-ordered phase, though the transition features of the complex turned out to be substantially different from those of the triiodide complex.

One of the interesting features is an inhomogeneous generation of SH signal from a single crystal, revealed by mapping measurement of SHG. The spatially resolved observation was performed for a filmy singly crystal (t = *ca.* 3 μm) in transmission geometry using a homemade scanning laser microscope equipped with an Er-doped fiber laser (λ = 1.55 μm, pulse duration: 100 fs, repetition: 20 MHz). The laser beam was focused by an objective lens into a spot (ϕ = *ca.* 20 μm) on the *ab*-plane of the crystal with an excitation power density of less than *ca.* 500 W/cm^2. To efficiently dissipate the heat at the spot, the crystal was embedded in polymer resin, afterwards sandwiched by a pair of two sapphire slides, then cooled by a liquid He flowing cryostat.

Figure 2 shows the comparison of the transmission and SHG images of the single crystal. As shown by the crack observed in the transmission image [Figure 2(a)], the crystal was cleaved together with the polymer matrix when cooled. As is displayed in Figure 2(b), the SHG image shows uneven distribution of the nonlinear optical signal; the signal was emanated from limited regions near the cracks and the edges of the crystal, whereas other regions far from cracks are almost completely dark.

Note that the SHG signal is generated not only from the very end of the crystal edges at the crack, but regions with a macroscopic width. This clearly indicates that the activation of SHG is not caused by the surface effect at the crack, but should be a manifestation of the breakdown of centrosymmetry in the bulk region. The uneven signal distribution is presumably attributed to inhomogeneous pressure distribution associated with the crack in polymer matrix generating at low temperatures; the matrix adhering to a sapphire plate should feel a stretching force (since the thermal expansion coefficient of the polymer is larger than sapphire), whereas the region near the crack would be free from the stretching force. Hence, the region near the crack, emanating the SHG light, seems to represent the ambient pressure property of the bulk state.

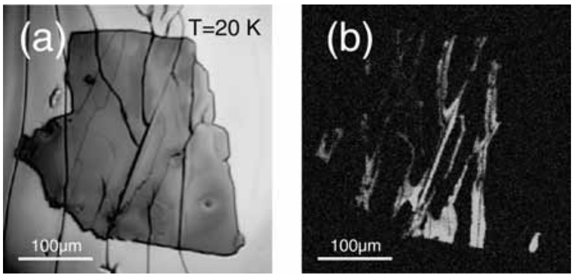

Figure 2. (a) Transmission image of a single crystal of α'-(BEDT-TTF)$_2$IBr$_2$ embedded in polymer resin, and (b) its SH image measured at 20 K. The SHG intensity in (b) is in proportional to the brightness.

The coexistence of the dark region in the image would be noteworthy. This indicates that the generation of the ferroelectric polarization is suppressed presumably by a small negative pressure, suggesting that a non-polar phase exists near the ferroelectric CO phase in the phase diagram. One may notice that the bright and dark regions are divided by clear boundaries, which fact implies that these two phases would be separated by a first-order transition.

The appearance of the distinct phases strongly suggests that there would be several stable arrangements for the charge order as realized for the spin system with geometrical frustration. To understand the intriguing features of the ferroelectric transition in this compound, precise crystal geometry at low temperatures as well as the SHG data measured without application of mechanical stress is necessary.

References

1) Y. Yue, *et al.*, *J. Phys. Soc.* **78**, 044701 (2009).
2) K. Yamamoto *et al.*, *Physica B* **405**, S363 (2010).
3) K. Yamamoto, *et al.*, *J. Phys. Soc. Jpn.* **77**, 074709 (2008).

Award

YAMAMOTO, Kaoru; JPSJ Award Article 2011.

---

* Present Address; Toyota Physical and Chemical Research Institute

Magnetic Resonance Studies for Molecular-Based Conductors

Department of Materials Molecular Science
Division of Electronic Properties

NAKAMURA, Toshikazu	Associate Professor
FURUKAWA, Ko	Assistant Professor
SUGIURA, Koichi	Graduate Student
ABE, Hitomi	Secretary

Magnetic resonance measurements are advantageous for studying fundamental electronic properties and for understanding the detailed electronic structures of molecular based compounds. Developing an understanding of the electronic phases and functionality of these materials enables us to perform systematic investigations of low-dimensional, highly-correlated electron systems and functional materials. Competition between the electronic phases in molecular-based conductors has attracted much attention. The investigations of such electronic phases by magnetic resonance measurements are important to understanding unsolved fundamental problems in the field of solid state physics, and to explore novel functionalities in the field of material science.

In this study, we performed broad-line NMR and ESR measurements on molecular-based conductors to understand electron spin dynamics and functionality in low-temperature electronic phases.

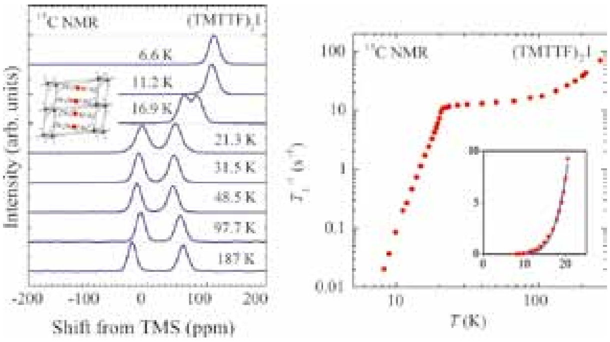

Figure 1. (Left) Temperature dependence of the ^{13}C-NMR spectra of a single crystal of (TMTTF)$_2$I Frequencies are referenced against tetramethylsilane. (Right) Temperature dependence of the ^{13}C-NMR, spin-lattice relaxation rate, T_1^{-1}, of (TMTTF)$_2$I. The inset is the low-temperature region, drawn with a linear scale. The blue line shows fitting results that assumed a simple gap, with Δ ~ 128 K.

1. Structural Investigation of the Spin-Singlet Phase in (TMTTF)$_2$I

To elucidate the electronic state that exists in the boundary region between the spin-singlet phase and the high-pressure side antiferromagnetic phase in the modified generalized phase diagram, we carried out x-ray diffraction, electron spin resonance, and nuclear magnetic resonance measurements of the tetramethyl-tetrathiafulvalene (TMTTF) family salt, (TMTTF)$_2$I. The unit-cell volume of (TMTTF)$_2$I is between that of (TMTTF)$_2$Br and (TMTTF)$_2$PF$_6$. We found that (TMTTF)$_2$I undergoes a spin-singlet phase transition at 21 K without involving paramagnetic charge-ordering phase. Therefore, the charge-ordering transition is not necessary for the spin-singlet transition of TMTTF salts as seen in other conventional spin-singlet salts. Finally, we discuss possible mechanisms of the spin-singlet phase transition.

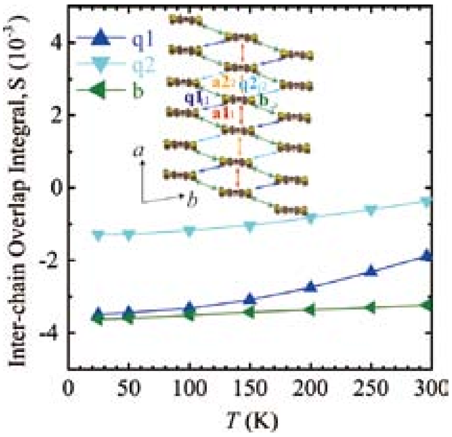

Figure 2. Temperature dependence of the overlap integral of (TMTTF)$_2$I down to 25 K focusing on the inter-chain overlap integral. The overlap parameters within the *ab*-plane are defined in the inset.

2. Photoinduced Triplet States of Photoconductive TTF Derivatives Including a Fluorescent Group

The spin dynamics of photoconductive tetrathiafulvalene (TTF) derivatives containing 2,5-diphenyl-1,3,4-oxadiazole (PPD) was examined using time-resolved electron spin resonance (TR-ESR) spectroscopy. TR-ESR signals of a frozen solution sample under visible excitation were attributed to the excited triplet state $\mathbf{T}_1$, which was populated via intersystem crossing from the excited singlet state $\mathbf{S}_1$ as confirmed by TR-ESR spectral simulations. From DFT calculations, the spin density distribution of the $\mathbf{T}_1$ state was found to be concentrated around the linker between the TTF and PPD molecules.

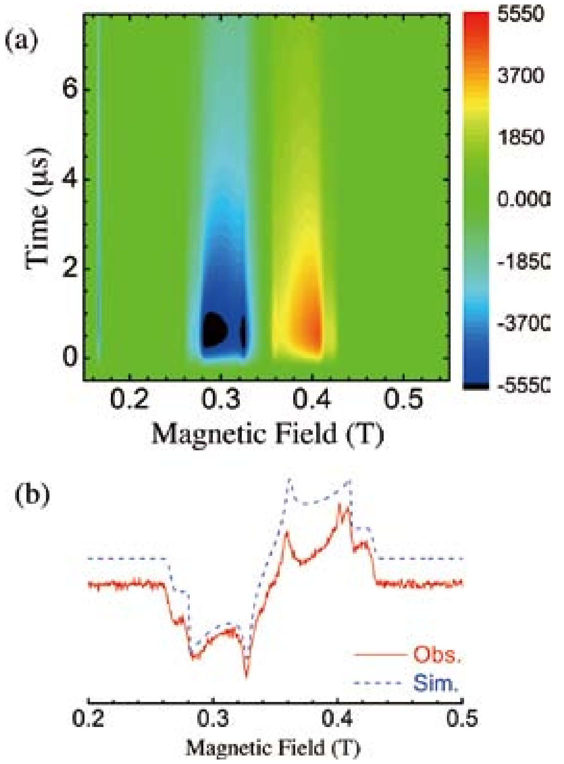

Figure 3. (a) 2D pulsed TR-ESR spectra for photoconductive TTF derivatives containing PPD. The normal axis represents the ESR signal intensity. The color scale denotes the signal intensity. Positive and negative values indicate the absorption and emission of microwaves, respectively. (b) Slice spectra along the magnetic field axis at $t = 0.5$ μs and $T = 20$ K. The solid and dotted lines denote the observed and simulated spectra, respectively.

3. Magnetic Memory Based on Magnetic Alignment of a Paramagnetic Ionic Liquid near Room Temperature

A paramagnetic ferrocenium-based ionic liquid that exhibits a magnetic memory effect coupled with a liquid–solid phase transformation has been developed. Based on field alignment of the magnetically anisotropic ferrocenium cation, the magnetic susceptibility in the solid state can be tuned by the weak magnetic fields (< 1 T) of permanent magnets.

4. Completely Hydrostatic Pressure Effect of Anisotropic Resistivity in the 1-D Organic Conductor $(TMTTF)_2SbF_6$

The anisotropic resistivity of $(TMTTF)_2SbF_6$ under hydrostatic pressure was investigated up to ~0.3 GPa using a helium gas pressure control system. The resistivity along the *a* axis shows a metallic behavior above a crossover temperature T_ρ (~220 K at ambient pressure) and an insulating behavior below T_ρ. On the other hand, the temperature dependence of $\rho_{b'}$ and ρ_c was found to show a kink at a charge ordered temperature T_{CO}. Interestingly, T_ρ was increased with applying pressure while T_{CO} was decreased with applying pressure. We discuss this unusual feature in terms of the pressure–temperature phase diagram in the $(TMTCF)_2X$ system.

5. ^{13}C NMR Study of the Magnetic Properties of the Quasi-One-Dimensional Conductor, $(TMTTF)_2SbF_6$

Magnetic properties in the quasi-one-dimensional organic salt $(TMTTF)_2SbF_6$ are investigated by ^{13}C C NMR under pressures. Antiferromagnetic phase transition at ambient pressure (AFI) is confirmed. Charge-ordering is suppressed by pressure and is not observed under 8 kbar. For $5 < P < 20$ kbar, a sharp spectrum and the rapid decrease of the spin-lattice relaxation rate $1/T_1$ were observed below about 4 K, attributed to a spin-gap transition. However, as the reduction of the Knight shift was not observed, the phase is not conventional non-magnetic spin-Peierls. Above 20 kbar, extremely broadened spectrum and critical increase of $1/T_1$ were observed. This indicates that the system enters into another antiferromagnetic phase (AFII) under pressure. The slope of the antiferromagnetic phase transition temperature T_{AFII}, dT_{AFII}/dP, is positive, while T_{AFI} decreases with pressure. The magnetic moment is weakly incommensurate with the lattice at 30 kbar.

References

1) K. Furukawa, K. Sugiura, F. Iwase and T. Nakamura, *Phys. Rev. B* **83**, 184419 (5 pages) (2011).
2) K. Furukawa, Y. Sugishima, H. Fujiwara and T. Nakamura, *Chem. Lett.* **40**, 292–294 (2011).
3) Y. Funasako, T. Mochida, T. Inagaki, T. Sakurai, H. Ohta, K. Furukawa and T. Nakamura, *Chem. Commun.* **47**, 4475–4477 (2011).
4) M. Itoi, Y. Ishii, H. Kitano, S. Takekoshi, K. Matsubayashi, Y. Uwatoko and T. Nakamura, *Physica C* **470**, S594–S595 (2011).

Design of Porous Polymer Frameworks

Department of Materials Molecular Science
Division of Molecular Functions

JIANG, Donglin	Associate Professor
NAGAI, Atsushi	Assistant Professor
KOU, Yan	Post-Doctoral Fellow
LIU, Xiaoming	Post-Doctoral Fellow
GUO, Zhaoqi	Post-Doctoral Fellow
XU, Yanhong	Graduate Student
DING, Xuesong	Graduate Student
JIN, Shangbin	Graduate Student
CHEN, Xiong	Graduate Student
FENG, Xiao	Graduate Student
CHEN, Long	Graduate Student
SUZUKI, Hiroko	Secretary

Covalent organic frameworks (COFs) are a new class of porous architectures that allow the integration of organic units with atomic precision into long-range-ordered two and three-dimensional structures. From a synthetic point of view, COFs are intriguing since they allow a new degree of control of porosity, composition and component positions. However, the construction of COFs to date has been limited to certain monomers, and the lack of suitable protocols utilizing other units has impeded further advances in this emerging field. To advance this emerging field it is important to extend the limited number of synthetic protocols and monomer units available. In our group, we have developed various π-electronic 2D COFs with porphyrin and phthalocyanine.[1–3]

Conjugated microporous polymers (CMPs) are another class of porous frameworks consisting of extended π-conjugation and inherent nanopores. As high surface-area porous materials, CMPs emerge as a new medium for gas adsorption and have been developed as a new type of nanoreactors and heterogeneous catalysts upon the integration of catalytic sites into the skeletons.[4] From a synthetic point of view, CMPs are unique because they allow the elaborate control of both skeletons and pores. In this context, a promising way to the exploration of CMPs is to combine the structural advantages of being π-conjugation and possessing inherent pores. We have developed such a cooperative porous framework based on aza-fused CMPs for supercapacitive energy storage and electric power supply.[5]

1. Two-Dimensional Phthalocyanine Polymer and Covalent Organic Framework

NiPc-COF was synthesized by the boronate esterification reaction of $(OH)_8$NiPc and 1,4-benzene diboronic acid (BDBA) in dimethylacetamide (DMAc)/*o*-dichlorobenzene under solvothermal conditions (Figure 1a). PXRD patterns of NiPc-COF exhibited strong diffraction peaks at 3.78°, 7.72°, 11.56° and 26.62° assignable to 100, 200, 300 and 001 facets, respectively. Based on the PXRD pattern, the center-to-center distance between neighboring pores was evaluated as 2.36 nm and the separation between the sheets as 3.32 Å. Simulations using the *P*4/*mmm* space group with $a = b = 23.12247$ Å and $c = 3.36358$ Å gave a PXRD pattern in good agreement with the experimentally observed pattern. The phthalocyanine units are

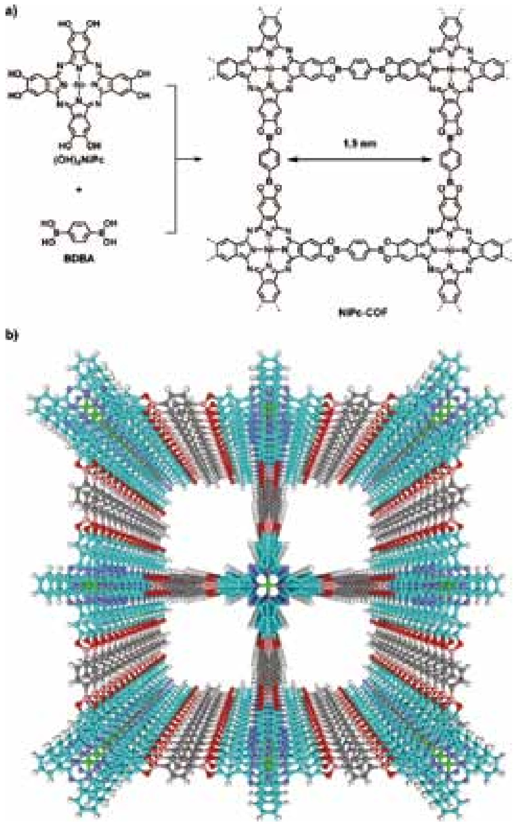

Figure 1. a) Schematic representation of the synthesis of NiPc-COF based on boronate esterification reaction. b) Eclipsed stack of phthalocyanine 2D sheets and microporous channels in NiPc-COF (a 2 × 2 grid). Colors used for identification are as follows: phthalocyanine unit (sky blue), Ni (green), N (violet), C (grey), O (red), B (orange) and H (white).

located at nodes separated by 2.3 nm in the 2D plane and stack to form layers separated by a distance of 3.36 Å. In contrast, the staggered arrangement resulting from an *I*4 space group did not reproduce the experimental pattern. In this stacking, the phthalocyanine units overlap on the pores of the neighboring planes.

Owing to ordered stacking of the phthalocyanine units, NiPc-COF becomes photoconductive, generating a prominent photocurrent. Irradiation from a Xenon light source (> 400 nm) with a UV cut-off module resulted in a significant increase in current from 20 nA (dark current) to 3 μA (photocurrent). Further, on-off switching experiments showed that NiPc-COF quickly responded to light irradiation and that the photocurrent can be switched on and off many times without deterioration. In contrast, $(MeO)_8NiPc$ did not show any photoresponse under the same conditions. To investigate the wavelength dependence of the photosensitivity, we irradiated with light passed through band-path filters (± 5 nm). NiPc-COF was panchromatically responsive to different wavelengths and was extremely sensitive to deep-red and near-infrared photons. The increased light-harvesting capability and enhanced carrier mobility accounts for the high photoconductivity and sensitivity. Therefore, owing to well-ordered stacking of the phthalocyanine unit, NiPc-COF shows enhanced light-harvesting capability in the visible and near-infrared regions, is semiconducting and facilitates charge carrier transport. NiPc-COF is highly photoconductive, exhibiting a panchromatic light response and exceptional sensitivity to visible and near-infrared photons. These properties are unique and highly correlated with the structure of NiPc-COF. The remarkable results demonstrate the enormous potential of two-dimensional polymers in novel optoelectronics applications.

2. Aza-Fused Conjugated Microporous Polymers for Supercapacitive Energy Storage and Electric Power Supply

Supercapacitors are energy storage and power supply devices that are in increasing demand with the broadening of applications such as vehicles and electric devices. Supercapacitive energy storage operates on the electric double layer by accumulation of charges at the electrode/electrolyte interface, where the stored energy is proportional to the capacitance of the electrode. Therefore, a breakthrough in the electrode materials holds the key to fundamental advances in supercapacitors. Despite the extensive efforts in synthesis, the rational design of supercapacitive electrodes that meet large capacitance, high energy density, and outstanding stability remains a substantial challenge.

Aza-CMPs were synthesized by the condensation reaction of 1,2,4,5-benzenetetramine with triquinoyl hydrate (Figure 2, Aza-CMPs). Aza-CMPs comprise four features: (1) fused CMP frameworks that are conductive, (2) aza units in the skeletons that enable dipolar interaction with electrolyte cations and accumulate protons on the walls of pores, (3) inherent micropores with optimized size that allows quick ion motion during charge-discharge processes, and (4) high surface area provide large interface for the formation of electrostatic charge-separation layers in the pores. Ultimately, these structural features work cooperatively, leading to exceptional energy storage and power supply capacities.

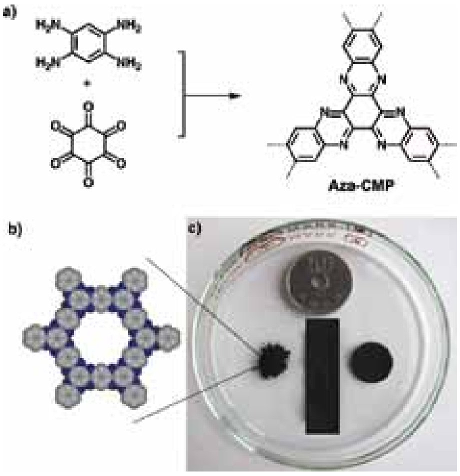

Figure 2. a) Schematic representation of the synthesis of Aza-CMP. b) The elementary pore structure of Aza-CMPs (grey is carbon network and blue is nitrogen). c) Photographic image of the powder and flexible thin films with different shapes of Aza-CMPs.

We have explored CMPs for supercapacitive energy storage, through the construction of an aza-fused porous framework with built-in aza units and high surface-area micropores. The fused skeleton, dense aza units, and well-defined micropores work cooperatively and facilitate electrostatic charge-separation layer formation. Consequently, Aza-CMPs exhibit large capacitance, high energy and power densities, and enable repetitive energy storage and power supply with excellent cycling life. These remarkable results demonstrate the enormous potential of conjugated microporous polymers in the exploration of energy materials.

References

1) X. Ding, L. Chen, Y. Honsho, X. Feng, O. Saengsawang, J. Guo, A. Saeki, S. Seki, S. Irle, S. Nagase, P. Vudhichai and D. Jiang, *J. Am. Chem. Soc.* **133**, in press (2011).
2) X. Feng, L. Chen, Y. Dong and D. Jiang, *Chem. Commun.* **47**, 1979–1981 (2011).
3) X. Ding, J. Guo, X. Feng, Y. Honsho, J. Guo, S. Seki, P. Maitarad, A. Saeki, S. Nagase and D. Jiang, *Angew. Chem., Int. Ed.* **50**, 1289–1293 (2011).
4) Y. Kou, Y. Xu, Z. Guo and D. Jiang, *Angew. Chem., Int. Ed.* **50**, 8753–8757 (2011). (VIP)
5) L. Chen, Y. Yang, Z. Guo and D. Jiang, *Adv. Mater.* **23**, 3149–3154 (2011).

Solid State NMR for Structural Biology

Department of Materials Molecular Science
Division of Molecular Functions

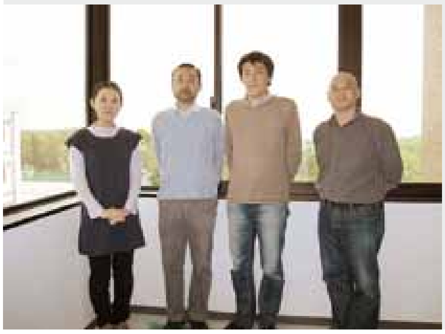

NISHIMURA, Katsuyuki	Associate Professor
IIJIMA, Takahiro	Assistant Professor
TANIO, Michikazu	IMS Research Assistant Professor

We are working on methodology and hardware developments of solid state NMR and structural biology based on them. In the following, we show developed variable temperature (VT) magic angle spinning (MAS) probe for ultra high field NMR and preliminary result of newly constructed over expression system of a peripheral membrane protein. In addition, a dynamics study of paramagnetic compound was reported.

1. Development of VT-MAS Solid-State NMR Probe for Ultra High Field 920 MHz NMR

Solid state NMR under ultra high field opens up new possibilities of experiments respect to spectral resolution and sensitivity of spectra. Unfortunately, none of sample temperature controllable solid-state NMR probes are available in ultra high field NMR facilities in Japan. This situation restricts usability and possibilities of solid state NMR studies under ultra high field in Japan.

In order to overcome this situation, we have developed ^{1}H-^{13}C double resonance VT-MAS probe based on JEOL 920MHz MAS probe. We have designed original VT control system for MAS probe, machined parts and built in JEOL 920 MHz MAS probe as show in Figure 1 (a). In the developed probe, a bearing gas for MAS was temperature controlled. Thus, all of bearing gas line was replaced by originally designed glass Dewar tubes. Since probe length was extremely long, Dewar was separated into two pieces. Those were jointed by optimally designed adapter, then a cartridge heater was built in bottom Dewar. The control of sample temperature was realized through feedback control of cartridge heater by monitoring gas temperature at a position close to sample tube. Upper and lower limits of available temperatures are limited by the material of stator and available chiller temperature, respectively. Stably available temperature range was verified experimentally from 0 to 60 °C which is sufficient range for studies of biomolecules.

Figure 1 (b) and (c) are photos of VT-MAS probe built in ultra high field magnet together with peripherals. For studies of biomolecules, precise temperature control of samples are required in order to retain those structures and functions. It is expected that this probe opens up the possibilities of studies for such samples. Finally the author K.N. appreciates to members of Equipment Development Center in IMS for their help.

Figure 1. (a) The bottom view of newly developed VT-MAS probe. (b) The side view of VT-MAS probe loaded into 920 MHz ultra high field magnet (21.6 T). (c) The side view of VT-MAS probe and peripherals enabling VT.

2. Structural Characterization of Peripheral Membrane Protein by Solution and Solid State NMR

Phospholipase C-δ1 (PLC-δ1) hydrolyzes phosphatidylinositol 4,5-bisphosphate (PIP$_2$) in the plasma membrane to produce the second messengers on the membrane surface. The pleckstrin homology (PH) domain in the N-terminus of PLC-δ1 selectively forms high affinity complex with PIP$_2$ in the plasma membrane and inositol 1,4,5-triphosphate (IP$_3$) in the cytoplasm. Consequently those complex formations regulate membrane localization of PLC-δ1. So far, we have reported rat-PLC-δ1 PH domain changes its conformation depending on curvatures of lipid bilayers and micelles.[1] In this study, we established the over expression system of the PH domain of human PLC-δ1, and performed preliminary NMR analysis of the recombinant protein.

The plasmid containing the hPH gene, corresponding to the PH domain (residues 1-142) of human PLC-δ1, was transformed into *Escherichia coli* BL21(DE3) strain. To produce the isotope labeled hPH, the transformed *E. coli* was incubated in M9 medium containing stable isotopes. The harvested *E. coli* cells were purified using GST-affinity chromatography followed by gel-filtration chromatography. The purified hPH shows IP_3-binding activity as judged by Native PAGE gel shift analysis (data not shown), indicating that the recombinant protein is correctly folded.

Figure 2 shows two-dimensional ^{1}H-^{15}N heteronuclear single quantum coherence (HSQC) solution NMR spectra of the ligand-free (black signals) and IP_3-complex forms (red signals) of the uniformly ^{15}N-labeled hPH. The chemical shift dispersion of the ^{1}H and ^{15}N resonances in the spectrum of the ligand-free hPH also indicated that the recombinant hPH is substantially folded. The addition of IP_3 resulted in chemical shift displacements of many resonances (Figure 2, red signals), indicating that the IP_3 binding induces a large conformational change of hPH. Solid state NMR studies of the hPH-PIP_2 complex in membrane, as well as ligand-binding studies for the several mutants of hPH, are in progress.

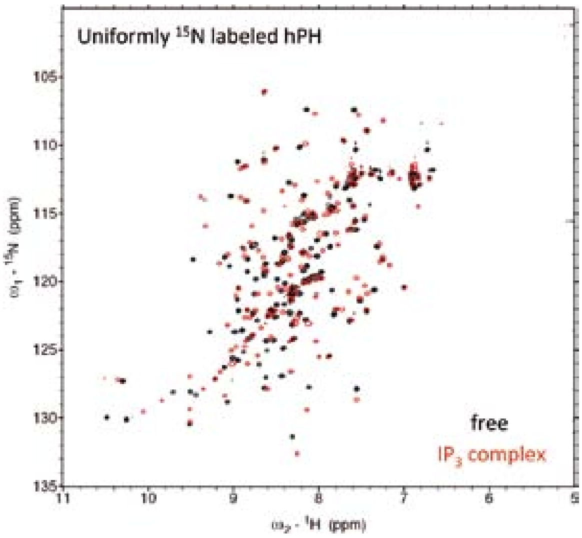

Figure 2. ^{1}H-^{15}N HSQC solution NMR spectra of uniformly ^{15}N-labeled hPH in the absence (black) and the presence of IP_3 (red) at 20 °C. Molar ratio of hPH and IP_3 was 1:1.3.

3. ^{2}H QCPMG NMR of Paramagnetic Solids as a Probe of Molecular Dynamics

Solid state NMR is a powerful technique to investigate dynamics of molecules and ions in substances. In particular, deuterium (^{2}H, $I = 1$) NMR can probe motions with timescale ranging from nanosecond to second by several methods such as a quadrupole echo, quadrupolar Carr-Purcell-Meiboom-Gill (QCPMG), magic-angle-spinning, two-dimensional NMR and relaxation experiments. Compared to measurement by the quadrupole echo sequence, the QCPMG technique where a train of spin echo generated by repeatedly irradiated refocusing pulses is acquired can enhance sensitivity of ^{2}H NMR spectra and extend dynamic range, although it has been employed only for diamagnetic compounds. Recently, we have developed a ^{2}H QCPMG method efficient for paramagnetic solids.

In this work, we applied the QCPMG method to probe molecular dynamics of paramagnetic solids. Figure 3 shows temperature dependences of ^{2}H NMR spectra of paramagnetic powder of $CoSiF_6$ $6H_2O$ under 9.4 T. Asymmetric lineshape is caused by the paramagnetic interaction between ^{2}H and unpaired electrons in Co^{2+}. For the QCPMG spectra, drastic change was observed in this temperature range, which is due to a reorientation of $[Co(H_2O)_6]^{2+}$ around the C_3 axis. For the echo spectra, however, lineshape of the spectra at low temperatures (293–313 K) are almost the same and small change was observed at high temperatures (373–393 K). By a simulation of the QCPMG spectra (Figure 3(ii)), ^{2}H interaction parameters of quadrupole coupling constant (C_Q) and asymmetric parameter (η) as well as a rate constant for the reorientational motion of $[Co(H_2O)_6]^{2+}$ (k_{re}) also shown in the Figure 3 were obtained successfully. With these parameters, the echo spectra were reproduced (Figure 3(iv)). It was found that the ^{2}H QCPMG technique to extend dynamic range is also effective for paramagnetic compounds.

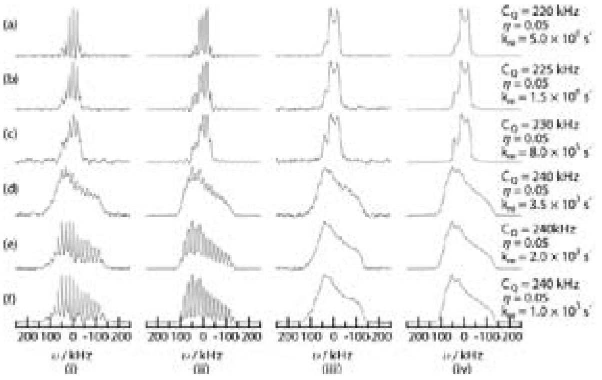

Figure 3. Temperature dependence of ^{2}H NMR spectra of paramagnetic $CoSiF_6 \cdot 6H_2O$ obtained by the QCPMG (i, ii) and echo (iii, iv) sequences. (i, iii) and (ii, iv) show the observed and simulated spectra, respectively. (a)–(f) are the spectra at 393, 383, 373, 313, 303 and 293 K, respectively.

Reference

1) N. Uekama, T. Aoki, T. Maruoka, S. Kurisu, A. Hatakeyama, S. Yamaguchi, M. Okada, H. Yagisawa, K. Nishimura and S. Tuzi, *Biochim. Biophys. Acta* **1788**, 2575–258 (2009).

Organic Solar Cells

Research Center for Molecular Scale Nanoscience
Division of Molecular Nanoscience

HIRAMOTO, Masahiro	Professor
KAJI, Toshihiko	Assistant Professor
IKETAKI, Kai	IMS Fellow
NAKAO, Satoru	Post-Doctoral Fellow
SHINMURA, Yusuke	Research Fellow
KUBO, Masayuki	Research Fellow
YOKOYAMA, Kazuya	Research Fellow
YOSHIOKA, Tadashi	Research Fellow
ISHIYAMA, Norihiro	Graduate Student
OTSUBO, Yuko	Secretary
SUGIHARA, Hidemi	Secretary

Organic solar cell is recognized as a future 3rd generation solar cell. In 2009, we started CREST Project; “Bandgap Science for Organic Solar Cells.” Target of this project is 15% efficiency of organic solar cells by establishing bandgap science for organic semiconductors, which is equivalent to that for silicon semiconductor.

Conductivity (σ) is related both carrier concentration (n) and carrier mobility (μ) [$\sigma = en\mu$]. To achieve high efficiency, cell resistance ($\rho = 1/\sigma$) should be decreased by increasing both n and μ. Former and latter relate Topics 1 , 2 and Topic 3, respectively.

1. Conduction-Type Control of C_{60} Films from *n*- to *p*-Type by MoO_3 Doping[1)]

As in the case of inorganic solar cells, precise conduction type control, *i.e.*, *pn*-control is indispensable to fabricate efficient organic solar cells consisting of *pn* and *pin* junctions.

In this study, conduction-type control of highly purified 7N (seven nines; 99.99999%) C_{60} films from *n*- to *p*-type by doping with molybdenum oxide (MoO_3) was demonstrated. The energetic value of the Fermi level (E_F), 4.50 eV, for nondoped C_{60} films measured by the Kelvin vibrating capacitor method was positively shifted to 5.88 eV, and approached the valence band by the coevaporated doping of MoO_3 at a concentration of 3300 ppm (Figure 1).

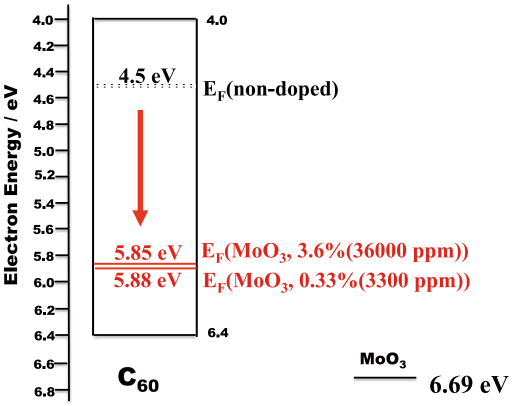

Figure 1. Positive shift of Fermi level (E_F) for C_{60} films by MoO_3 doping.

Due to the observation of charge transfer (CT) absorption between C_{60} and MoO_3, and ability of electron extraction of MoO_3 from the valence band of C_{60} (Figure 1), we concluded that the formation of CT complex [C_{60}^{+}-MoO_3^{-}]. Positive charge on C_{60}^{+} can be liberated from the negative charge of the MoO_3^{-} by the heat energy of room temperature (Figure 2). Increase of the free hole concentration causes the large positive shift of E_F. Formation of *p*-type C_{60} was also confirmed based on the photovoltaic properties.

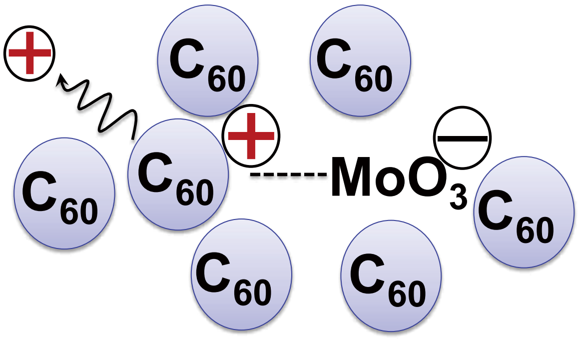

Figure 2. Mechanism of MoO_3-doping.

2. Doping-Based Control of the Energetic Structure of Photovoltatic Co-Deposited Films[2)]

Doping based pn-control technique for co-deposited films should be developed to enhance cell efficiency since recent organic solar cells incorporate co-deposited films to generate significant photocurrent densities based on the dissociation of excitons by the photoinduced electron transfer process.

In this study, energetic structures of C_{60}:6T (α-sexithiophene) co-deposited films were intentionally tuned from *n*-type Schottky junctions through metal/intrinsic/metal junctions to *p*-type Schottky junctions by ppm-level doping with MoO_3.

‘Three component co-evaporation’ technique was developed for the doping of MoO_3 into the C_{60}:6T co-deposited films. Precise monitoring of the deposition rate of the MoO_3

using a computer monitoring system allowed us to dope with MoO_3 to as low as 70 ppm in volume concentration. Light was irradiated on ITO electrode for the cells, ITO/MoO_3-doped C_{60}:6T/MoO_3/Ag (Figure 3).

For non-doped (0 ppm) and 400 ppm MoO_3-doped cells, photocurrent appeared in the region from 500 to 700 nm, where there is weak absorption from the cells (masking effect). This means that an *n*-type Schottky junction was formed at the C_{60}:6T/MoO_3 interface (Figure 4(a)). For 600 ppm-doped cell (Figure 3), the photocurrent was distributed equally throughout the wavelength region from 300 to 700 nm, *i.e.*, the generation of photocurrent occurs in the whole of the bulk of the cell. This means that the co-deposited film behaves as 'intrinsic' material (Figure 4(b)). For 1100 and 4300 ppm-doped cells (Figure 3), photocurrent appeared in the strong absorption region (300–500 nm). This means that a *p*-type Schottky junction was formed at the ITO/C_{60}:6T interface (Figure 4(c)).

We are now trying to fabricate *pn*- and *pin*-homojunctions to create built-in potentials directly in the co-deposited films to realize high efficient organic solar cells.

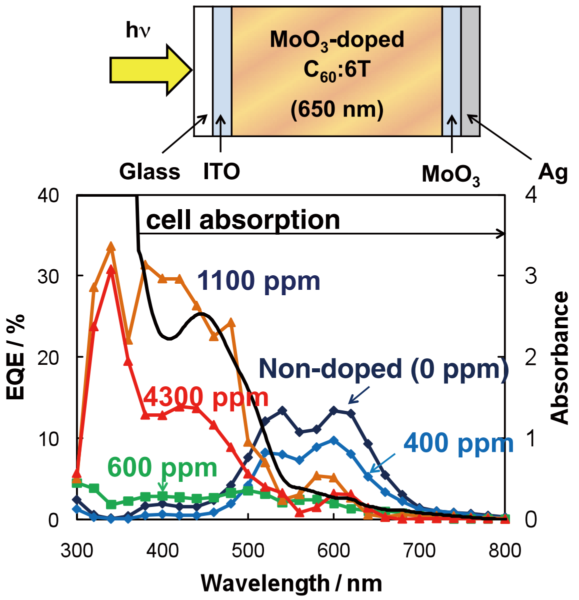

Figure 3. Action spectra of the external quantum efficiency (EQE) of the short-circuit photocurrent. Black curve shows cell absorption.

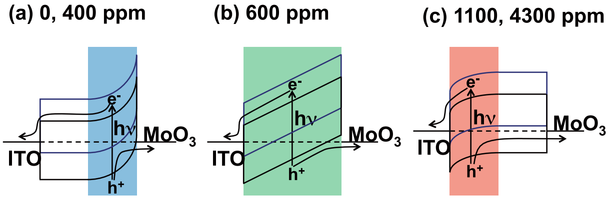
(a) 0, 400 ppm
(b) 600 ppm
(c) 1100, 4300 ppm

Figure 4. Energetic structures of the ITO/C_{60}:6T/MoO_3 cells for various MoO_3-doping concentrations.

3. Co-Evaporant Induced Crystalline Co-Deposited Films in Organic Solar Cells[3)]

Nano-structure control of co-deposited films, *i.e.*, route formation for electrons and holes photogenerated in the co-deposited films is indispensable to fabricate efficient organic solar cells.

In this study, a novel method for crystallizing co-deposited films is developed. This method utilizes a liquid as a non-sticking co-evaporant during vacuum deposition (Figure 5).

Photocurrent enhancement was observed particularly for relatively thick (~400 nm) co-deposited films having greater light absorption (Figure 5). Co-deposited films based on H_2Pc and C_{60} with much improved crystallinity have been produced by introducing co-evaporant and confirmed by analysis using UV-Vis, XRD and FESEM (Figure 5). Striking enhancement in photocurrent generation is achieved in organic solar cells without exception, based on a variety of co-deposited films such as PbPc:C_{60}, AlClPc:C_{60}, and rubrene:C_{60}. We believe that this method is generally applicable for growing high-quality crystalline films by vacuum deposition and opens the possibility of producing high-performance organic solar cells.

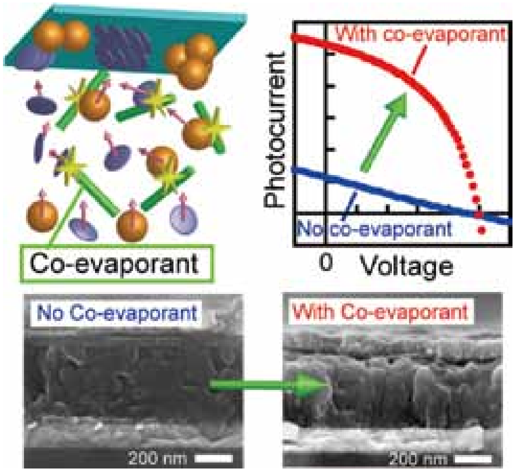

Figure 5. (Upper-left) Model of co-evaporant induced crystallization. Additional co-evaporant molecules hit C_{60} and phthalocyanines (Pc) at or near the substrate and promoting crystallization in the co-deposited film. (Upper-right) Photocurrent-voltage charactereistics of H_2Pc:C_{60} co-deposited cells with/without co-evaporants, showing dramatic improvements of cell performances. (Lower) Enhanced crystallization is clearly observed in the co-deposited film with a co-evaporant, including a transformation of the grain from a random structure without the co-evaporant to a column structure with the co-evaporants.

References

1) M. Kubo, K. Iketaki, T. Kaji and M. Hiramoto, *Appl. Phys. Lett.* **98**, 073311 (2011).
2) N. Ishiyama, M. Kubo, T. Kaji and M. Hiramoto, *Appl. Phys. Lett.* **99**, 133301 (2011).
3) T. Kaji, M. Zhang, S. Nakao, K. Iketaki, K. Yokoyama, C. W. Tang and M. Hiramoto, *Adv. Mater.* **23**, 3320 (2011).

Development of Organic Semiconductors for Molecular Thin-Film Devices

Research Center for Molecular Scale Nanoscience
Division of Molecular Nanoscience

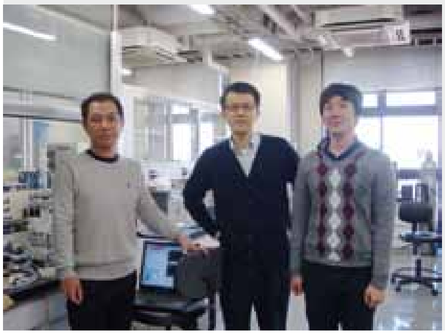

SUZUKI, Toshiyasu	Associate Professor
SAKAMOTO, Youichi	Assistant Professor
KURODA, Yasuhiro	Graduate Student
WATANABE, Yoko	Secretary

Organic light-emitting diodes (OLEDs) and organic field-effect transistors (OFETs) based on π-conjugated oligomers have been extensively studied as molecular thin-film devices. Organic semiconductors with low injection barriers and high mobilities are required for highly efficient OLEDs and OFETs. Radical cations or anions of an organic semiconductor have to be generated easily at the interface with an electrode (or a dielectric), and holes or electrons must move fast in the semiconducting layer. Compared with organic p-type semiconductors, organic n-type semiconductors for practical use are few and rather difficult to develop. Recently, we found that perfluorinated aromatic compounds are efficient n-type semiconductors for OLEDs and OFETs.

1. Selective and Random Syntheses of [*n*] Cycloparaphenylenes (*n* = 8–13) and Size Dependence of Their Electronic Properties[1)]

[*n*]Cycloparaphenylenes (*n* = 8–13, CPPs) were synthesized, and their physical properties were systematically investigated. [8] and [12]CPPs were selectively prepared from the reaction of 4,4’-bis(trimethylstannyl)biphenyl and 4,4”-bis (trimethylstannyl)terphenyl, respectively, with Pt(cod)Cl_2 (cod = 1,5-cyclooctadiene) through square-shaped tetranuclear platinum intermediates. A mixture of [8]–[13]CPPs was prepared in good combined yields by mixing biphenyl and terphenyl precursors with platinum sources. Products were easily separated and purified by using gel permeation chromatography. In ^{1}H NMR spectra, the proton of the CPPs shifts to a lower field as *n* increased due to an anisotropic effect from the nearby PP moieties. Although the UV-vis spectra were rather insensitive to the size of the CPPs, the fluorescence spectra changed significantly in relation to their size. A larger Stokes shift was observed for the smaller CPPs. Redox properties of the CPPs were measured for the first time by using cyclic

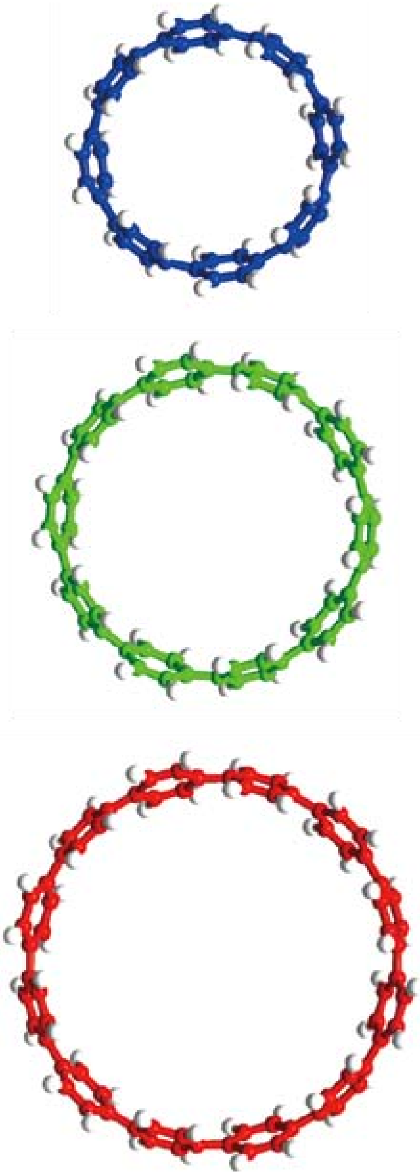

Figure 1. [8], [10], and [12]CPPs.

voltammetry, and the smaller CPPs had lower oxidation potentials. The results are consistent with the HOMO energies of CPPs, of which the smaller CPPs had higher energies.

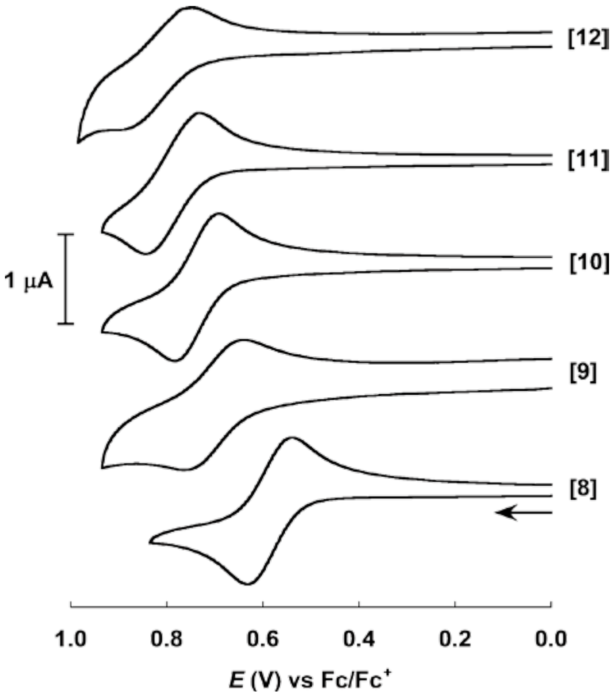

Figure 2. Cyclic voltammograms of [8] to [12]CPPs at 100 mV/s in 1,1,2,2-tetrachloroethane containing 0.1 M (n-Bu)$_4$NPF$_6$.

Reference

1) T. Iwamoto, Y. Watanabe, Y. Sakamoto, T. Suzuki and S. Yamago, *J. Am. Chem. Soc.* **133**, 8354–8361 (2011).

Building Photosynthesis by Artificial Molecules

Research Center for Molecular Scale Nanoscience
Division of Molecular Nanoscience

NAGATA, Toshi	Associate Professor
KAWAO, Masahiro	IMS Fellow
KON, Hiroki	Post-Doctoral Fellow
MIURA, Takahiro	Graduate Student
YUSA, Masaaki	Graduate Student
WANATABE, Yoko	Secretary

The purpose of this project is to build nanomolecular machinery for photosynthesis by use of artificial molecules. The world's most successful molecular machinery for photosynthesis is that of green plants—the two photosystems and related protein complexes. These are composed almost exclusively from organic molecules, plus a small amount of metal elements playing important roles. Inspired by these natural systems, we are trying to build up multimolecular systems that are capable of light-to-chemical energy conversion. At present, our interest is mainly focused on constructing necessary molecular parts.

1. Photoreaction of Zinc Porphyrin/Co(II) Polypyridine Dyad Molecules with Hydroquinones as Electron Donors

Combination of photoinduced electron transfer and redox chemistry of transition metal complexes is an attractive way to achieve useful photochemical energy and materials conversion. We are particularly interested in systems having organic pigments as photosensitizers and first-row transition metals as catalytic sites.

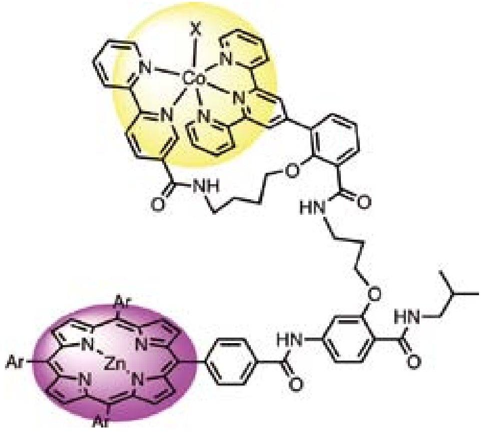

Figure 1. The Zn porphyrin/Co(II) complex dyad molecules.

Along this line, we prepared a series of dyad molecules consisting of zinc porphyrins and cobalt(II) complexs (Figure 1). By use of this dyad molecule as a catalyst, we developed a new photoreaction, in which chloroform is reduced to lower chlorinated hydrocarbons with hydroquinone as the electron donor. Hydroquinone is used as the intermediate electron carrier in natural photosynthesis and other biochemical energy conversion systems, and the present system is a novel example of photosynthetic model that utilizes hydroquinone as the electron donor.

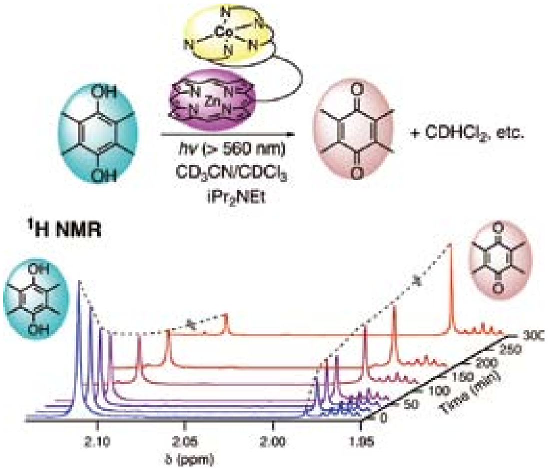

Figure 2. Photoreaction of ZnP/Co dyad with hydroquinone.

Although the detailed reaction mechanism of this photoreaction is still under investigation, one plausible mechanism is shown in Figure 3. The mechanism involves reductive quenching of the excited porphyrin by hydroquinone (or its anionic form), followed by charge shift reaction to generate the Co^{I} intermediate. The Co^{I} species is highly nucleophilic and will easily react with chlorocarbon to produce some active species, which eventually generates the product. This reaction should open the door to utilization of a regenerable electron donor in photochemical materials conversion.

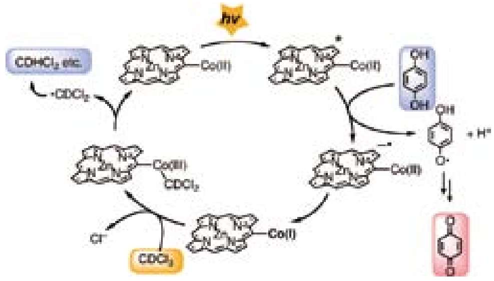

Figure 3. Plausible mechanism of the photoreaction.

2. Improved Synthesis of Single-Molecular Quinone Pools with Internal Redox Gradients and ^{19}F-NMR Handles

As demonstrated in the last section, hydroquinone/quinone interconversion is becoming important as a component of photochemical materials conversion. In this context, the “quinone pool” of natural photosynthesis should need much attention. The quinone pool in natural photosynthesis consists of a collection of plastoquinones embedded in thylacoid membranes, and transport electrons (and protons) between different redox enzymes.

Previously we reported our research on building “single-molecular” quinone pools by use of synthetic dendrimer molecules.[1] Our next targets are (1) quinone pools containing two different quinones with different redox potentials, and (2) linearly extended quinone pools with two different photosystems on both ends. We synthesized the molecule shown in Figure 4, which is a third-generation dendrimer molecule with two different quinones in the internal positions. Although we had already published a quinone pool molecule based on a similar amide-dendrimer framework,[2] our new synthesis employs introduction of protected quinones in the early stage of dendron synthesis, thus allowing generation-selective incorporation of different quinones.

3. Synthesis and Photoreaction of Soluble Phthalocyanines

Although porphyrins are very useful pigments in photosynthetic model systems, they are not optimal in terms of utilizing solar light. In particular, they do not absorb light of wavelength longer than 650 nm, which limits usage of red to near-infrared light. Therefore, it is desirable to use pigments that have strong absorption in this region. Phthalocyanines are good candidates as they have very strong absorption bands around 700 nm. However, incorporating phthalocyanines in complex molecular systems often causes difficulty because of the low solubility of phthalocyanine derivatives. To address this problem, we chose phthalocyanines having 2,4-di-tert-butylphenoxy substituents in the periphery. These phthalocyanines are very soluble in many organic solvents (including hexanes), so that the manipulation is easy.

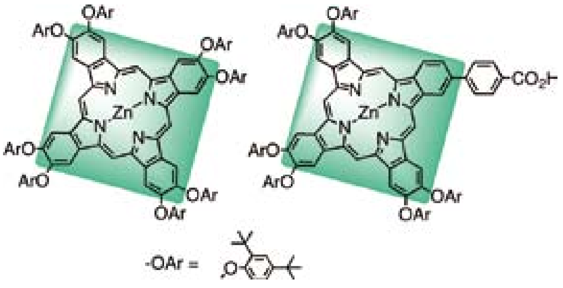

Figure 5. Highly soluble phthalocyanines used in this work.

The high solubility of these phthalocyanines also allowed us to study photoreactions in a solution phase. Thus, the photoreduction of duroquinone by thiophenol was carried out in the presence of phthalocyanine and porphyrin. The results clearly show that phthalocyanine can utilize low-energy light more efficiently than porphyrin.

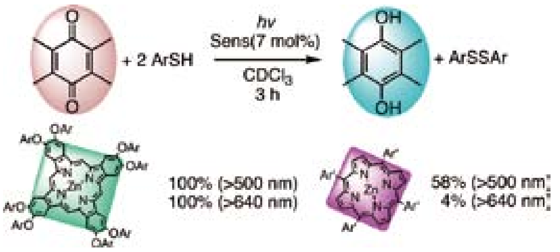

Figure 6. Comparison of photoreaction of phthalocyanine and porphyrin.

References

1) T. Nagata and Y. Kikuzawa, *Biochim. Biophys. Acta* **1767**, 648–652 (2007).

2) T. Nagata, Y. Kikuzawa, T. Nagasawa and S. I. Allakhverdiev, *Trans. Mater. Res. Soc. Jpn.* **34**, 505–508 (2009).

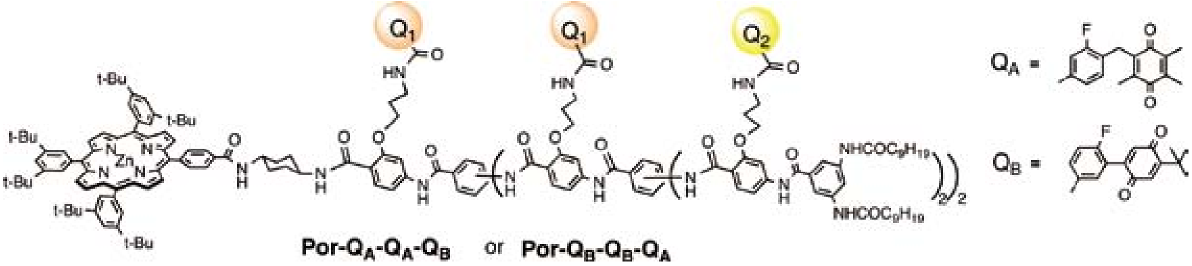

Figure 4. The third-generation quionone pool molecule with internal redox gradient.

Chemistry of Bowl-Shaped Aromatic Compounds and Metal Nanocluster Catalysts

Research Center for Molecular Scale Nanoscience
Division of Molecular Nanoscience

SAKURAI, Hidehiro	Associate Professor
HIGASHIBAYASHI, Shuhei	Assistant Professor
TSURUOKA, Ryoji	IMS Fellow
SAL PRIMA, Yudha S.	Visiting Scientist; JSPS Invited Fellow
MURUGADOSS, Arumugam	Visiting Scientist; JSPS Post-Doctoral Fellow
TAN, Qi-Tao	Visiting Scientist; JSPS Post-Doctoral Fellow
MORITA, Yuki	Post-Doctoral Fellow
KITAHARA, Hiroaki	Post-Doctoral Fellow
BAIG, Nasir R.	Post-Doctoral Fellow
GAYATRI, Gaddamanugu	Visiting Scientist
MISHRA, Vijaya Lakshmi	Visiting Scientist
KAEWMATI, Patcharin	Visiting Scientist
PONGPIPATT, Paweena	Visiting Scientist
HAESUWANNAKIJ, Setsiri	Visiting Scientist
ONOGI, Satoru	Graduate Student
DHITAL, Raghu Nath	Graduate Student
KATAOKA, Keita	Graduate Student
KARANJIT, Sangita	Graduate Student
SHRESTHA, Binod Babu	Graduate Student
PREEDASURIYACHAI, Patcharee	Graduate Student*
NAKANO, Sachiko	Technical Fellow
KAI, Noriko	Technical Fellow
ISHIDA, Yuka	Technical Fellow
KIM, Yukimi	Technical Fellow
SASAKI, Tokiyo	Secretary
TANIWAKE, Mayuko	Secretary

Bowl-shaped π-conjugated compounds including partial structures of the fullerenes, which are called "buckybowls," are of importance not only as model compounds of fullerenes but also as their own chemical and physical properties. For example, in solution they show the characteristic dynamic behavior such as bowl-to-bowl inversion. On the other hand, they sometimes favor stacking structure in a concave-convex fashion in the solid state, giving excellent electron conductivity. Furthermore, some buckybowls are conceivable to possess the bowl-chirality if the racemization process, as equal as bowl-to-bowl inversion, is slow enough to be isolated. Very few buckybowls has been achieved for preparation mainly due to their strained structure, and no report on the preparation of chiral bowls has appeared. In this project, we develop the rational route to the various buckybowls with perfect chirality control using the organic synthesis approach.

We also investigate to develop novel catalytic properties of metal nanoclusters. We focus on the following projects: Preparation of size-selective gold nanoclusters supported by hydrophilic polymers and its application to aerobic oxidation catalysts: Synthetic application using metal nanocluster catalyst: Development of designer metal nanocluster catalyst using the highly-functionalized protective polymers.

1. The Impact of Basis Set Superposition Error on the Structure of π-π Dimers[1)]

The effect of basis set superposition error (BSSE) on the structure and energy of benzene, naphthalene, corannulene, and sumanene dimer has been analyzed. MP2 method was chosen and the effect is estimated using 6-31G, 6-31G(d), 6-311.G(d), cc-pVDZ, and cc-pVTZ basis sets. The model calculations on benzene dimer indicate that the impact of BSSE on the equilibrium geometry of π-stacked dimers appears to be quite significant. Calculations on larger molecular dimers such as the dimers of naphthalene, corannulene, and sumanene are also studied. Our results cautions that whenever a counterpoise correction is significant for the stacking interaction, it is essential to incorporate the BSSE in the geometry optimization. The most often adopted practice of including the BSSE only for the energy and not for the geometry may be not be acceptable for stacking interactions. The impact of BSSE on structure and energy is much higher as the size of the monomeric units of stacked π-dimers is increased. The results on the stacking interactions of the two prototypical buckybowls, corannulene, and sumanene reveal that most of the pragmatic basis sets are essentially associated with a very high correction due to BSSE.

2. *N*-Formylation of Amines Catalyzed by Nanogold Under Aerobic Oxidation Conditions with MeOH or Formalin[2)]

Direct formation of amides from alcohols or aldehydes with amines has recently received attention from the viewpoint of the development of environmentally benign process. In particular, *N*-formylation of amines using MeOH or formaldehyde (especially formalin) is very important. The use of simple reactants makes it possible to understand the reaction mechanism. Furthermore, the starting materials are both economical and the formamide derivatives produced in the reaction are important intermediates in organic synthesis. Until now, though, only a few examples of this transformation have been reported. Cu hydroxyl salts have been used in the presence of hydrogen peroxide. However, aerobic oxidation has been achieved with nanosize-gold supported on metal oxide with MeOH, and formylation of dimethylamine with formaldehyde has been carried out using metallic gold or silver surfaces as a catalyst. Practical procedures for *N*-formylation by aerobic oxidation that tolerate a wide scope of amines are still needed.

Nanosized-gold metal has recently attracted a great deal of interest because of its high activity and potential application in the emerging area of green oxidation chemistry. We have recently demonstrated that gold nanoclusters stabilized by poly(*N*-vinyl-2-pyrrolidone) (**Au:PVP**) act as an excellent quasi-homogenous catalyst for the aerobic oxidation of benzylic alcohols, generation of H_2O_2 in the presence of ammonium formate, homo-coupling reaction of arylboronic acids, and other cyclization reactions. **Au:PVP** was found to be an excellent catalyst for the direct *N*-formylation of amine with MeOH or formalin as a formyl source. In particular, only 1 atom% of catalyst was needed and the reaction proceeded under ambient conditions in the reaction with formalin solution. The results strongly indicate that **Au:PVP** might possess superior catalytic activity toward the oxidation of hemiaminal intermediate when compared to other catalysts. Such characteristic features of **Au:PVP** will be applicable to many types of practical organic syntheses.we wish to report highly selective direct *N*-formylation using MeOH or formalin as a formyl source in the presence of **Au:PVP** under aerobic conditions.

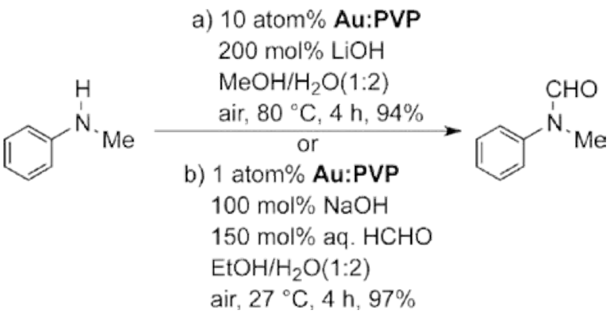

3. Chitosan-Stabilized Gold, Gold–Palladium, and Gold–Platinum Nanoclusters as Efficient Catalysts for Aerobic Oxidation of Alcohols[3]

Chitosan was used as a stabilizer for the synthesis of Au, AuPd and AuPt nanoclusters (NCs). The produced NCs had a narrow particle size distribution with sizes less than 2.3 nm in diameter and were characterized by various techniques such as UV-Visible spectroscopy, X-ray diffraction, X-ray photoelectron spectroscopy, transmission electron microscopy and scanning electron microscope energy dispersive spectroscopy (STEM-EDS). These metal NCs exhibited high catalytic activity toward the aerobic oxidation of various alcohols under ambient conditions comparable with the reported **Au:PVP** catalyst. Au NCs protected by chitosan could easily be recovered for repeated use.

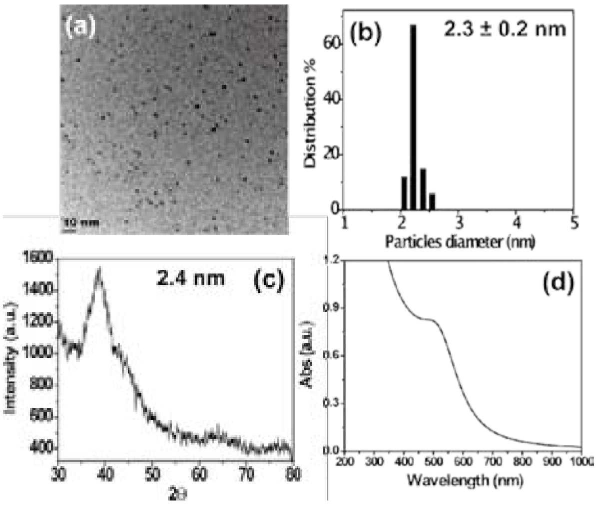

Figure 1. (a) TEM image of chitosan-stabilized Au NCs. (b) Particle size histogram plot obtained from (a). (c) X-ray diffraction pattern of Au:Chit. (d) UV-Visible spectrum of Au:Chit.

4. Magnetically Recoverable Magnetite/Gold Catalyst Stabilized by Poly(*N*-vinyl-2-pyrrolidone) for Aerobic Oxidation of Alcohols[4]

Fe_3O_4:PVP/Au nanocomposite synthesized *via* a two-step procedure was tested as quasi-homogenous catalysts in alcohol oxidation. It was found that the nanocomposite was able to carry out aerobic oxidation of alcohols in water at room temperature. Studies show rapid magnetic recoverability and reusability characteristics.

References

1) D. Vijay, H. Sakurai and G. N. Sastry, *Int. J. Quantum Chem.* **111**, 1893–1901 (2011).
2) P. Preedasuriyachai, H. Kitahara, W. Chavasiri and H. Sakurai, *Chem. Lett.* **39**, 1174–1176 (2010).
3) A. Murugadoss and H. Sakurai, *J. Mol. Catal. A: Chem.* **341**, 1–6 (2011).
4) H. W. Chen, A. Murugadoss, T. S. A. Hor and H. Sakurai, *Molecules* **16**, 149–161 (2011).

---

* carrying out graduate research on Cooperative Education Program of IMS with Chulalongkorn University

Multifunction Integrated Macromolecules for Molecular-Scale Electronics

Research Center for Molecular Scale Nanoscience
Division of Molecular Nanoscience

TANAKA, Shoji Assistant Professor

Recently a single electron tunnel (SET) device has attracted much attention due to the growing demand for ultra-low-power device. A SET device manipulates an electron by means of one-by-one electron transfer, resulting in ultimately low power consumption. However, for room temperature operation, the size of SET device must be as small as a few nm to overcome the thermal fluctuation problems. The process size of a few nm is out of the range of conventional micro-technology. In this project, to establish an innovative fabrication process for SET device systems, we have been developing step-wise synthetic protocols for molecule-based single-electron tunnel devices (MOSET) and circuit.

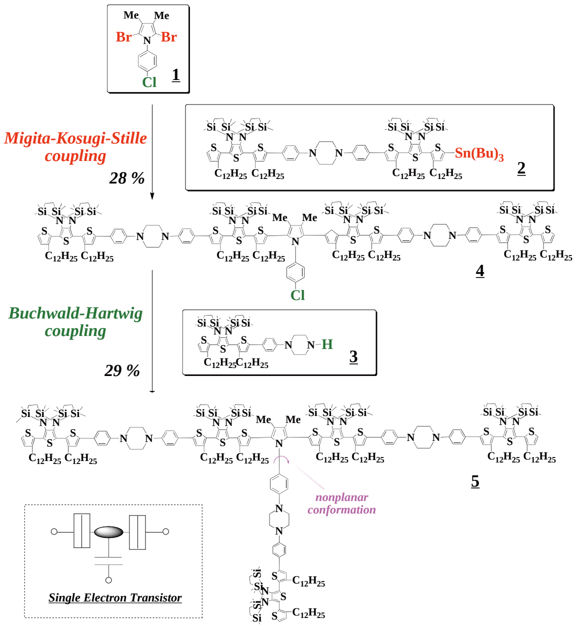

Scheme 1. Step-wise Synthetic Route to Single-electron Transistor.

1. Molecular Design for Mono-Molecular Integration of Basic Components of Single-Electron Devices

Single electron devices comprise three key elements: Coulomb island, tunnel junction, and capacitive junction. To integrate these elements in a single molecule, we have designed versatile molecular building blocks (**1-3**). Using these building blocks, we have synthesized the first trial model of a “mono-molecular” single-electron transistor (Scheme 1). Although there are a lot of issues to be solved, this is the first step to realize the practical MOSET device systems based on mono-molecular integration strategy.

2. Mechanism of Electrical Conduction through Single Oligothiophene Molecules[1)]

The temperature dependence of electrical conductance of oligothiophene molecules with the length of 2.2 nm (5-mer), 5.6 nm (14-mer) and 6.7 nm (17-mer) was measured by break junction method with a scanning tunneling microscope to clarify the charge transport mechanisms. The conductance of 17-mer molecule increased exponentially with temperature whereas the conductance of 5-mer and 14-mer molecules did not change. These results indicate that the dominant charge transport mechanism changed from tunneling to thermally activated hopping at molecular length around 6.7 nm (17-mer).

Reference

1) SK. Lee, R. Yamada, H. Kumazawa, H. Tada and S. Tanaka, *Funct. Mater. Lett.* **3**. 245–248 (2010).

Development of Novel Heterocyclic Compounds and Their Molecular Assemblies for Advanced Materials

Safety Office

TOMURA, Masaaki Assistant Professor

Heterocycles containing sulfur and/or nitrogen atoms are useful as components of functional organic materials since heteroatoms in their rings are helpful to stabilize ions or ion-radical species. In addition, intermolecular interactions caused by heteroatom contacts can be expected to form unique molecular assemblies. In this project, novel functional organic materials based on various heterocycles were synthesized and their physical and structural properties were investigated.

1. Synthesis and Properties of Terthiophene and Bithiophene Functionalized by BF_2 Chelation: A New Type of Electron Acceptor Based on Quadrupolar Structure[1)]

Terthiophene and bithiophene derivatives functionalized by BF_2 chelation were synthesized as a new type of electron acceptor, and their properties were compared to those of bifuran and biphenyl derivatives. These new compounds are characterized by quadrupolar structures due to resonance contributors generated by BF_2 chelation. The bithiophene derivative has a strong quadrupolar character compared with the bifuran and biphenyl derivatives because their hydrolytic analyses indicated that the bithiophene moiety has a larger on-site Coulomb repulsion than the others. The terthiophene derivative has a smaller on-site Coulomb repulsion than the bithiophene derivative due to the addition of a thiophene spacer. These BF_2 complexes exhibit long-wavelength absorptions and according to measurements of ionization potentials and absorption edges they have energetically low-lying HOMOs and LUMOs. The crystal structure of the bithiophene derivative is of the herringbone type, with short F···S and F···C contacts affording dense crystal packing. n-Type semiconducting behavior was observed in organic field-effect transistors based on these BF_2 complexes.

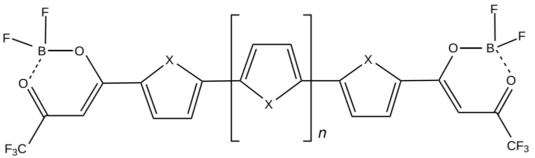

n = 0 or 1; X = S, O or -CH=CH-

2. Theoretical Study of Intermolecular S···N Interactions in a 1,2,5-Thiadiadole Dimer

Ab initio (HF, MP2) and DFT (B3LYP, PW91PW91) calculations with the 6-31++G(2d,2p) basis sets have been performed on a 1,2,5-thiadiazole dimer. The binding energy of the dimer by MP2 corrected BSSE and ZPE is 3.37 kcal/mol, which is comparable to those of noncovalent C–H···O and C–H···π interactions. The HF and DFT method extremely underestimated the binding energies as compared to MP2. This fact indicates that the dispersion interaction is significantly important for the intermolecular S···N interaction in the dimer. The optimized S···N distance (3.022 Å) by MP2 is in good agreement with crystallographic data.

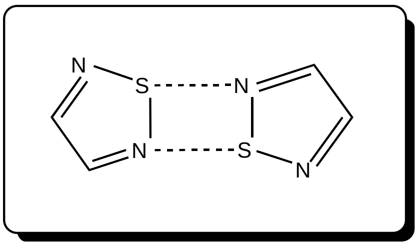

Reference

1) K. Ono, A. Nakashima, Y. Tsuji, T. Kinoshita, M. Tomura, J. Nishida and Y. Yamashita, *Chem. –Eur. J.* **16**, 13539–13546 (2010).

Visiting Professors

Visiting Professor
OHTA, Nobuhiro *(from Hokkaido University)*

Photoirradiation Effects on Structure, Dynamics and Material Properties

Photoinduced change in electrical conductivity as well as in structure and dynamics has been examined for various materials with the time-resolved measurements of resistance and/or luminescence following photoirradiation. In the photoirradiated organic crystals, conductivity switching and bistability of current over certain ranges of applied voltages have been observed. In organic superconductors, photoinduced change in the electrical conductivity has also been examined at temperatures in the vicinity of the metal–superconductor (M–S) phase transition temperature, and unconventional asymmetry of critical slowing down about the M–S transition temperature has been found. In ionic conductor such as silver iodide, photoirradiation effect on ionic conductivity has been observed, depending on the excitation wavelength. To understand the photoirradiation effect as well as the synergy effect of photoirradiatin and applied electric field on electrical conductivity, photoirradiation effects not only on the electrical conductivity but also on the magnetic property will be examined.

Visiting Professor
ABE, Manabu *(from Hiroshima University)*

Singlet Biradical Chemistry: π-Single Bonded Species

Localized singlet biradicals have been recognized as putative intermediates in processes involving homolytic bond-cleavages and formations. To understand the homolytic reactions, the singlet biradicals should be detected at least using conventional spectroscopic analyses. To this end, we needed to design and generate relatively long-lived singlet biradicals, in which the singlet state should be the ground state spin-multiplicity. In cyclopentane-1,3-diyl systems, we have found the notable substituent effect on lowering the singlet state energetically than the triplet state. Thus, the 2,2-dialkoxycyclopentane-1,3-diyls were calculated to be the singlet ground state molecules. The 1,3-diphenyl substitution of the 1,3-biracails allowed us to detect experimentally the singlet biradical at nano-second time scale. The species was found to be observed at λ_{max} 600 nm, which is persistent below the temperature of liquid nitrogen. The electronic transition was calculated to be corresponding to the $\pi \rightarrow \pi^*$ transition, which means that the singlet species possess a character of π-single bond.

Visiting Professor
KATO, Tatsuhisa *(from Kyoto University)*

Studies of Molecular Magnetization of Super-Molecules Relating Fullerenes

People distinguish electrons in terms of Cartesian coordinates in space as well as of spin ones. Although both coordinates are independent, some spin states are specified by the electron configuration on the levels of electronic wave function in space because of anti-symmetry with exchange of electrons. In this manner the electronic structure of molecules can be characterized through the measurement of spins. The high-spin states of metallo-fullerenes and molecular complexes were investigated by high-field and pulsed electron spin resonance (ESR) spectrometers. For example, the dimetallic endohedral heterofullerene, $Gd_2@C_{79}$ N, was characterized by a half-integer spin quantum number of $S = 15/2$ by ESR measurements. The result described an exceptionally stable paramagnetic molecule with low chemical reactivity, whose unpaired electron spins were localized on the internal diatomic gadolinium cluster.

RESEARCH ACTIVITIES

Life and Coordination-Complex Molecular Science

Department of Life and Coordination-Complex Molecular Science is composed of two divisions of biomolecular science, two divisions of coordination-complex molecular science, and one adjunct division. Biomolecular science divisions cover the studies on the elucidation of functions, dynamic structures, and mechanisms for various biomolecules such as sensor, membrane, and metal proteins, glycoconjugates, and molecular chaperone. Coordination complex divisions aim to develop molecular catalysts and functional metal complexes for transformation of organic molecules, reversible conversion between chemical and electrical energies, and artificial photosynthesis. Interdisciplinary alliances in this department aim to create new basic concepts for the molecular and energy conversion through the fundamental science conducted at each division.

Bioinorganic Chemistry of Metal-Containing Sensor Proteins

Department of Life and Coordination-Complex Molecular Science
Division of Biomolecular Functions

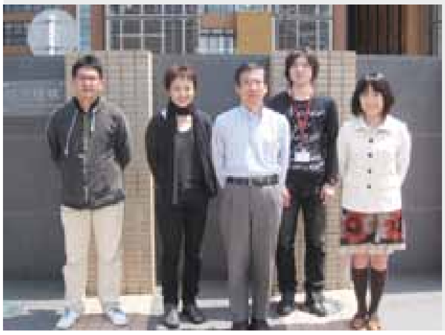

AONO, Shigetoshi	Professor
YOSHIOKA, Shiro	Assistant Professor
SAWAI, Hitomi	IMS Research Assistant Professor
YAMANAKA, Masaru	Post-Doctral Fellow
TANIZAWA, Misako	Secretary

Heme shows many biological functions. The most popular function is to be used as a prosthetic group in heme proteins. Heme proteins show a variety of functions including oxygen transport/storage, electron transfer, oxidase, peroxidase, oxygenase, catalase, and dehydratase. In addition to these functions, a new function of hemeprotein has been found recently, which is a sensor of diatomic gas molecules or redox change.[1,2] In these heme-based sensor proteins, the heme acts as the active site for sensing the external signal such as gas molecules and redox change. Heme also shows a novel biological function as a signaling molecule for transcriptional and translational regulation. In these systems, heme-sensing proteins sense a heme molecule to regulate biological processes. Our research interests are focused on the elucidation of the structure-function relationships of these heme-based sensor proteins and heme-sensing proteins.

1. Bacterial Gas Sensor Proteins Using Transition Metal-Containing Prosthetic Groups as Active Sites[3]

Gas sensor proteins are involved in many biological regulatory systems, including transcription, chemotaxis, and other complex physiological processes. These regulatory systems consist of a sensor and regulatory protein, and, if any, signal transduction proteins that transmit the input signal sensed by the sensor protein to regulator proteins. Sensor proteins are the most upstream component in these regulatory systems, and the sensor and regulator proteins can be distinct molecules, or can sometimes exist in the same molecule as sensor and regulator domains. In both cases, the general scheme is as follows for biological regulatory systems by gas sensor proteins. Once a gas sensor protein/domain senses a gas molecule of its physiological effector, a conformational change of the sensor protein/domain is induced, and then intra- and/or inter-molecular signal transductions proceed to modulate the activity of the regulator protein/domain that is responsible for the regulation of the above biological functions.

Elucidating the mechanisms of gas sensing and signal transduction is required to understand the structure and function of gas sensor proteins. To do this, the following questions should be answered. How do gas sensor proteins discriminate a physiological gas molecule from other gas molecules? What conformational changes are induced upon gas sensing, and how? How are the conformational changes induced by gas sensing related to the subsequent signal transduction process? How do intra- and inter-molecular signal transduction take place between the sensor and regulator protein/domain?

Gas sensor proteins that contain metal centers are advantageous for answering these questions, because the metal centers can serve as excellent spectroscopic probes in various applications such as UV/Vis, electron paramagnetic resonance (EPR), resonance Raman, circular dichroism (CD), and X-ray absorption spectroscopy (XAS). These methods can provide detailed information on the reactivity of the metal center with a gas molecule, and structural information around the metal center. X-ray crystallography is also an important tool to study gas sensor proteins. We have elucidated the structure and function relationships of the heme-based sensor proteins by these techniques.

Aer2 is a new MCP responsible for aerotaxis of *Pseudomonas aeruginosa*, which consists of N-terminal three-unit poly-HAMP, PAS, di-HAMP, and MCP domains. The Aer2 PAS domain contains a heme that acts as the active site for sensing O_2. Once the PAS domain senses O_2, intramolecular signal transduction will proceed from the PAS domain to the MCP domain. Though the HAMP domains are assumed to be responsible for intramolecular signal transduction, detail mechanisms remain to be elucidated.

We have determined the X-ray crystal structures of Aer2-N384 (residues 1-384 that consists of three-HAMP, PAS, and di-HAMP) and Aer2-PH (residues 173-384 that consists of PAS and di-HAMP) to elucidate the mechanism by which intramolecular signal transduction proceeds between the HAMP and PAS domains in Aer2. Aer2-N384 is a homodimer having a non-crystallographic 2-fold symmetry as shown in Figure 1. The three-unit poly-HAMP, PAS, and di-HAMP domains are ordered in linear configuration. Most of the C-terminal di-HAMP domain is disordered.

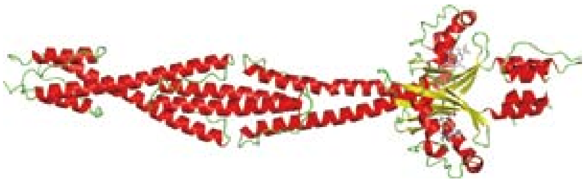

Figure 1. X-ray crystal structure of Aer2-N384 in cyano-met form.

Most of the di-HAMP domain is also disordered in the structure of Aer2-PH. A heme exists in a hydrophobic pocket in the PAS domain. His234 serves as the proximal ligand of the heme as shown in Figure 2. The 6-propionate forms a salt bridge with NE2 atom of His251, and the 7-propionate has hydrogen bonds with a water molecule, the main chain N atom of Lys235, and NE2 atom of Gln240. The heme-bound CN^- interacts with the side chain of Trp283. The distance is 2.9 Å between the N atom of CN^- and the NE2 atom of Trp283. CN-bound form of the heme can be thought to be a model of O_2-bound heme. The structure of Aer2-PH suggests that the heme-bound O_2 forms a hydrogen bond with Trp283. Trp283 is located on the C-terminal of the strand β5. This strand connects to the helix α5, which is the starting region of the C-terminal di-HAMP domain, suggesting that the hydrogen bond between Trp283 and O_2 are responsible for intramolecular signal transduction.

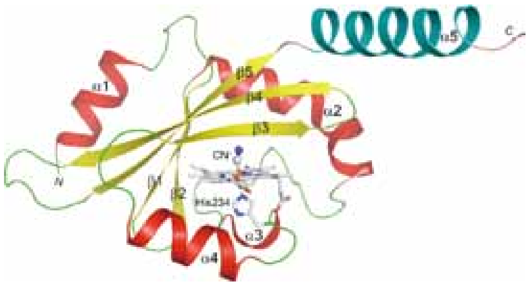

Figure 2. X-ray crystal structure of Aer2-PH in cyano-met form.

2. Structural Basis for the Transcriptional Regulation of Heme Homeostasis in *Lactococcus lactis*

Though a lactic acid bacterium *Lactococcus lactis* lacks heme biosynthesis genes, it can uptake and use heme molecules provided externally to grow by oxygen respiration. As free heme molecules are toxic for cells, cellular concentrations of heme should be controled strictly. *L. lactis* controls cellular heme concentrations by operating a heme efflux system. The expression of the heme efflux system is regulated by a heme-sensing transcriptional regulator HesR (heme efflux system regulator). In this work, we have determined X-ray crystal structures of HesR in heme-binding (holo-) and heme-free (apo-) forms to elucidate the structure and functions relationships of HesR.

HesR is a homo-dimer in the both of apo- and holo-forms as shown in Figure. HesR monomer consists of the N-terminal DNA-binding domain and the C-terminal heme binding domain that binds one heme molecule. Global fold of HesR is similar to that of TetR family transcriptional regulators. HesR is the first example of heme-sensing TetR family transcriptional regulator. A change in the relative orientation of the DNA-binding domain is induced upon heme-binding, which results in the regulation of DNA-binding activity of HesR.

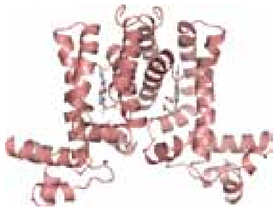

Figure 3. (Left) X-ray crystal structure of apo-HesR.

Figure 4. (Right) X-ray crystal structure of holo-HesR.

The HesR recognition sequence, ATGACACAGTGTCAT, is a perfect palindrome sequence as shown in the underlined sequence.We have found that apo-HesR can bind the target DNA, but holo-HesR can not. DNA-binding affinity of apo-HesR is determined to be Kd = 0.7 nM by fluorescence anisotropy measurements. These results indicate that heme molecule acts as a physiological effector of HesR to regulate its DNA-binding activity.

HesR shows a very high affinity for heme binding. When apo-HesR is mixed with holo-myoglobin, it can extract heme from myoglobin. The estimated heme binding affinity of HesR is comparable to that of myoglobin.

References

1) S. Aono, *Dalton Trans.* 3125–3248 (2008).
2) S. Aono, *Acc. Chem. Res.* **36**, 825–831 (2003).
3) S. Aono, *Antioxid. Redox Signaling* in press (2011).

Elucidation of the Molecular Mechanisms of Protein Folding

Department of Life and Coordination-Complex Molecular Science
Division of Biomolecular Functions

KUWAJIMA, Kunihiro	Professor
MAKABE, Koki	Assistant Professor
NAKAMURA, Takashi	IMS Research Assistant Professor
CHEN, Jin	OIIB Research Assistant Professor
TAKENAKA, Toshio	Post-Doctoral Fellow
MIZUKI, Hiroko	Technical Fellow
IKEDA, Yukako	Technical Fellow
TANAKA, Kei	Secretary

Kuwajima group is studying mechanisms of *in vitro* protein folding and mechanisms of molecular chaperone function. Our goals are to elucidate the physical principles by which a protein organizes its specific native structure from the amino acid sequence. In this year, we studied the equilibrium and kinetics of bimolecular MgATP^{2-} binding to GroEL.

1. Dissecting a Bimolecular Process of MgATP^{2-} Binding to the Chaperonin GroEL

The chaperonin GroEL from *Escherichia coli*, a tetradecameric protein complex consisting of two heptameric rings stacked back to back with a central cavity, is one of the best characterized molecular chaperones that facilitate protein folding *in vivo*. The ATP^{-} dependent control of the affinity for its target protein and the co-chaperonin GroES is essential for its molecular chaperone function, and this control occurs through a series of cooperative allosteric transitions of GroEL induced by MgATP^{2-}. The equilibria and kinetics of the allosteric transitions of GroEL have thus been studied for some time by a variety of techniques. However, the initial bimolecular step of MgATP^{2-} binding to GroEL, which must precede the allosteric transitions, remains to be clarified.

Here, we studied the equilibrium and kinetics of MgATP^{2-} binding to a variant of GroEL, in which Tyr485 was replaced by tryptophan, via isothermal titration calorimetry (ITC) and stopped-flow fluorescence spectroscopy (Figures 1 and 2). In the absence of K^{+} at 4 ~ 5 °C, the allosteric transitions and the subsequent ATP hydrolysis by GroEL are halted, and hence, the stopped–flow fluorescence kinetics induced by rapid mixing of MgATP^{2-} and the GroEL variant solely reflected MgATP^{2-} binding, which was well represented by bimolecular noncooperative binding with a binding rate constant, k_{on}, of 9.14×10^{4} M^{-1} s^{-1} and a dissociation rate constant, k_{off}, of 14.2 s^{-1}, yielding a binding constant, K_{b} (= $k_{\mathrm{on}}/k_{\mathrm{off}}$), of 6.4×10^{3} M^{-1}. We also successfully performed ITC to measure

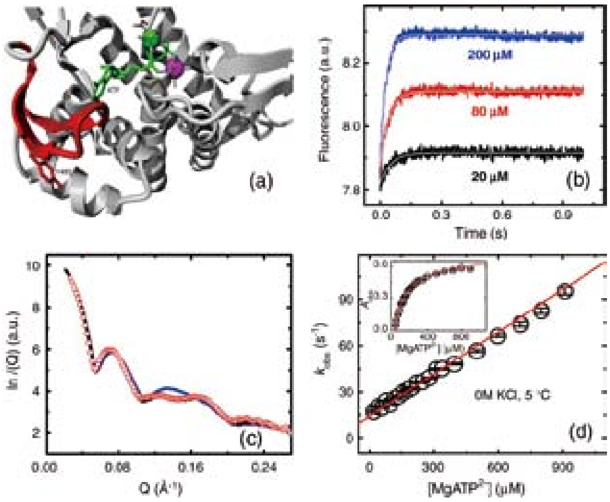

Figure 1. The structure around the MgATP^{2-}-binding site of GroEL (a), the SAXS patterns of wild-type GroEL in the different allosteric states (b), and the binding kinetics of MgATP^{2-} to GroEL(Y485W) (c and d).

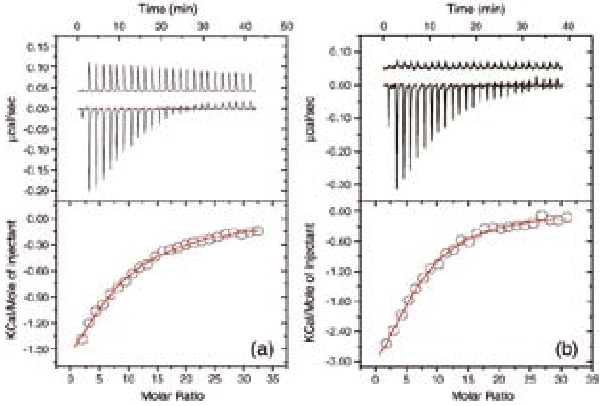

Figure 2. MgATP^{2-}-binding isotherms to GroEL(Y485W) (a) and GroEL(wild type) (b) measured by ITC in the absence of K^{+} at 5 °C.

binding isotherms of MgATP^{2-} to GroEL and obtained a K_b of 9.5×10^3 M^{-1} and a binding stoichiometric number of 6.6 (Figure 2). K_b was thus in good agreement with that obtained by stopped-flow fluorescence. In the presence of 10 ~ 50 mM KCl, the fluorescence kinetics consisted of three to four phases (the first fluorescence-increasing phase, followed by one or two exponential fluorescence-decreasing phases, and the final slow fluorescence-increasing phase), and comparison of the kinetics in the absence and presence of K$^+$ clearly demonstrated that the first fluorescence-increasing phase corresponds to bimolecular MgATP^{2-} binding to GroEL. The temperature dependence of the kinetics indicated that MgATP^{2-} binding to GroEL was activation-controlled with an activation enthalpy as large as 14 ~ 16 kcal mol^{-1}.

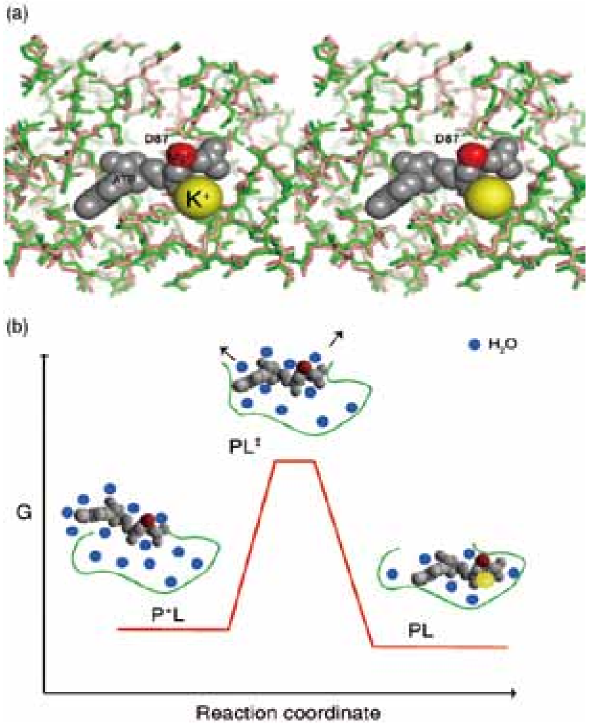

Figure 3. (a) A stereo view of superposition of X-ray structures of apo GroEL (green) (PDB code: 1OEL) and MgATP^{2-}-bound GroEL (pink) (PDB code: 1KP8) in a region around the binding site. (b) A reaction diagram of MgATP^{2-} binding to GroEL and schematic representations for the diffusional encounter complex (P*L), the transition–state complex (PL‡), and the final stable complex (PL).

To further elucidate what kind of activation (P*L $\rightarrow$ PL‡) takes place during MgATP^{2-} binding to apo GroEL, we investigated the X-ray crystallographic structures of the MgATP^{2-}-binding site of apo GroEL (PDB code: 1OEL) and MgATP^{2-}-bound GroEL (PDB code: 1KP8). The MgATP^{2-}-bound GroEL, originally complexed with ATPγS, assumed the T-state conformation, and hence provides an excellent model of the MgATP^{2-}-bound complex (PL) in the present study. As a result, the two structures were almost superimposable to each other. All atoms other than the O$^\gamma$ of Thr38 are not shifted more than 1.9 Å (Figure 3(a)).

If there is no essential difference in the binding-site structure between apo and MgATP^{2-}-bound GroEL, how can we explain the $\Delta H^‡$ of 14 ~ 16 kcal mol^{-1} that is involved in the activation step from P*L to PL (Figure 3(b))? A possible explanation is given by partial dehydration and conformational strain in the transition-state complex (PL‡) that exists between P*L and PL. Both MgATP^{2-} and the binding groove of GroEL are highly hydrated in P*L, but these hydrated water molecules must be completely removed from the binding surface between MgATP^{2-} and the binding groove in PL, except for the two caves underneath the groove. In PL‡, MgATP^{2-} and the binding groove are thus only partially dehydrated, and this partial dehydration increases the energy level of PL‡ as the final stabilization requires full dehydration. Furthermore, there may be conformational strain imposed on the binding groove in PL‡ when specific interactions steer the ligand into the binding groove, and probably some openings at the entrance of the groove are required for accommodating MgATP^{2-}. Such conformational strain also increases the energy level of PL‡. As a result, the activation from P*L to PL is accompanied by a $\Delta H^‡$ as large as 14 ~ 16 kcal mol^{-1}. Interestingly, a very similar $\Delta H^‡$ (16 kcal mol^{-1}) was observed in the reversed activation from P*L to PL. In the reversed process, the partial hydration and the conformational strain similarly occur in PL‡, leading to the similar $\Delta H^‡$ in the reversed activation process.

Reference

1) J. Chen, K. Makabe, T. Nakamura, T. Inobe and K. Kuwajima, *J. Mol. Biol.* **410**, 343–356 (2011).

Elucidation of Dynamical Structures of Biomolecules toward Understanding the Mechanisms Underlying Their Functions

Department of Life and Coordination-Complex Molecular Science
Division of Biomolecular Functions

KATO, Koichi	Professor
YAMAGUCHI, Takumi	Assistant Professor
KAMIYA, Yukiko	IMS Research Assistant Professor
UEKUSA, Yoshinori	Post-Doctoral Fellow
YAGI-UTSUMI, Maho	Post-Doctoral Fellow
NGUYEN, Le Anh	Visiting Scientist
TRINH XUAN, Anh	Visiting Scientist
BOONSRI, Pornthip	Visiting Scientist
BUI DINH, Long	Visiting Scientist
SUGIHARA, Takahiro	Research Fellow
CHANDAK, Mahesh	Graduate Student
ZHANG, Ying	Graduate Student
HIRANO, Takashi	Graduate Student*
UNO, Tsuyoshi	Graduate Student*
YAMAMOTO, Sayoko	Graduate Student*
SUZUKI, Mariko	Technical Fellow
ISONO, Yukiko	Technical Fellow
TANAKA, Kei	Secretary

Our biomolecular studies are based on detailed analyses of structures and dynamics of various biological macromolecules and their complexes at atomic level, primarily using NMR spectroscopy. Here we report NMR methods we recently developed for detailed conformational characterization of oligosaccharides and an NMR study of intermolecular interaction of amyloid β (Aβ) promoted on GM1 micelles.

1. Paramagnetic Lanthanide Tagging for NMR Conformational Analyses of *N*-Linked Oligosaccharides[1)]

Although NMR spectroscopy has great potential to provide information on structure and dynamics of oligosaccharides, the applicability of the NOE-based approach, widely used for protein-structure determination, is limited by the insufficiency of distance-restraint information as a consequence of the low proton density in oligosaccharides and the exceedingly low number of proton-proton NOEs. Hence, to develop NOE-independent approaches for determining the oligosaccharide conformations and dynamics, we employed paramagnetic effects using novel lanthanide tags attached to the reducing end of an *N*-linked oligosaccharide.

Paramagnetic effects, such as pseudocontact shifts (PCSs) induced by lanthanide ions with an anisotropic magnetic susceptibility tensor, offer long-distance information on conformations and dynamics of biological macromolecules. For the development of a general method, we focused on the common core structure shared among all *N*-linked oligosaccharides, *i.e. N,N'*-diacetylchitobiose. An EDTA derivative designed to serve as the paramagnetic tag by chelating a lanthanide ion was attached to *N,N'*-diacetylchitobiose through amide linkage mimicking the '*N*-linked' oligosaccharides.

By ^{1}H-^{13}C HSQC experiments using a series of paramagnetic lanthanide ions, the PCS values were measured as the differences of ^{1}H and ^{13}C chemical shifts from those of the complex with the diamagnetic La^{3+} ion as a reference. For quantitative validation of our approach, the experimentally obtained PCS values were compared with those calculated from the 3D model of the complex based on a reported conformation of *N,N'*-diacetylchitobiose. The back-calculated PCS values are in excellent agreement with the experimental data demonstrating the utility of our approach. These results indicate that the common innermost part of the *N*-linked oligosaccharides exhibits a rigid conformation, which is little affected by the attachment of the tag (Figure 1). The conformational rigidity of the glycosidic linkage of this disaccharide agrees with results from molecular dynamics simulation. This success opens the door to conformational studies of a variety of sugar chains of biological interest.

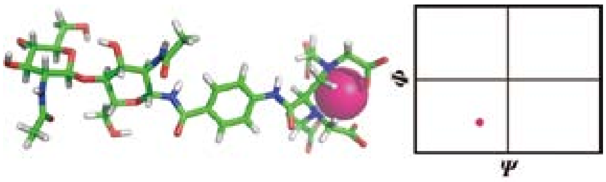

Figure 1. 3D structural model of the lanthanide-tagged *N,N'*-diacetylchitobiose and its glycosidic torsional angles.

2. Development of Metabolic ^{13}C-Labeling Techniques for Carbohydrate NMR Analyses Using Genetically Engineered Yeast Strain[2)]

Applicability of NMR approach to carbohydrate conformational analyses will be strengthened by combining it with stable isotope labeling of the oligosaccharides. However, methodology of stable isotope labeling of sugar chains has been largely unexplored, especially for larger, branched oligosaccharides. In view of the situation, we developed a novel method for overexpression of homogeneous oligosaccharides with ^{13}C labeling using genetically engineered yeast strain.

We employed engineered *Saccharomyces cerevisiae* cells, in which a homogeneous high-mannose-type oligosaccharide accumulates because of deletions of genes encoding three enzymes involved in the processing pathway of *N*-linked oligosaccharides in the Golgi complex. Using uniformly ^{13}C-labeled glucose as the sole carbon source in the culture medium of these engineered yeast cells, high yields of the isotopically labeled $Man_8GlcNAc_2$ (M8B) oligosaccharide could be successfully harvested from glycoprotein extracts of the cells. This enabled to observe ^{1}H-^{13}C HSQC spectrum at a proton observation frequency of 920.7 MHz. Furthermore, ^{13}C labeling at selected positions of the sugar residues in the oligosaccharide could be achieved using a site-specific ^{13}C- enriched glucose as the metabolic precursor, facilitating NMR spectral assignments (Figure 2). The ^{13}C-labeling method thus established provides the technical basis for NMR analyses of structures, dynamics, and interactions of larger, branched oligosaccharides.

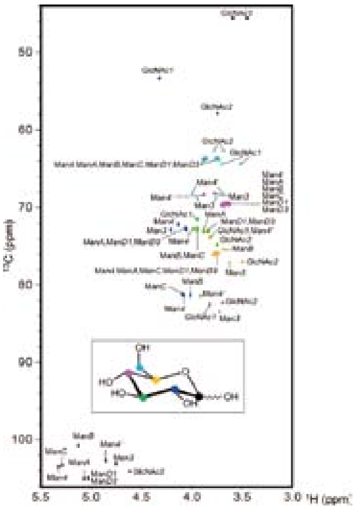

Figure 2. ^{1}H-^{13}C HSQC spectra of the pyridylamino derivative of M8B, metabolically ^{13}C-labeled using site-specific ^{13}C-enriched glucose isotopomers.

3. Spectroscopic Characterization of Intermolecular Interaction of Amyloid β Promoted on GM1 Micelles[3)]

Clusters of GM1 gangliosides act as platforms for conformational transition of monomeric, unstructured Aβ to its toxic β-structured aggregates. We previously reported that Aβ(1-40) is accommodated on the hydrophobic/hydrophilic interface of the ganglioside cluster exhibiting an α-helical conformation under ganglioside-excess conditions. To gain further insights into the underlying mechanisms of the amyloid formation of Aβ, it is necessary to characterize the conformational transition from α-helices to β-structures of Aβ on the ganglioside clusters.

We characterized conformational states of Aβ(1-40) in the presence of varying amounts of GM1 aqueous micelles using stable-isotope-assisted NMR spectroscopy in conjunction with synchrotron-radiation vacuum-ultraviolet CD spectroscopy. We found that GM1 micelles induce distinct secondary structures of Aβ(1-40) depending on the Aβ/GM1 ratios. Furthermore, it was revealed that the thioflavin T (ThT)-reactive β-structure is more populated in Aβ(1-40) under conditions where the Aβ(1-40) density on GM1 micelles is high. Under this circumstance, the C-terminal hydrophobic anchor Val39-Val40 shows two distinct conformational states that are reactive with ThT, while such Aβ species were not generated by smaller lyso-GM1 micelles (Figure 3). These findings suggest that GM1 clusters promote specific Aβ–Aβinteractions through their C-termini coupled with formation of the ThT-reactive β-structure depending on sizes and curvatures of the clusters.

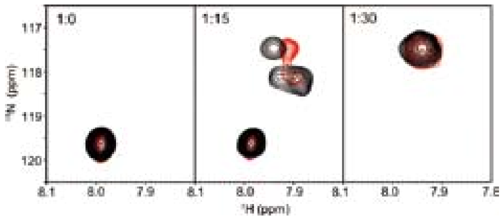

Figure 3. ^{1}H-^{15}N HSQC peak originating from Val39 of Aβ(1-40) titrated with GM1 micelles in the presence or absence of ThT. The spectra measured in the absence (black) and presence (red) of ThT are overlaid.

References

1) S. Yamamoto, T. Yamaguchi, M. Erdélyi, C. Griesinger and K. Kato, *Chem. –Eur. J.* **17**, 9280–9282 (2011).
2) Y. Kamiya, S. Yamamoto, Y. Chiba, Y. Jigami and K. Kato, *J. Biomol. NMR* **50**, 397–401 (2011).
3) M. Yagi-Utsumi, K. Matsuo, K. Yanagisawa, K. Gekko and K. Kato, *Int. J. Alzheimers. Dis.* **2011**, 925073 (8 pages) (2011).

Award

KATO, Koichi; The Pharmaceutical Society of Japan Award for Divisional Scientific Promotions.
YAGI-UTSUMI, Maho; The Protein Science Society of Japan Incentive Award for Young Investigators, The 11th Annual Meeting of the Protein Science Society of Japan (2011).

---

* carrying out graduate research on Cooperative Education Program of IMS with Nagoya City University

Structure-Function Relationship of Metalloproteins

Department of Life and Coordination-Complex Molecular Science
Division of Biomolecular Functions

FUJII, Hiroshi	Associate Professor
KURAHASHI, Takuya	Assistant Professor
CONG, Zhiqi	IMS Fellow
OHTSUKI, Akimichi	Post-Doctoral Fellow
WANG, Chunlan	Graduate Student
TANIZAWA, Misako	Secretary

Metalloproteins are a class of biologically important macromolecules, which have various functions such as oxygen transport, electron transfer, oxidation, and oxygenation. These diverse functions of metalloproteins have been thought to depend on the ligands from amino acid, coordination structures, and protein structures in immediate vicinity of metal ions. In this project, we are studying the relationship between the electronic structures of the metal active sites and reactivity of metalloproteins.

1. One-Electron Oxidation of Electronically-Diverse Manganese(III) and Nickel(II) Salen Complexes: Transition from Localized to Delocalized Mixed-Valence Ligand Radicals1)

Ligand radicals from salen complexes are unique mixed-valence compounds, in which a phenoxyl radical is electronically linked to a remote phenolate via a neighboring redox-active metal ion, providing an opportunity to study electron transfer from a phenolate to a phenoxyl radical mediated by a redox-active metal ion as a bridge. We herein synthesize one-electron oxidized products from electronically-diverse manganese(III) salen complexes, in which the locus of oxidation is shown to be ligand-centered, not metal-centered, affording manganese(III)–phenoxyl radical species. The key point in the present study is an unambiguous assignment of IVCT (intervalence charge transfer) bands by using non-symmetrical salen complexes, which enables us to obtain otherwise inaccessible insight into the mixed-valence property. A d^4 high-spin manganese(III) ion forms a Robin-Day Class II mixed-valence system, in which electron transfer is occurring between the *localized* phenoxyl radical and the phenolate. This is in clear contrast to a d^8 low-spin nickel(II) ion with the same salen ligand, which induces a *delocalized* radical (Robin-Day Class III) over the two phenolate rings, as previously reported by others. The present findings point to a fascinating possibility that electron transfer could be drastically modulated by exchanging the metal ion that bridges the two redox centers.

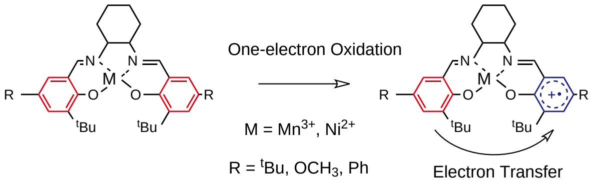

Figure 1. Mixed-Valence Ligand Radicals formed from manganese (III) and nickel(II) salen Complexes.

2. Redox Potentials of Oxoiron(IV) Porphyrin π-Cation Radical Complexes: Participation of Electron Transfer Process in Oxygenation Reactions2)

The oxoiron(IV) porphyrin π-cation radical complex (compound I) has been identified as the key reactive intermediate of several heme enzymes and synthetic heme complexes. The redox properties of this reactive species are not yet well understood. Here, we report the results of a systematic study of the electrochemistry of oxoiron(IV) porphyrin π-cation radical complexes with various porphyrin structures and axial ligands in organic solvents at low temperatures. The cyclic voltammogram of (TMP)Fe^{IV}O, (TMP = 5,10,15,20-tetramesitylporphyrinate), exhibits two quasi-reversible redox waves at $E_{1/2}$ = 0.88 and 1.18 V *vs.* SCE in dichloromethane at –60 °C (Figure 2). Absorption spectral measurements for electrochemical oxidation at controlled potential clearly indicated that the first redox wave results from the (TMP)Fe^{IV}O/[(TMP$^{+\bullet}$)Fe^{IV}O]$^{+}$ couple. The redox potential for the (TMP)Fe^{IV}O/[(TMP$^{+\bullet}$)Fe^{IV}O]$^{+}$ couple undergoes a positive shift upon coordination of an anionic axial ligand, but a negative shift upon coordination of a neutral axial ligand (imidazole). The negative shifts of the redox potential for the imidazole complexes are contrary to their high oxygenation activity. On the other hand, the electron-withdrawing effect of the meso-substituent shifts the redox potential in a positive direction. Comparison of the measured redox potentials and reaction rate constants for epoxidation of cyclooctene and demethylation of *N*,*N*-dimethylanilines enable us to discuss the details of the electron transfer process from substrates to the oxoiron(IV) porphyrin π-cation radical complex in the oxygenation mechanisms.

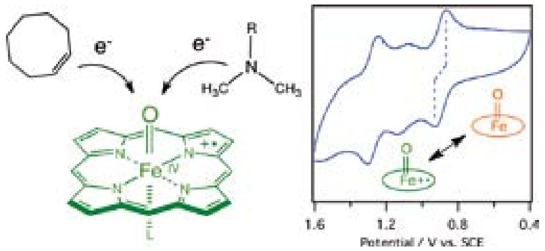

Figure 2. Cyclic Voltammogram of Oxoiron(IV) Porphyrin π-Cation Radical Complex.

3. Oxidation of Chloride Ion and Subsequent Chlorination of Organic Compounds by Oxoiron(IV) Porphyrin π-Cation Radical Complexes3)

Chloroperoxidase (CPO) and myeloperoxidase (MPO) are the only heme peroxidases that catalyze oxidation of chloride ion with hydrogen peroxide. CPO is an enzyme of *Caldariomyces fumago* and catalyzes chlorination reactions in the biosynthesis of chlorine-containing compounds. CPO is also known to exhibit peroxidase, catalase, and cytochrome P450-like activities. CPO has a thiolate heme axial ligand like cytochrome P450. This makes CPO distinct from other heme peroxidases which have a histidine imidazole as the heme axial ligand. On the other hand, MPO is found in the granules of myelocytes (precursors of neutrophils), and works as a major component of the antimicrobial system of neutrophils. MPO belongs to the animal peroxidase superfamily and has an imidazole heme axial ligand. Numerous biological studies have suggested that an oxoiron(IV) porphyrin π-cation radical species known as compound I, is responsible for oxidation of chloride ion and for addition of a chloride ion to the ferryl oxygen atom of compound I to produce a transient ferric hypochlorite complex, Fe(III)-OCl. The ferric hypochlorite complex is believed to act as a key compound in the reactions leading to chlorination of organic substrates by CPO and antimicrobial activity in MPO. Although the oxidation process has been studied by multi-mixing stopped-flow experiments in which transiently formed compound I were reacted with chloride ion, spectroscopic evidence for the formation of the ferric hypochlorite complex has not been obtained and it remains unclear how compound I oxidizes chloride ion. Furthermore, the identity of the true chlorinating agent in the subsequent chlorination of organic substrates is not known and more information is needed about the exact roles of the hypochlorite adduct, free hypochlorous acid, and Cl$_2$. Here, we report the direct observation of oxidation of chloride ion with synthetic compound I model complexes and subsequent reactions leading to chlorination of organic compounds (Figure 3).

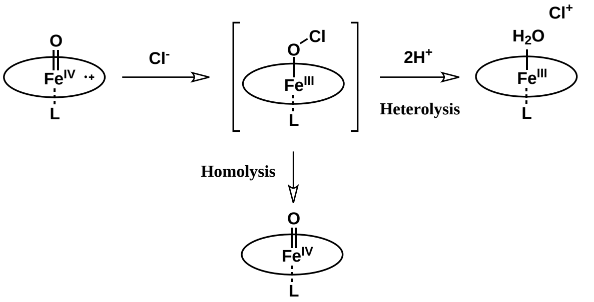

Figure 3. Cyclic Voltammogram of Oxoiron(IV) Porphyrin π-Cation Radical Complex.

References

1) T. Kurahashi and H, Fujii, *J. Am. Chem. Soc.* **133**, 8307–8316 (2011).
2) A. Takahashi, T. Kurahashi and H. Fujii, *Inorg. Chem.* **49**, 6922–6928 (2011).
3) Z. Cong, T. Kurahashi and H. Fujii, *Angew. Chem., Int. Ed.* **50**, 9935–9939 (2011).

Fabrication of Silicon-Based Planar Ion-Channel Biosensors and Integration of Functional Cell Membrane Model Systems on Solid Substrates

Department of Life and Coordination-Complex Molecular Science
Division of Biomolecular Sensing

URISU, Tsuneo	Professor*
TERO, Ryugo	Assistant Professor[†]
WANG, Zhihong	Post-Doctoral Fellow
RAHMAN, Mashiur	Post-Doctoral Fellow
ASANO, Toshifumi	Post-Doctoral Fellow
NAGAHIRO, Takeshi	Post-Doctoral Fellow
NAGAOKA, Yasutaka	Research Fellow
UNO, Hidetaka	Graduate Student
NAKAI, Naohito	Graduate Student
SHANG, Zhi-Guo	Graduate Student
FUJIWARA, Kuniyo	Graduate Student
SHIMIZU, Atsuko	Secretary

We are interested in the investigation of cell membrane surface reactions and the pathogen mechanism of the neuro-degenerative diseases, based on the molecular science. We are advancing two subjects, aiming the creation and development of new molecular science field, “medical molecular science.” One is the development of ion channel biosensor and its application to the neural network analyzer device. The other is the fundamental understanding of bilayer membrane properties using the artificial lipid bilayers on solid substrates, which is called supported bilayers, by means of atomic force microscope and fluorescence microscope-based techniques.

1. Development of Neural Network Device and Precise Microfabrications

Although the patch-clamp method using the pipette is now in practical use, it is not suitable for miniaturization and high throughput screening applications, since the measurement system is large and requires high level of skills for operations. It is expected that the breakthrough for these technical problems can be realized by the planarization of the device. For the planar typed ion channel biosensor, glass (Fertig, 2002), Si (Sordel, 2006, Matthews, 2006, Pantoja, 2004), quartz (Sett, 2003) and a silicon elastomer PDMS (Li, 2006), *etc.* have been reported as the substrate materials. And for Si, it has been considered that the background noise current is large due to the free charge carrier density in the substrate. However, we have recently demonstrated that the noise current can be significantly reduced by using silicon-on-insulator (SOI) or polymethyl methacrylate (PMMA) substrate.

Commercialized planer patch clamp devices, however, can not be used in a system that requires long incubation periods. New functional analysis and/or screening devices could be realized by adding an incubation function to the planar patch clamp method, and these would be especially useful in applications such as *in vitro* systems of neurons and neural networks using dissociated cultured neurons (Tao, 2000, Taylor, 2010, Reska, 2008, Erickson, 2008). Moreover, the planar patch clamp method enables simultaneous measurement of multi-point ion channel currents and advanced 2-D bio-imaging. We have developed an incubation type of planar patch clamp device and demonstrated its operation using TRPV1-expressing HEK293 cells and capsaicin as a ligand molecule. Detailed investigation about the basic properties have not yet been done.

The recently developed light-gated ion-channel method is extremely suitable for the investigation of neural cell and/or neural network functional analysis due to its excellent time and space resolutions (Petreanu, 2007). Concerning the application of light-gated ion-channel in the planar patch clamp method, however, no investigation has been done, in spite of its extreme importance.

In this work, ion channel biosensor based on the incubation type planar patch clamp method was developed and the basic properties were investigated. Due to the existence of ECM protein at the cleft between the cell membrane and the substrate surface near the miropore, it is not easy to realize the high seal resistance (giga-ohm seal). In the present case using collagen 4 as ECM, the seal resistance was usually about 10 MΩ, and the noise level was 7 pA with the 1 kHz low pass filter (Figure 1). The main noise sources were excess current noise and the thermal noise generated at micro pore resistance (R_a) and the seal resistance (R_j). All these noises can be reduced by increasing the seal resistance. Operation of the light-gated ion channel, ChRWR, was investigated by the incubation type planar patch clamp method using laser (λ = 473 nm) stimulations (Figure 2). The channel current profile and its membrane potential dependence well agreed to the reported data measured by pipette patch clamp method. So we think that light-gated method is also useful in the neural network function analysis and high throughput screening application based on the incubation type planar patch clamp method, and also useful in the simple performance check of these devices. The biosensor operation was examined, using TRPV1-expressing HEK293 cells. Quite high sensitivity was confirmed. But for the single channel recordings, several times improvement of the seal resistance is required.

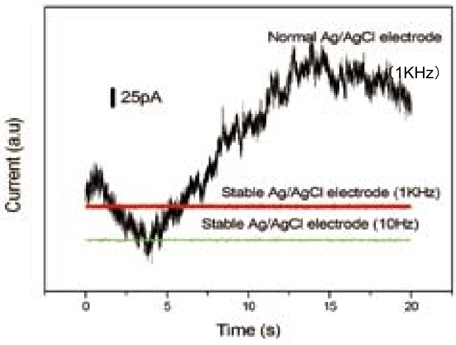

Figure 1. Observed current noise in the biosensor system.

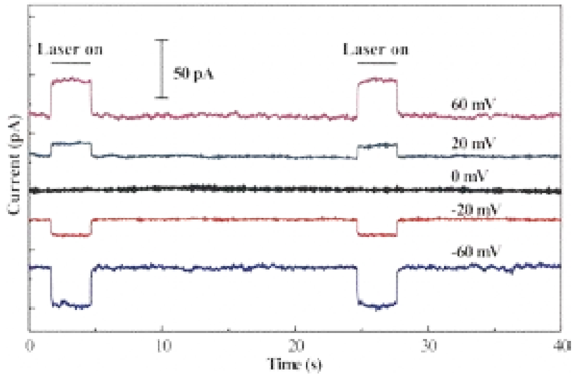

Figure 2. Observed ion channel current under voltage clamp of 473-nm laser irradiation with ChRWR-expressing HEK293. Ion channel current wave forms depend on the applied membrane potentials.

2. Extracellular Matrix Patterning for Cell Alignment by Atmospheric Pressure Plasma

Low-temperature atmospheric-pressure plasma (APP) jets and a metal stencil mask have been used for the patterning of fibronectins deposited on a silicon (Si) wafer. Fibronectins typically constitute the extracellular matrix (ECM) and a micro-patterned ECM may be used for arranging living cells in a desired pattern on the substrate surface. Such a technique can be used for the fabrication of cell chips. In this study, patterning of 100 mm wide lines of fibronectin layers has been demonstrated. Desorption of fibronectins from the surface by plasma application has been confirmed by atomic force microscopy (AFM) (Figure 3), and Fourier transform infrared spectroscopy (FT-IR).

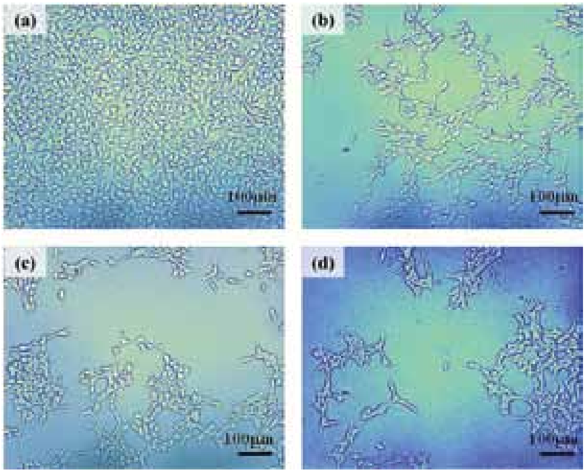

Figure 3. Photomicrographs of the sample substrate surface after plasma application of (a) 0 s (b) 10 s, (c) 20 s and (d) is 30 s. The photographs were taken after 72 hours cell cultivation.

---

* Present Address: Nagoya University

† Present Address: Electronics-Inspired Interdisciplinary Research Institute, Toyohashi University of Technology

Investigation of Molecular Mechanisms of Transporters and Receptors in Membrane

Department of Life and Coordination-Complex Molecular Science
Division of Biomolecular Sensing

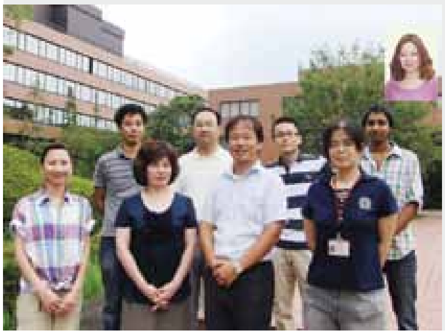

FURUTANI, Yuji	Associate Professor
KIMURA,Tetsunari	Assistant Professor
TSUKAMOTO, Hisao	IMS Research Assistant Professor
MEENA, Yatindra Shingh	Visiting Scientist
GUO, Hao	Graduate Student
FUJIWARA, Kuniyo	Graduate Student
INAGUMA, Asumi	Graduate Student
MURAMATSU, Chikako	Graduate Student*
SHIMIZU, Atsuko	Secretary

Membrane proteins are important for homeostasis of living cells, which work as ion channel, ion pump, various types of chemical and biophysical sensors, and so on. These proteins are considered as important targets for biophysical studies. However, their molecular mechanisms have not been studied well, because X-ray crystallography and NMR spectroscopy are hard to access them in general.

Our main goal is to clarify molecular mechanisms of transporters and receptors in cell membrane mainly by using stimulus-induced difference infrared (IR) spectroscopy, which is sensitive to the structural and environmental changes of organic and bio- molecules. In this year, Dr. Kimura has started to construct a microfluidic device to monitor biological and chemical reactions by infrared and fluorescent microscopic techniques.

1. Perfusion-Induced Difference FT-IR Spectroscopy for Na^+-Pump V-ATPase

Attenuated total reflection (ATR) FT-IR spectroscopy is a powerful technique to obtain infrared spectra of membrane proteins immersed in aqueous solution.[1,2] By exchanging buffer with and without salts, the difference spectra between the two conditions provide the structural information relating to the interaction between protein and ions. In this year, application of this technique to a transporter protein (V-ATPase) has been published in JACS.

V-ATPase from *Enterococcus hirae*, which forms a large supramolecular protein complex (total molecular weight: ~700,000), physiologically transports Na^+ and Li^+ across a hydrophobic lipid bilayer. Stabilization of these cations in the binding site has been discussed based on the X-ray crystal structures of a membrane-embedded domain, named the K-ring (Na^+ and Li^+ bound forms). Here, we applied ATR-FTIR spectroscopy on this large protein complex for the first time, and we measured sodium or lithium ion binding-induced difference infrared spectra of the intact V-ATPase with sufficient amount of hydration at physiological temperature.[1] The results suggest that binding of sodium or lithium ion induces the deprotonation of Glu139, resulting in a hydrogen-bonding change around a tyrosine residue and a little conformational change in the K-ring. These structural changes, especially the deprotonation of Glu139, are considered to be important for reducing energetic barriers to the transport of the cations across membranes.

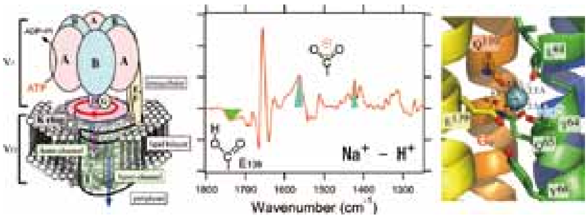

Figure 1. (left) Schematic structure of whole V-ATPase protein complex (center) Sodium ion binding induced difference infrared spectrum. The green and cyan colored bands are assigned to protonated and deprotonted carboxylic acid residues of Glu139 in K-ring, respectively. (right) Sodium ion binding site revealed by X-ray crystallography on K-ring.

2. Ion-Selective Mechanism of Mg^{2+} Transporter MgtE Studied by ATR FT-IR

Mg^{2+} is the most abundant divalent cation in living cells. MgtE is one of the Mg^{2+} transporters that function in the homeostasis of the intracellular Mg^{2+} concentration, in which the cytosolic domain acts as a 'Mg^{2+} sensor' and the transmembrane (TM) domain works as a 'pore.' Under high-intracellular Mg^{2+} conditions (> 10 mM), Mg^{2+} binding to the MgtE stabilizes a "closed" state and shuts down the Mg^{2+} transport from the extracellular part. In contrast, under low-intracellular Mg^{2+} conditions (< 1 mM), the MgtE is in equilibrium between the "closed" and "open" states, which can transport Mg^{2+}. In addition, MgtE is a highly Mg^{2+}-selective channel and unable to transport other divalent-cations including near-cognate Ca^{2+}. We performed the perfusion-induced difference ATR-FTIR measurements to understand the molecular mechanism underlying the Mg^{2+}-selectivity of MgtE.

The difference FTIR spectrum between the magnesium- and calcium-binding forms showed the bands between 1430 and 1380 cm^{-1} which are assigned to carboxylate groups. The COO$^-$ bands in the presence of Mg^{2+} were observed in the higher wavenumber than in the presence of Ca^{2+}, indicating weaker interaction of the carboxylate groups with Mg^{2+} than with Ca^{2+}. This result contradicts the stronger electrostatic interaction of fully dehydrated Mg^{2+} with COO$^-$ group compared with Ca^{2+}. On the other hand, the titration experiment for the closed states revealed that there are some binding sites to which Mg^{2+} binds ~40 times higher affinity than Ca^{2+} binds. The Mg^{2+}-binding site composed of the Asp432 in the TM domain (Mg1 site) is a plausible candidate based on our mutagenesis and protease protection experiments. These results suggest that the higher affinity for Mg^{2+} is due to the size of the cavity that can accommodate the hydrated Mg^{2+} rather than its charge intensity.

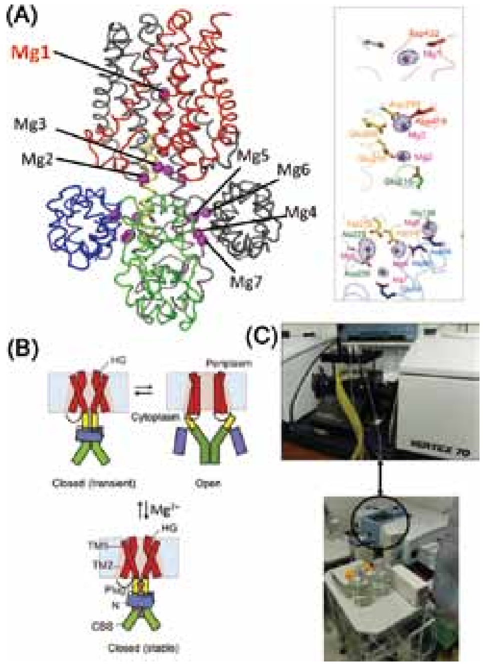

Figure 2. (A) X-ray crystal structure of MgtE in the closed state. *Inset*: Divalent cation binding sites. (B) Proposed gating mechanism of MgtE. (C) Pictures of the perfusion-induced difference ATR-FTIR measurements system.

3. Surface Enhanced Infrared Spectroscopy for Membrane Proteins in a Single Sheet of Lipid Bilayers

Monitoring structural changes of membrane proteins in a single sheet of lipid bilayer has been considered to be an ideal measurement method, while it is probably hard to detect tiny spectral change of the single-layered proteins. A graduate student, Mr. Hao Guo, has been struggling to establish the method. He got an award from SOKENDAI in advance of publication. In the near future, we will accomplish this challenging subject.

4. Development of a Microfluidic Device to Monitor Biological and Chemical Reactions

Real-time observation is one of the powerful techniques to understand the molecular mechanisms of the self-organization and molecular association. The solution mixing technique realizes many reaction fields for biological and chemical reactions by changing the buffer condition and can be combined with spectroscopic equipment easily. However, conventional mixing techniques limit their targets because of the large consumption of the sample. We are developing a novel microfluidic device and trying to reduce the sample consumption to ~1/1000. In addition, we aim to achieve the time-resolution of several microseconds by combining with microscopic techniques.

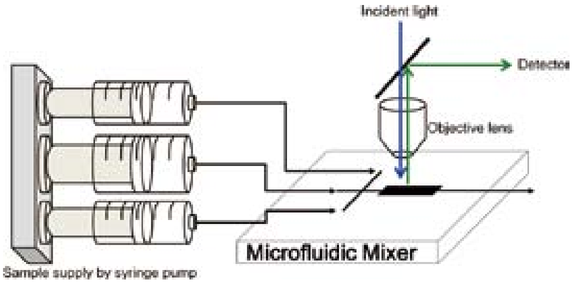

Figure 3. Schematic drawing of the microfluidic mixer.

Acknowledgements

We thank many collaborators, especially Prof. Hideki Kandori (Nagoya Institute of Technology) and Assoc. Prof. Takeshi Murata (Chiba University) for V-ATPase project, Prof. Osamu Nureki and Assoc. Prof. Ryuichiro Ishitani (University of Tokyo) for MgtE project.

References

1) Y. Furutani, T. Murata and H. Kandori, *J. Am. Chem. Soc.* **133**, 2860–2863 (2011).
2) J. Sasaki, H. Takahashi, Y. Furutani, H. Kandori and J. L. Spudich, *Biophys. J.* **100**, 2178–2183 (2011).

Award

GUO, Hao; FY2011 (the 2nd) Sokendai President’s Award.

* carrying out graduate research on Cooperative Education Program of IMS with Nagoya Institute of Technology

Heterogeneous Catalytic Systems for Organic Chemical Transformations in Water

Department of Life and Coordination-Complex Molecular Science
Division of Complex Catalysis

UOZUMI, Yasuhiro	Professor
OSAKO, Takao	Assistant Professor
HAMASAKA, Go	Post-Doctoral Fellow
ZHOU, Haifeng	Post-Doctoral Fellow
KOBAYASHI, Noboru	Graduate Student
MUTO, Tsubasa	Graduate Student
SAKURAI, Fumie	Graduate Student
TORII, Kaoru	Technical Fellow
TAZAWA, Aya	Technical Fellow
SASAKI, Tokiyo	Secretary
FUKUSHIMA, Tomoko	Secretary

Various transition metal-catalyzed organic molecular transformations in water were achieved under heterogeneous conditions by use of an amphiphilic resin-supported ruthenium complexes, a boron-iridium heterobimetallic polymeric catalyst, or an architecture-based system of transition metal catalysis using an amphiphilic pincer palladium complex bearing hydrophilic and hydrophobic chains which were designed and prepared by this research group. In particular, tandem olefin migration-aldol condensation and dehydrative alkylation, which were performed in water under heterogeneous conditions, and development of an amphiphilic pincer palladium complex bearing hydrophilic and hydrophobic chains for an architecture-based system of transition metal catalysis are highlights among the achievements of the 2010–2011 period to approach what may be considered ideal chemical processes of next generation. Representative results are summarized hereunder.

1. Tandem Olefin Migration-Aldol Condensation in Water with an Amphiphilic Resin-Supported Ruthenium Complex[1,2)]

A catalytic tandem olefin migration/aldol condensation process with allylic carbinols and aryl aldehydes was performed with an amphiphilic polystyrene-poly(ethylene glycol) (PS-PEG) resin-supported phosphine-ruthenium complex in water as a single reaction medium under heterogeneous conditions. It is noteworthy that the catalytic performance of the polymeric complex PS-PEG-phosphine-$RuCl_2Cp^*$ in water was much higher than that reported for ruthenium-phosphine complexes (*e.g.* $RuCl_2(PPh_3)_3$) under homogeneous conditions. Thus, 0.5 mol% Ru of the polymeric catalyst promoted the tandem olefin migration/aldol condensation in water at 45 °C within 2 h to give quantitative yields of the corresponding aldols with *syn*-selectivity. Inverse stereoselectivity (*anti*-selectivity) was observed when the reaction was carried out in the presence of K_2CO_3.

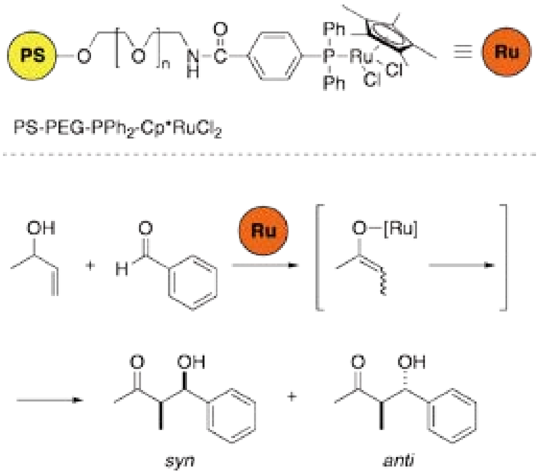

Scheme 1. Tandem Olefin Migration-Aldol Condensation in Water with Amphiphilic Resin-Supported Ruthenium Complex.

2. Molecular Architecture-Based Administration of Catalysis in Water via Self-Assembly of an Amphiphilic Palladium Pincer Complex[3)]

An architecture-based system of transition metal catalysis using an amphiphilic pincer palladium complex bearing hydrophilic and hydrophobic chains was developed, where (i) the self-assembling formation of bilayer vesicles of a palladium complex, (ii) the concentration of organic substrates at the hydrophobic region of the bilayer membrane, (iii) and the catalytic transformation of the substrate with the palladium species, all located in a close diffusion distance, automatically occurred in water. The oxirane ring opening reaction and the Michael reaction, both with arylboron reagents, were found to proceed in water where the vesicle structure of the palladium complex was essential to promote catalysis.

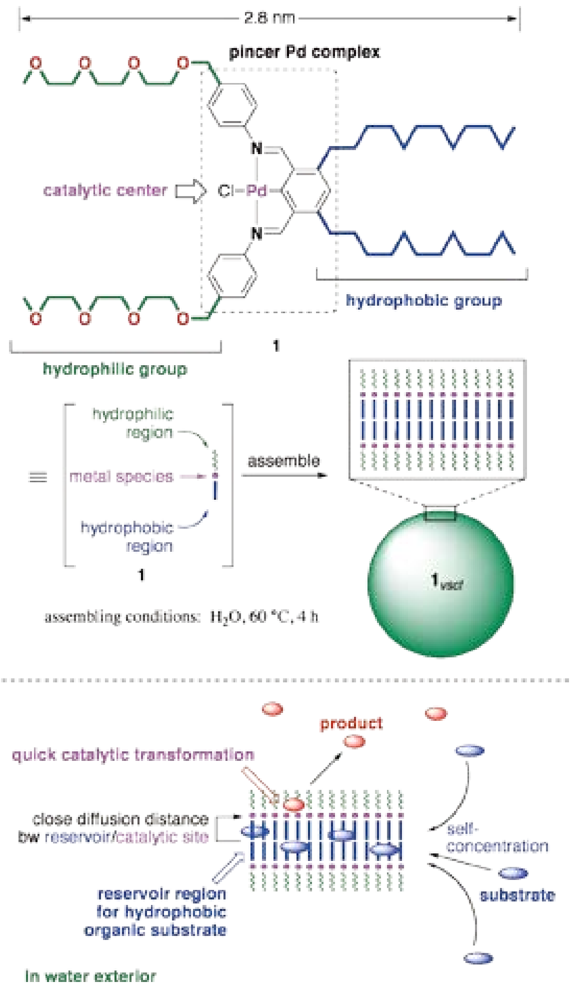

Scheme 2. Formation of Vesicle $\mathbf{1}_{vscl}$ by Self-Assembly of the Pincer Palladium Complex **1** (top) and Schematic Image of the Concept of Catalysis within the Bilayer membrane of the $\mathbf{1}_{vscl}$ (bottom).

3. In-Water Dehydrative Alkylation of Ammonia and Amines with Alcohols by a Polymeric Bimetallic Catalyst$^{4)}$

We have previously developed new methodology for the preparation of highly active and reusable polymer-supported catalysts, also known as "molecular convolution," where a soluble linear polymer having multiple ligand groups was convoluted with neutral metals or anionic metal salts via coordinative or ionic complexation to achieve the one-step preparation of the insoluble polymeric metal composite, combining heterogeneity and catalytic activity in one system. A novel convoluted polymeric metal catalyst was designed and prepared for the first time to realize "in-water dehydrative *N*-alkylation." Thus, a boron-iridium heterobimetallic polymeric catalyst was prepared by ionic convolution of a poly (catechol borate) and an iridium complex. The alkylation of ammonia and amines with alcohols, alkylating agents, was performed with 1 mol% Ir of the heterogeneous catalyst in water without the use of organic solvents under aerobic conditions to give the corresponding alkylated amines in up to quantitative yield.

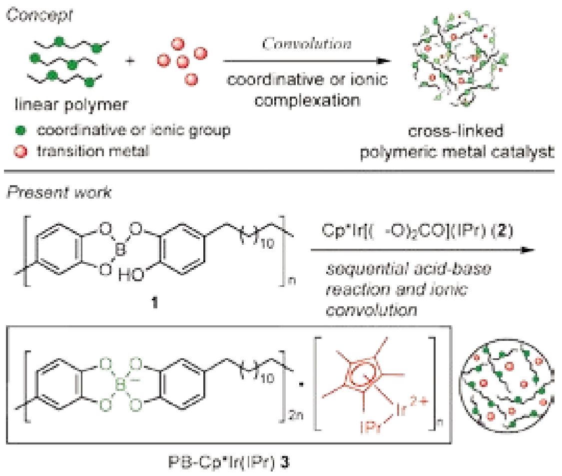

Scheme 3. Concept for the Molecular Convolution (top) and Preparation of PB-Cp*Ir(IPr) (bottom).

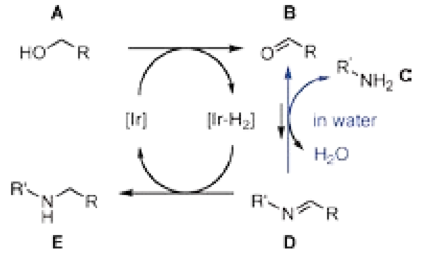

Scheme 4. Proposed Mechanism for In-Water Dehydrative *N*-Alkylation with PB-Cp*Ir(IPr).

References

1) Y. Oe and Y. Uozumi, *Adv. Synth. Catal.* **350**, 1771–1775 (2008).
2) Y. Oe and Y. Uozumi, *Synlett* 787–790 (2010).
3) G. Hamasaka, T. Muto and Y. Uozumi, *Angew. Chem., Int. Ed.* **50**, 4876–4878 (2011).
4) H. Ohta, Y. Yuyama, Y. Uozumi and Y. M. A. Yamada, *Org. Lett.* **13**, 3892–3895 (2011).

Synthesis of Metal Complexes Aiming at Storage and Release of Chemical Energy

Department of Life and Coordination-Complex Molecular Science
Division of Functional Coordination Chemistry

TANAKA, Koji	Professor
OHTSU, Hideki	Assistant Professor
KOBAYASHI, Katsuaki	IMS Research Assistant Professor
PADHI, Sumanta Kumar	Post-Doctoral Fellow
NAKANE, Daisuke	Post-Doctoral Fellow
YAMAGUCHI, Yumiko	Secretary
NOGAWA, Kyoko	Secretary

Artificial photosynthetic processes aimed at carbon dioxide reduction and water splitting are top research priorities for coping with the energy shortage that is anticipated in the near future to result from depletion of fossil fuels. Photoinduced one-electron transfer inevitably generates high-energy free radical intermediates that often trigger undesired side reactions, which is a serious issue that remains to be overcome. Proton coupled electron transfer is expected to substantially stabilize such radical intermediates, and could play a key role in multi-electron transfer to the relevant reaction sites involved in carbon dioxide reduction and water splitting.

Recently, we found that mono-nuclear [Ru(bpy)$_2$(pbn)](PF$_6$)$_2$ ([**1**]$^{2+}$; bpy = 2,2'-bipyridine, pbn = 2-(2-pyridyl)-benzo[*b*]-1,5-naphthyridine) is smoothly reduced to [Ru(bpy)$_2$(pbnH$_2$)](PF$_6$)$_2$ ([**1**•H$_2$]$^{2+}$; pbnH$_2$ = 5,10-dihydro-2-(2-pyridyl)benzo[*b*]-1,5-naphthyridine) by photoinduced two-electron reduction of pbn under irradiation with visible light in the presence of a sacrificial reagent. The reaction mechanism for the photoassisted two-electron reduction of [**1**]$^{2+}$ (Scheme 1) is explained as follows; i) photoexcitation of [**1**]$^{2+}$ and the subsequent reductive quenching of the photoexcited [**1**]$^{2+*}$ by a sacrificial donor produces [Ru(bpy)$_2$(pbn$^{\bullet-}$)]$^+$ ([**1**]$^+$), ii) protonation of the non-coordinating nitrogen of the pbn$^{\bullet-}$ of [**1**]$^+$ generates [Ru(bpy)$_2$(pbnH$^\bullet$)]$^{2+}$ ([**1**•H]$^{2+}$), iii) rapid dimerization of [**1**•H]$^{2+}$ through π–π interaction between two neutral pbnH$^\bullet$ of [**1**•H]$^{2+}$ affords [{**1**•H}$_2$]$^{4+}$, and iv) intramolecular electron and proton transfer from one pbnH$^\bullet$ to another one in [{**1**•H}$_2$]$^{4+}$ results in the disproportionation reaction to afford a 1:1 mixture of [**1**•H$_2$]$^{2+}$ (two-electron reduced form) and [**1**]$^{2+}$ (the starting complex).

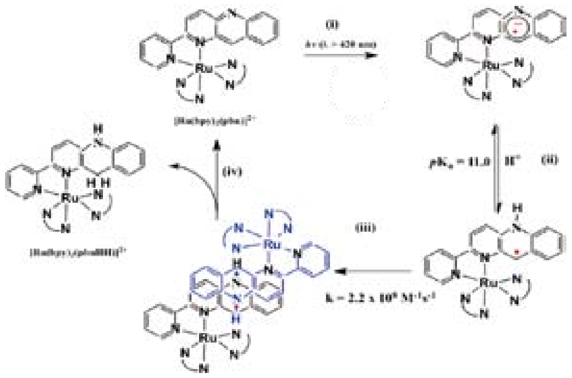

Scheme 1. Proposed mechanism for photochemical two-electron reduction of [**1**]$^{2+}$.

1. Photoinduced Four- and Six-Electron Reduction of Mononuclear Ruthenium Complexes Having NAD$^+$ Analogous Ligands

Mono-nuclear complexes are generally easier to synthesize and analyze their reaction mechanisms compared with multi-nuclear metal complexes. Photoinduced multi-electron redox reaction under visible light irradiation using mononuclear metal complexes is a fascinating approach to harvesting solar energy. Succesfull photochemical two electron reduction of [**1**]$^{2+}$ drove us to investigate the photoinduced four- and six-electron reduction of [Ru(bpy)(pbn)$_2$](PF$_6$)$_2$ ([**2**]$^{2+}$) and [Ru(pbn)$_3$](PF$_6$)$_2$ ([**3**]$^{2+}$), respectively, under irradiation with visible light. Photoirradiation (λ > 420 nm) of [**2**]$^{2+}$ and [**3**]$^{2+}$ in CH$_3$CN/triethanolamine (TEOA) brought about proton coupled four- and six-electron reduction of the complexes to produce [Ru(bpy)(pbnH$_2$)$_2$](PF$_6$)$_2$ ([**2**•H$_4$]$^{2+}$) and [Ru(pbnH$_2$)$_3$](PF$_6$)$_2$ ([**3**•H$_6$]$^{2+}$), respectively. To eluciadate the mechanism for the novel photoinduced multi-electron reduction, we examined redox and photophysical behavior of [**2**•H$_2$]$^{2+}$ having both pbn and pbnHH ligands. The complexes [**2**]$^{2+}$ and [**2**•H$_2$]$^{2+}$ exhibit two ($E_{1/2}$ = –0.69 and –0.82 V *vs.* SCE) and one ($E_{1/2}$ = –0.69 V) reversible (pbn$^{\bullet-}$/pbn) redox couples, respectively, and [**2**•H$_2$]$^{2+}$ and [**2**•H$_4$]$^{2+}$ displayed the pbnH$_2$

localized irreversible anodic peak at 1.15 V. The metal centered Ru^{II}/Ru^{III} redox potentials of [**2**]$^{2+}$, [**2**•H_2]$^{2+}$ and [**2**•H_4]$^{2+}$ are observed at $E_{1/2}$ = 1.44 V, 1.70 V and 1.70 V, respectively. The MLCT (d–π_{pbn}*) band of [**2**]$^{2+}$ and [**2**•H_2]$^{2+}$ is observed around 530 nm, and both complexes exhibit emissions from their lowest energy ^{3}MLCT (d–π_{pbn}*) excited states around 780 nm. The emission maximum of [**2**•H_2]$^{2+}$ (786 nm) in *n*-C_4H_9CN at 77 K, and the 0–0 transition energy of the complex is determined as 1.58 eV. The excited state redox potential for the (Ru^{II}*/Ru^{I}) couple calculated from the equation of $E(\mathrm{Ru^{II*}/Ru^{I}}) = E_{1/2}(\mathrm{pbn^{\bullet-}/pbn}) + E_{em}(0\text{–}0)$ is 0.89 V. Thus, the redox potential of the (Ru^{II}*/Ru^{I}) couple is located at a more negative potential than that of the oxidation of pbnH_2. Photoirradiation of the MLCT (d–π_{pbn}*) band of [**2**•H_2]$^{2+}$ bearing both pbn and pbnH_2 ligands, therefore, accepts one electron through intermolecular electron transfer from TEOA to the ruthenium center without accompanying intramolecular electron transfer from pbnH_2. Indeed, the electronic absorption spectrum of [**2**•H_2]$^{2+}$ in CH_3CN/TEOA (4:1, v/v) smoothly and completely changed to that of [**2**•H_4]$^{2+}$ at the expense of the MLCT (d–π_{pbn}*) absorption band at 530 nm of [**2**•H_2]$^{2+}$ under irradiation with visible light ($\lambda > 420$ nm). The photoinduced four- and six-electron reduction of [**2**]$^{2+}$ and [**3**]$^{2+}$ in CH_3CN/TEOA, therefore, is achieved by the repeated two-electron reduction of the Ru–pbn framework as described in Scheme 1.

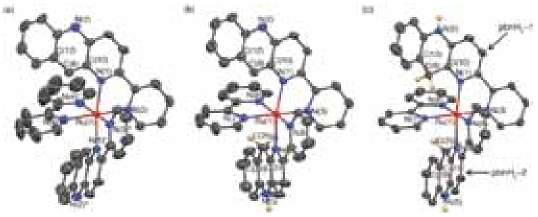

Figure 1. Crystal structures of [**2**]$^{2+}$, [**2**•H_2]$^{2+}$, and [**2**•H_4]$^{2+}$.

2. Photochemical and Electrochemical Redox Behavior of Cyclometallated Ru(II) Complexes with NAD$^+$/NADH Function

The world highly demands the renewable energy resources such as to capture and the storage of solar energy. One of the key issues for environmental science is to find out the alternative sources for the utilization of light driven energy in the form of chemical energy. In the realm of coordination chemistry ruthenium-poly-pyridyl complexes have been paid superior attention for molecular light-to-chemical energy conversion because of their unique photophysical properties and chemical stabilities. The photoinduced proton coupled “multielectronic reservoirs” of ruthenium complexes are far less common. A few research groups have reported the storage of more than one photo-excited electrons into the π* orbital of the poly-pyridyl ligands in the presence of sacrificial electron donors upon irradiation of visible light. Our group has developed two, four and six reversibly electron storing ability of [Ru(bpy)$_2$(**pbn**)](PF$_6$)$_2$, [Ru(bpy)(**pbn**)$_2$](PF$_6$)$_2$ and [Ru(**pbn**)$_3$](PF$_6$)$_2$ respectively, described above. We also found that [Ru(**phbn**)(bpy)$_2$]PF$_6$ ([**1**]PF$_6$; **phbn** = 3-phenylbenzo[*b*][1,6]naphthyridine) undergoes photochemical proton coupled two electron reduction.

Treatment of 3-phenylbenzo[*b*][1,6]naphthyridine (**phbn**) obtained by Scheme 2 with [(η^6-C_6H_6)RuCl_2]$_2$, NaPF$_6$ and NaOH in acetonitrile provides [Ru(**phbn**)(CH_3CN)$_4$]PF$_6$. Further addition of two equivalents of 2, 2’-bypiridyl with [Ru(**phbn**)(CH_3CN)$_4$]$^+$ in 2-methoxyethanol medium gives [Ru(**phbn**)(bpy)$_2$]$^+$ ([**4**]$^+$). The complex [**4**]PF$_6$ was reduced to [Ru(**phbnH$_2$**)(bpy)$_2$]PF$_6$ ([**4·HH**]PF$_6$) by chemical, electrochemical as well as photochemical methods (Scheme 3). The reaction of [**4**]PF$_6$ with NaBH_4 in methanol/H_2O mixture (9:1 v/v) gave [**4·HH**]PF$_6$ in a very good yield. Electrolysis of [**4**]PF$_6$ at –1.15 V (*vs*. SCE) in CH_3CN/H_2O (9:1 v/v) also produced [**4·HH**]PF$_6$ after two equivalent of electrons were consumed in the electrolysis. The continuous photolysis at ($\lambda \geq 420$ nm) of a 0.1 mM solution of [**4**]PF$_6$ in CH_3CN/Et_3N or CH_3CN/triethanolamine (CH_3CN/TEOA) (4:1, v/v) causes a decrease in the absorption band of [**4**]$^+$ (λ_{max} = 550 nm) and the appearance of a new species with band (λ_{max} = 425 nm) with a gradual change in color of [**4**]PF$_6$ purple to brownish red. The HR-ESI mass spectra, cyclic voltammogram as well as the UV-vis spectra of the resultant product are consistent with those of [**4·HH**]PF$_6$ obtained by the chemical reduction method. The ^{1}H NMR spectrum of [**4·HH**]PF$_6$ in CD_3CN displayed 17 different signals with a total intensity of 29 protons, out of which 27 are in the aromatic region generating from two bpy and **phbnH$_2$** ligand. An AB patterned doublet observed at 3.36 (^{1}H, d, *J* = 19.53), 3.52 (^{1}H, d, *J* = 18.93) ppm due to the germinal coupling of the methylene protons.

Scheme 2. Synthesis of phbn.

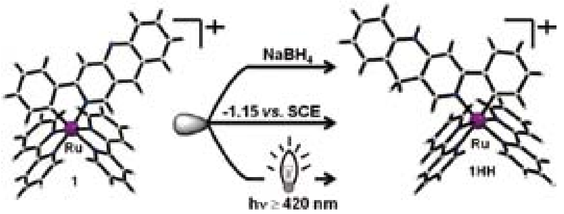

Scheme 3. Chemical, photo, and electrica reduction of [**4**]$^+$.

Development of Functional Metal Complexes for Artificial Photosynthesis

Department of Life and Coordination-Complex Molecular Science
Division of Functional Coordination Chemistry

MASAOKA, Shigeyuki	Associate Professor
KONDO, Mio	Assistant Professor
YOSHIDA, Masaki	Graduate Student*
KIMOTO, Ayano	Graduate Student*
OKAMURA, Masaya	Graduate Student
KUGA, Reiko	Technical Fellow
TORII, Sena	Technical Fellow
YAMAGUCHI, Yumiko	Secretary

Visible light-induced water splitting ($2H_2O + 4h\nu \rightarrow 2H_2 + O_2$) has attracted considerable attention in recent years due to its potential application in artificial solar energy conversion and storage. This water-to-fuels conversion consists of the two half-cell reactions; reduction of water to H_2 ($2H^+ + 2e^- \rightarrow H_2$) and oxidation of water to O_2 ($2H_2O \rightarrow O_2 + 4H^+ + 4e^-$). In this context, we have investigated oxygen evolution and photochemical hydrogen evolution from water catalyzed by metal complexes. In this report, we show (i) the mechanism of water oxidation catalyzed by mononuclear ruthenium complexes, (ii) electrocatalytic water oxidation at an ITO electrode modified with mononuclear ruthenium complexes, and (iii) photochemical hydrogen production from water catalyzed by carboxylate-bridged dirhodium(II) complexes.

1. Mechanism of Water Oxidation Catalyzed by Mononuclear Ruthenium Complexes[1)]

As mentioned above, the water splitting reaction can be divided into the two half-cell reactions; reduction of water to H_2 and oxidation of water to O_2. Particularly, development of molecular catalysts for O_2 evolution has been targeted by many researchers, since the O_2 evolution requires removal of four protons and four electrons, and is therefore considered more difficult process to accelerate. Recently, several different groups, including our group, discovered that mononuclear ruthenium complexes with an aqua ligand, such as $[Ru(terpy)(bpy)(OH_2)]^{2+}$ (terpy = 2,2':6',2"-terpyridine, bpy = 2,2'-bipyridine), exhibit surprisingly high catalytic activity towards O_2 evolution from water in the presence of Ce^{4+} as an oxidizing reagent in acidic aqueous media. These findings became a significant breakthrough in this field and various reaction mechanisms have been proposed to date.

We have investigated the mechanism of O_2 evolution from water catalyzed by a series of mononuclear aquaruthenium complexes, $[Ru(terpy)(bpy)(OH_2)]^{2+}$ (**1**), $[Ru(tmtacn)(R_2bpy)(OH_2)]^{2+}$ (**2** for R = H, **3** for R = Me, and **4** for R = OMe; R_2bpy = 4,4'-disubstituted-2,2'-bipyridines), and $[Ru(tpzm)(R_2bpy)(OH_2)]^{2+}$ (**5** for R = H, **6** for R = Me, and **7** for R = OMe), where tmtacn = 1,4,7-trimethyl-1,4,7-triazacyclononane, and tpzm = tris(1-pyrazolyl)methane. The kinetics of O_2 evolution is investigated as a function of either the catalyst concentration or the oxidant concentration by employing $Ce(NH_4)_2(NO_3)_6$ as an oxidant, revealing that these catalysts can be classified into two groups exhibiting different rate laws for O_2 evolution. In one class (**1**, and **5**–**7**), the rate of O_2 evolution is linear to both the catalyst and Ce^{4+} concentrations. For the other class (**2**–**4**), the rate of O_2 evolution is quadratic to the catalyst concentration and independent of the Ce^{4+} concentration. Moreover, the singlet biradical character of the hydroxocerium(IV) ion is realized by the experimental and DFT investigations. These results indicate that the radical coupling of the oxygen atoms of a $Ru^V{=}O$ species and a hydroxocerium(IV) ion is the key step for the catalysis of **1** and **5**–**7**, while the well-known oxo–oxo radical coupling among two $Ru^V{=}O$ species proceeds in the catalysis of **2**–**4**. This is the first report demonstrating that the radical character provided by the hydroxocerium(IV) ion plays a crucial role in the catalysis of such ruthenium complexes in O_2 evolution from water.

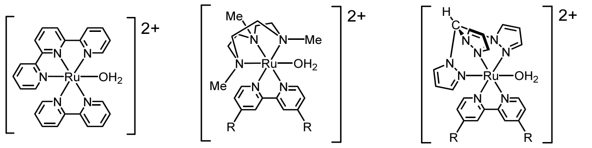

$[Ru(terpy)(bpy)(OH_2)]^{2+}$
1

$[Ru(tmtacn)(R_2bpy)(OH_2)]^{2+}$
2, R = H
3, R = Me
4, R = OMe

$[Ru(tpzm)(R_2bpy)(OH_2)]^{2+}$
5, R = H
6, R = Me
7, R = OMe

Figure 1. Structures of mononuclear aquaruthenium catalysts for water oxidation.

2. Electrocatalytic Water Oxidation at an ITO Electrode Modified with Mononuclear Ruthenium Complexes[2)]

An ITO (indium tin oxide) electrode modified with [Ru(terpy){4,4'-($CH_2PO_3H_2$)$_2$-2,2'-bpy}(OH_2)]$^{2+}$ (**8**) was prepared to gain insight into the mechanism of O_2 evolution from water catalyzed by a series of mononuclear aquaruthenium complexes. The average separation between two closest molecules can be estimated to be ca. 35 Å. This system does not allow two or more ruthenium centers to engage in the same O_2-evolving event, and hence the electrocatalytic O_2 evolution from water promoted with this system can be fully attributable to an O_2-evolving event at a single aquaruthenium site. Indeed, the modified ITO electrode showed a clear decrease in overpotential for O_2 evolution (1.35 V in an aqueous 0.1 M Na_2SO_4/H_2SO_4 solution, pH 4.0), indicating that the O_2 evolution proceeds in a unimolecular fashion without having any intermolecular associations.

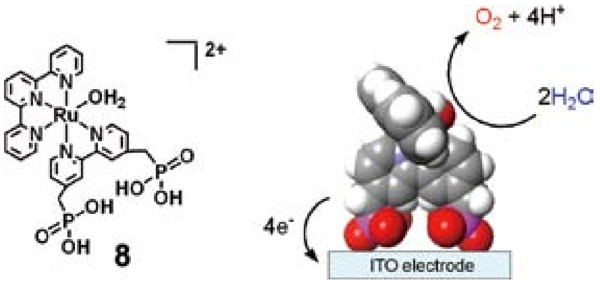

Figure 2. Schematic view of the electrochemical water oxidation catalyzed by a mononuculear ruthenium complex (**8**).

3. Photochemical Hydrogen Production from Water Catalyzed by Carboxylate-Bridged Dirhodium(II) Complexes[3)]

A series of dinuclear Rh(II) complexes, [Rh_2(μ-OAc)$_4$(H_2O)$_2$] (HOAc = acetic acid) (**9**), [Rh_2(μ-gly)$_4$(H_2O)$_2$] (Hgly = glycolic acid) (**10**), [Rh_2(μ-CF_3CO_2)$_4$(acetone)$_2$] (**11**), and [Rh_2(bpy)$_2$(μ-OAc)$_2$(OAc)$_2$] (**12**), were found to serve as H_2-evolving catalysts in a three-component system consisting of tris(2,2'-bipyridine)ruthenium(II) (Ru(bpy)$_3^{2+}$), methylviologen (MV^{2+}), and ethylenediaminetetraacetic acid disodium salt (EDTA). It was also confirmed that thermal reduction of water into H_2 by $MV^{+\bullet}$, in situ generated by the bulk electrolysis of MV^{2+}, is effectively promoted by **9** as a H_2-evolving catalyst. The absorption spectra of the photolysis solution during the photocatalysis were monitored up to 6 h to reveal that the formation of photochemical or thermal byproducts of $MV^{+\bullet}$ is dramatically retarded in the presence of the Rh(II)$_2$ catalysts, for the H_2 formation rather than the decomposition of $MV^{+\bullet}$ becomes predominant in the presence of the Rh(II)$_2$ catalysts. The stability of the Rh(II)$_2$ dimers was confirmed by absorption spectroscopy, ^{1}H NMR, and ESI-TOF mass spectroscopy. The results indicated that neither elimination nor replacement of the equatorial ligands take place during the photolysis, revealing that one of the axial sites of the Rh_2 core is responsible for the hydrogenic activation. The quenching of Ru*(bpy)$_3^{2+}$ by **9** was also investigated by luminescence spectroscopy. The rate of H_2 evolution was found to decrease upon increasing the concentration of **9**, indicating that the quenching of Ru*(bpy)$_3^{2+}$ by the Rh(II)$_2$ species rather than by MV^{2+} becomes predominant at the higher concentrations of **9**. The DFT calculations were carried out for several possible reaction paths proposed (*e.g.*, [Rh^{II}_2(μ-OAc)$_4$(H_2O)] + H^+ and [Rh^{II}_2(μ-OAc)$_4$(H_2O)] + H^+ + e^-). It is suggested that the initial step is a proton-coupled electron transfer (PCET) to the Rh(II)$_2$ dimer leading to the formation of a Rh(II)Rh(III)–H intermediate. The H_2 evolution step is suggested to proceed either *via* the transfer of another set of H^+ and e^- to the Rh(II)Rh(III)–H intermediate or *via* the homolytic radical coupling through the interaction of two Rh(II)Rh(III)–H intermediates.

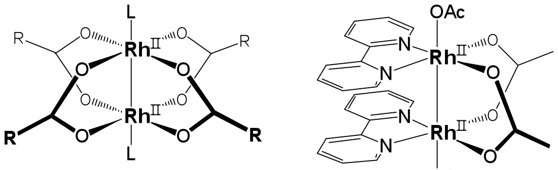

R = CH_3, L = H_2O (**9**)
R = CH_2OH, L = H_2O (**10**)
R = CF_3, L = acetone (**11**)

[$Rh^{II,II}_2$(bpy)$_2$(OAc)$_4$] (**12**)

Figure 3. Structures of carboxylate-bridged dirhodium(II) catalysts for photochemical water reduction.

References

1) M. Yoshida, S. Masaoka, J. Abe and K. Sakai, *Chem. –Asian J.* **5**, 2369–2378 (2010).
2) J. Kiyota, J. Yokoyama, M. Yoshida, S. Masaoka and K. Sakai, *Chem. Lett.* **39**, 1146–1148 (2010).
3) S. Tanaka, S. Masaoka, K. Yamauchi, M. Annaka and K. Sakai, *Dalton Trans.* **39**, 11218–11226 (2010).

Awards

MASAOKA, Shigeyuki; The 25th Young Scholar Lectures in the 91th Annual Meeting of CSJ (2011).
KONDO, Mio; Poster Award at 60th Anniversary Conference on Coordination Chemistry in OSAKA (2010).
KONDO, Mio; The 27th Inoue Research Award for Young Scientists (2010).

---

* carrying out graduate research on Cooperative Education Program of IMS with Kyushu University

Visiting Professors

Visiting Professor

NISHIHARA, Hiroshi *(from The University of Tokyo)*

Coordination Programming of Electro- and Photo-Functional Materials

One of the goals of molecular electronics is to control electron conduction in molecular wires and networks by combining appropriate molecular units. We are investigating the construction of hetero metal complex oligomer wires by an interfacial stepwise coordination method using various combinations of surface materials, ligands and metals in order to clarify all the factors to decide the electron conduction behaviors. The surface coordination programming is being applied for development of bio-photosensors and also new types of electro- and photo-functional molecular systems based on photochromism, strong donor–acceptor interaction, π-conjugation, and molecular rotation.

Visiting Associate Professor

UENO, Takafumi *(from Kyoto University)*

Novel Functional Nano Bio-Materials Based on Protein Assembly

Our research interests focus on the understanding, utilization, and design of protein assemblies that promote chemical reactions. We are developing strategies to functionalize natural protein assemblies as well as prepare artificial protein assemblies. This will expand the possibilities of our research into several emerging fields by bringing together the fields of organic chemistry, inorganic chemistry, biochemistry, molecular biology and structural biology.

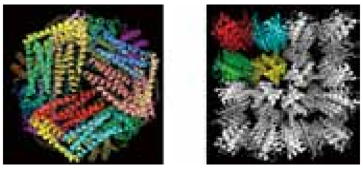

Visiting Associate Professor

OYAMA, Dai *(from Fukushima University)*

Development of Highly Functionalized Transition Metal Complexes Based on Non-Innocent Ligands

Redox reactions are one of the most fundamental chemical reactions. Nature often utilizes redox-active organics in chemical transformations. Therefore, significant attention is currently focused on ligand-centered redox reactions in transition metal complexes.

We have investigated the synthesis and properties of the ruthenium complexes containing both pyridyl binding sites and azo, naphthyridine or quinone moieties which are closely related to biologically important molecules. In particular, we have studied on some important reaction systems such as multi-electron CO_2 reductions and H_2 evolution, based on proton-coupled electron transfer (PCET).